Electronic Thesis and Dissertation Repository

8-30-2017 10:00 AM

Pressure Equalization of Wind-Induced Pressures on Residential Vinyl Siding Cladding in Full-Scale

Randy A. Van Straaten, *The University of Western Ontario*

Follow this and additional works at: https://ir.lib.uwo.ca/etd

Part of the Civil Engineering Commons

Abstract

Residential vinyl siding cladding system failures have been observed in high wind events. North American vinyl siding design standards allow a 64% pressure equalization factor, which yield relatively low wind load resistance for these products. The allowance is based on testing, which is questioned based on the literature review. The modified discharge equation analytical model, developed by others, accurately predict extent of pressure equalization found in scaled wind tunnel measurements. The model provides value in informing testing standards, product design and forensic investigations. However, it has only been validated based on scaled wind tunnel testing which may present scaling effect errors.

In this study, the analytical model is verified through testing of a full-scale simplified cladding system, a dataset collected from full-scale wind tunnel testing is analyzed, and the model is adapted to vinyl siding and compared to full-scale wind tunnel test measurements. Wall friction losses, discharge losses, and inertial effects are evaluated using the full-scale simplified cladding system. Wall friction losses were found to fall between those predicted for fully developed laminar and turbulent flow models for steady flows. Discharge losses for orifice flows into a deep (9.46mm) cavity best fit the sharp-edged orifice equation while application of entrance/exit, elbow, and tee loss coefficients best fit orifice flows into a shallow (2.58mm) cavity. Use of effective slug lengths are able to capture inertial effects found in unsteady measurements.

Analysis of a full-scale wind tunnel dataset for vinyl siding clad walls suggest negligible influence by sheathing air leakage and flexibility. The analytical model used in the first part of the study was found in this final part to accurately predict vinyl siding pressure equalization performance. The model is then used to show that a factor of 10 increase in open area and a reduction of cavity depth to 4mm was required for the 64% allowance in the code.

Keywords

Acknowledgments

Table of Contents

List of Tables

List of Figures

List of Appendices

Nomenclature

A	Area (m^2)
C	Coefficient (-)
D	Diameter (m)
f	Frequency (Hz)
f	Darcy friction factor (-)
G	Orifice width (m)
h	Eave height (m)
H	Cavity depth (m)
k	Discharge coefficient (-)
l	Panel thickness or orifice length (m)
L	Cavity or wall length (m)
n	Power law exponent (-)
N	Total number of openings (-)
O	Open area ratio (-)
p	Pressure (Pa)
P	Amplitude of applied pressure (Pa)
PEF	Pressure Equalization Factor (-)
Q	Volumetric flow rate (m^3/s)
Re	Reynolds number (-)
Ro	Roshko number (-)
St	Strouhal number (-)
t	Time (s)
T	Temperature (°C)
u	Cavity airflow velocity (m/s)
U	Horizontal wind velocity (m/s)
v	Orifice airflow velocity (m/s)
W	Height of a vertical slot (m)
ρ	Density (kg/m^3)
ɸ	Velocity phase shift (degrees)
τ	Shear stress (N/m^2 or kg m/s^2 /m^2)
μ	Dynamic viscosity (kg/(s·m))

Subscripts

b	Batt space
c	Cavity
d	Entrance and diverging tee
e	Exterior surface
eff	Effective
h	Hydraulic
i	Internal
l	Loss
m	Merging tee and exit
n	Entrance and elbow
x	Elbow and exit

Chapter 1

1 Introduction

Wall cladding systems must be designed to withstand design wind conditions. A field assessment of building damage from Hurricanes Rita and Katrina (NIST 2006) found cladding on residential buildings mostly undamaged by the storms except for aluminum and vinyl siding cladding. Hence, there appears to be an issue with the design of such systems.

Modern North American houses, such as those in the regions affected by Hurricanes Rita and Katrina, typically have multi-layer wall systems with an air cavity separating the cladding layer from the remaining inner layers, as shown in Figure 1. The main function of this air cavity is for rain water drainage and accommodation of construction tolerances (Garden 1963, Gerhardt and Janser 1994, Straube and Burnett 1999). The wind load on the cladding is the difference between the exterior surface pressure and interior cavity-side surface pressure.
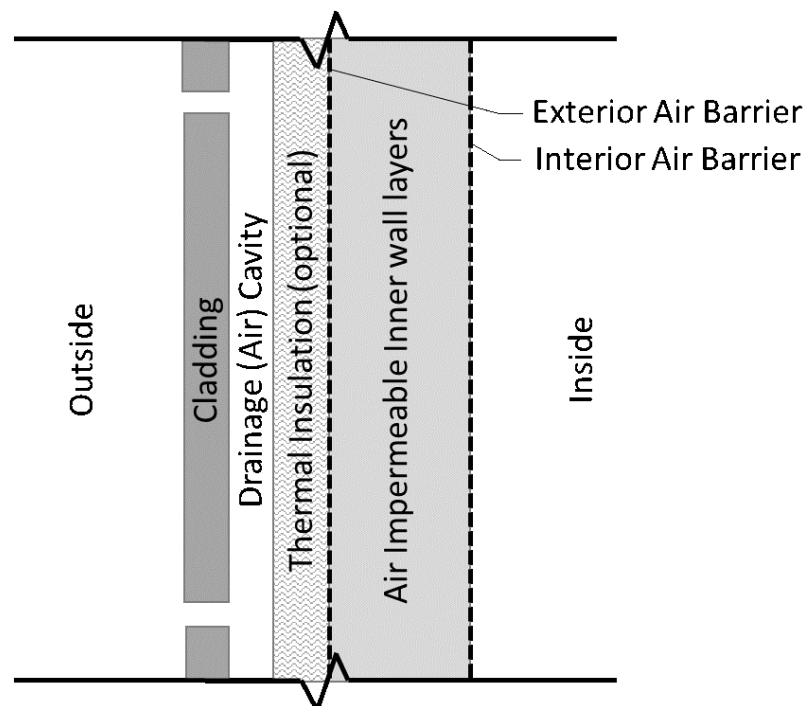
Figure 1: Definition sketch of a typical multi-layer wall system

Pressure equalization of vented wall cladding systems for wind loading considerations are investigated in this thesis. The importance of pressure equalization along with the related industry standards and the layout of the thesis components are presented in this chapter

1.1   Pressure Equalization in Cladding Standards

The terms "pressure equalization" or "pressure moderation" describe the reduction in net wind forces acting across layers of the building enclosure due to the rapid transfer of air pressures through intentional and/or unintentional openings (Straube and Burnett 1999).

The International Building Code (IBC) and the International Residential Code (IRC) require static pressure testing using ASTM D5206 *Wind Testing of Vinyl Siding* (2006). For this test, a plastic sheet is placed directly behind the cladding within the drainage (air) cavity to ensure all the suction pressure over the area of the wall is converted to a force on the siding. The suction pressure is generated by depressurizing a test chamber ("airbox") positioned over the outside of the cladding. The airbox pressure is stepped to greater and greater suction pressures until failure. IBC and IRC use ASTM D3679 *Vinyl Siding Specification* (2009) which allow 64% reduction of design wind loads used in ASTM D5206 testing. This reduction is based on pressure equalization measurements by ATI (2002). Their testing differed from ASTM D5206 in that it involved a rapid depressurization of the air box chamber and the plastic sheet was omitted allowing the pressure equalization across the cladding. This study found that under such test conditions the net pressure across the siding was, at most, only 18% of the peak external suction pressure due to this pressure equalization effect. The 18% was doubled to set the 0.36 multiplication factor (1.00-0.64) used in the ASTM D3679 standard.

ASTM D3678 does not allow the pressure equalization allowance when installed over a flexible surface. It has been suggested that installations over foam board sheathing can result in failures do to its flexibility (FEMA 2010). However, the NIST study (2006) found that vinyl siding wind damage occurred regardless of sheathing. Furthermore, numerous installation issues with vinyl siding have been identified as the potential source of failures during high wind events (FEMA 2010), adding additional complication.

Over a building exterior surface, pressures vary spatially and temporally due to wind and aerodynamic effects. The ASTM D5206 test standard disregards spatial variation. In this thesis, it will be shown that spatial surface pressure variations affect pressure equalization.

1.2   Thesis Outline

The objective of this study is to validate an available analytical model and determine where calibration is necessary. An accurate pressure equalization model will provide a tool for wall system designers to optimize designs. It may also support test standard development to ensure their effectiveness in reflecting actual field performance. Finally, it may be used in forensic investigations of cladding failures due to wind loading.

Chapter 2 presents a literature review of the current pressure equalization measurements and models. The review focuses on wall cladding systems but studies of roof pavers are also presented as the conditions have similarities.

Chapter 3 presents measurements of pressure equalization for a simplified full-scale cladding system and an analytical model to predict performance.

In Chapter 4 the results from full-scale wind tunnel tests by others of a small test building clad with vinyl siding are analyzed. This analysis includes investigation of spatial performance variation and measurement anomalies. The analytical model developed in Chapter 3 is then adopted to the test vinyl siding wall system. The model is then used to demonstrate optimization of vinyl siding design including modification necessary to meet the ASTM D3679 allowance.

In the final chapter, the major conclusions from the research are provided. Recommendation for vinyl siding wall system designs and further research are also presented in that chapter.

Chapter 2

2　Background

To assess pressure equalization effects on cladding systems a pragmatic approach would be to evaluate wind damage and exposure in the field after high wind events. However, that approach poses several limitations;

- It is difficult to accurately assess installation details of damaged assemblies, particularly installation defects;

- It is difficult to accurately assess the wind exposure during high wind events;

- It is difficult to assess the degradation of the assembly prior to the event; and

- Cladding and wall systems are constantly evolving and inevitably the damaged systems assessed in the field are considerably different from new systems of interest.

Controlled laboratory investigations allow evaluation of properly installed system and systems with given degradation or construction defects. Wind exposures can be controlled and repeated. New systems can be tested prior to use on buildings. The testing described in ASTM D5206 is a simplified approach for such testing.

Computer models can further be used to predict effects guiding designs. In this chapter, key published measurements related to pressure equalization of cladding systems are summarized. This is followed by a review of current analytical models for predicting pressure equalization across cladding systems. The limitations of this research as it applies to vinyl siding pressure equalization effects are summarized at the end of the chapter. The suitability of the testing which underlies the allowance in ASTM D3679 is discussed relative to the published research.

2.1 Wind Induced Pressure on Buildings

Wind is a perceptible natural movement of air. Large scale air circulation systems in the atmosphere are caused differences in solar exposure and the earth's rotation. Local severe winds can result from local convective effects (gales from large depressions, tropical cyclones, thunderstorms, tornados, and downbursts) or movement of air masses over mountains. For design of structures, wind speeds under design conditions are determined from extreme value analysis of weather station data and models informed by a host of information.

Wind speeds vary spatially and temporally during high wind conditions. Time averaged mean horizontal wind speeds, $\overline{U}$, are often used to express of spatial variations and simplify calculations. Building sit in on the earth's surface for which their significant mean vertical wind speed gradient, $\overline{U}(z)$, which vary with height, z. For engineering purposes, the profile is characterized as a power law (Holmes 2001) described as

$$\overline{U}(z) = \overline{U}_{10}(\frac{z}{10})^{\alpha} \tag{1}$$

where α is an exponent dependent on terrain roughness and assume wind speeds are measured at 10m. The power law is used with a given boundary layer thickness which also depends on terrain.

The time varying component of wind speeds can be described by spectral density function. The von Karman-Harris (described in Holmes 2001) is a common mathematical expression for the longitudinal velocity component and given in Figure 2.
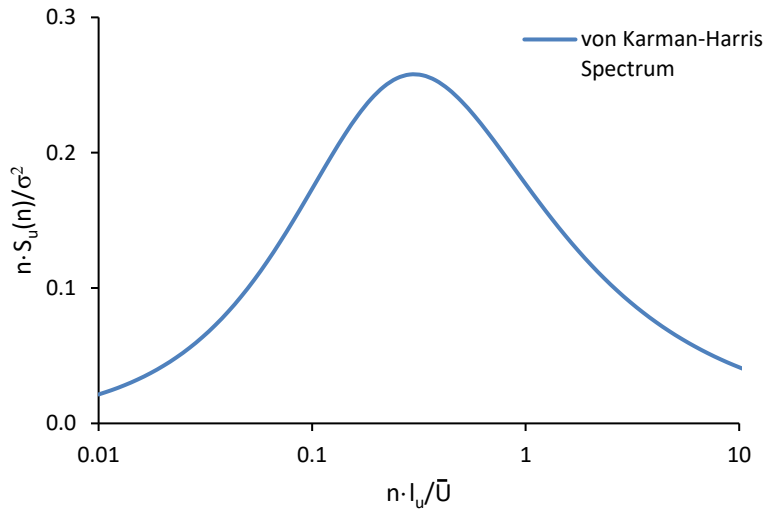
Figure 2 Normalized spectrum of longitudinal velocity component (von Karman-Harris)
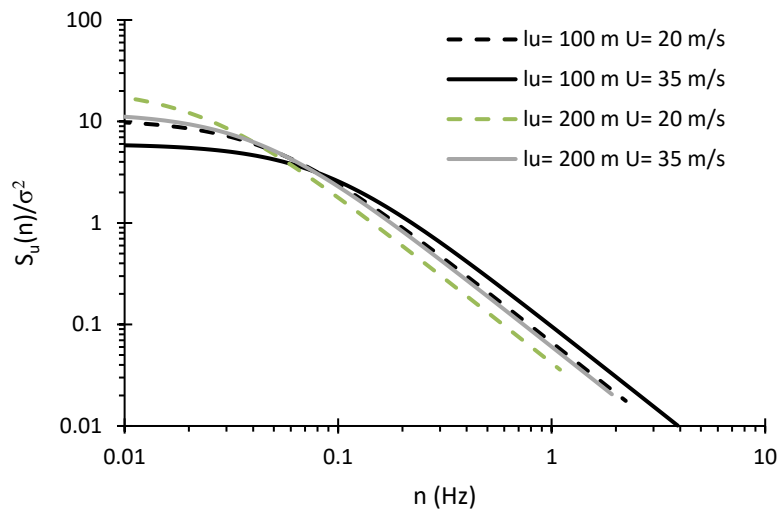
Figure 3 Calculate spectrum of longitudinal velocity component (von Karman-Harris) based on turbulence lengths of 100 and 200m and 20 and 30 m/s average wind speeds

Flow past buildings or other bluff bodies is characterized by a stagnation on the wind ward surface. This behavior has been found to create positive pressures approaching the combined static and dynamic pressure in Bernoulli's equation as follows:

$$p_{atm} + 0.5\rho U^2 = p \qquad\qquad (2)$$

Mean surface pressures are described by non-dimensional mean pressure coefficients, $\bar{C}_p$:

$$\bar{C}_p = (p_e - p_o)_{mean}/(0.5\rho\bar{U}_W^2) \tag{3}$$

where p_0 is the air pressure outside the influence of the building, ρ is the air density, and $\bar{U}_W$ is the mean windspeed. Windward $\bar{C}_p$ values approach 1.0 on windward faces of bluff bodies due to stagnation.

The wind accelerates around the sides of building resulting in negative suction pressures. For low rise houses with sloped roofs, $\bar{C}_p$ values reach -0.6 close the windward wall edges. (Swami and Chandra 1987). Furthermore, eddies formed beyond the separation edges are unstable and will roll up towards the wake to form concentrated vortices, which are subsequently shed downwind. This phenomenon results in temporal variation of the pressures within the separation bubble. Hence, the variation of pressures in separation tend to be large than those only influence by the gusts in the wind. This results in peak pressure coefficients reaching -3 within the separation bubble (Homes, 1994) which tend to be design loads for residential cladding.

Models to predict the impact of winds on pressures across cladding systems including the impacts of the spatially and temporally varying surface pressures are reviewed in the remainder of this chapter.

2.2 Measurements of Pressure Equalization

There are several approaches to pressure moderation measurements that have been pursued by others and will be reviewed in this chapter. The dimensional nomenclature used in this study is illustrated in Figure 4.
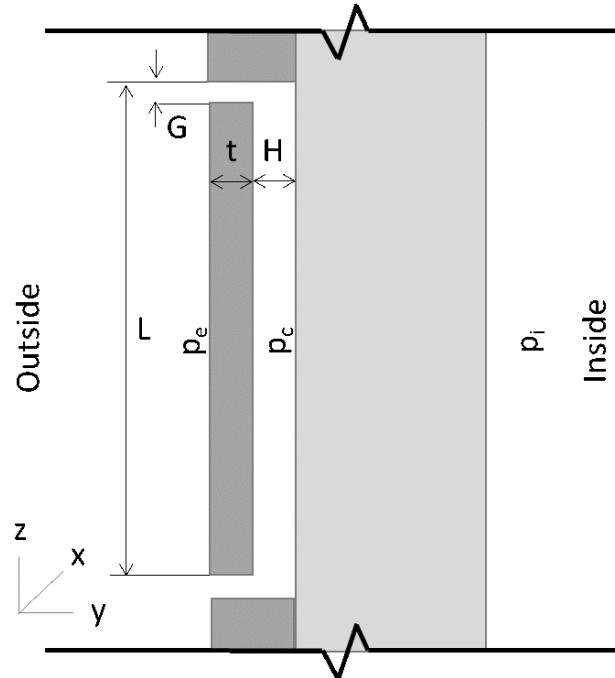
Figure 4: Wall cladding schematic with dimension nomenclature

Instantaneous pressure equalization factor, PEF, is determined for cladding as

$$\text{PEF} = \frac{\text{pressure drop across cladding}}{\text{pressure drop across wall}} = \frac{p_e - p_c}{p_e - p_i}. \qquad (4)$$

Hence, high PEF values equate to cladding taking most of the wind induced pressure and low PEF values equate to the cladding taking little of the force. Within the discussion of vinyl siding wind loads in Chapter 2 the ATI study (2002) measured a PEF values of 0.02 to 0.18 in their test. The high value was doubled to a PEF of 0.36 for use in ASTM D3679 (2009).

2.2.1   Field Measurements

Researchers have used differential surface pressure measurements over cladding systems to calculate cladding ventilation rates as part of moisture drying and wind washing studies (Uvslokk 1996, Straube 1999). Recent studies investigating ventilation drying have monitored ventilation rates using tracer gas and/or hot wire anemometers (Gudum 2003, Bassett and McNeil 2009). However, these measurements did not capture high wind conditions.

Gerhardt and Janser (1994) measured wind pressures across open-joint cladding panels on an office building to investigate pressure equalization effects. The monitored panels were adjacent to building corners where high horizontal pressure gradients occur. The conditions of the cladding panels were modified part way through the monitoring to seal the cavities behind the cladding at the panel's vertical edges. They found this modification encouraged pressure equalization by limiting vertical flow behind the cladding allowing cavity pressures to better follow the coincident outer surface pressure. However, trim at building corners for siding clad residential walls provide a vertical separator to avoid such affects.

Van Benton and Geurts (2015) published pressure equalization measurements for a 150m tall building in Rotterdam, taken when wind speeds exceeded 6m/s. They measured PEF values based on the maximum net cladding pressures relative to maximum net wall pressures both calculated from extreme values analysis for winds from the same direction. This was done in lieu of using instantaneous values. Since the maximum net cladding pressures may not be temporally coincident with the maximum net wall pressures this approach would be expected to introduce some error. They found a maximum PEF of 0.8. The study was focused on cornering effect with open cladding vents at corners only which is different than vinyl siding systems with vent openings mostly along the length of walls.

2.2.2   Wind Tunnel Measurements

Bienkiewicz and Sun (1992) conducted wind tunnel testing for a low-rise building with a flat roof covered with roof pavers constructed at a 1:25 geometrical scale. They included two pressure taps on top and two below each roof paver. When no intentional space was left below the pavers it was essentially pressure equalized (i.e., the PEF was close to 0). When this cavity space depth, H, was raised and made equivalent to a quarter the paver thickness, l, the pressure distribution underneath was more uniform and attenuated, resulting in less pressure equalization. Bienkiewicz and Sun's (1997) study included variation of the spacing between the pavers, G, finding that reducing this spacing had a similar effect of reducing pressure equalization as increasing the cavity depth.

Gerhardt and Janser (1994) conducted wind tunnel tests on a scaled building with claddings with varying air permeability and air cavity depths. They found similar results as Bienkiewicz and Sun (1992) where increasing the cladding air permeability and/or decreasing the cavity depth reduced cladding wind loads by encouraging pressure equalization. They also compared mean measurements from field monitoring (summarized in section 2.1.1) with wind tunnel measurement for a scaled model. They generally found poor agreement and suggested it was due to sensitivity to minor differences in gap flow resistance between the two cases.

Van Bentum et al. (2012) conducted wind tunnel tests on a 600mm cube structure exposed to low turbulence smooth air velocities of around 15 m/s. The cube had a cladding with 4, 8, and 16mm wide orifice openings at the edges only. They measured the highest net cladding pressures for the most open 16mm gap width case. The 4 and 8mm gap widths resulted in similar lower pressures. They also varied the cavity depths to 10, 20, and 40mm and found that the 10mm cavity resulted in the highest net pressures. Both findings were opposite to expectations and thought by the authors to be due to cornering effects or that an even greater range of dimensions is necessary to show the expected effect. However, the smooth "wind" exposure, the presence of cladding openings at corners only, and the large relative scale of the cladding gap and cavity were all non-typical and may cause the difference in findings from systems with distributed openings and realistic exposures.

Aly and Bitsuamlak (2013) measured wind loading on solar panels on two pitches of residential roofs and found increase suction loads due a "secondary roof" effect where the position of panels over on the roof affected the loading even with the same roof slope. Warsido et. al. (2014) furthered the wind tunnel study to investigate the effects roof mounted solar array spacing from the roof edge. They found that increasing the distance reduced loading but did not specifically investigate spacing between panels or cavity depths underneath.

Oh and Kopp (2014) conducted wind tunnel testing on roof solar panels with ratios of gap orifice spacing, G, to cavity depth, H, varying over the range $1/30 \leq G/H \leq 30$, and

panel thicknesses, l, over a range $0.53 \leq l/G \geq 16$. The study incorporated 7 taps per panel (between the gap orifices), which was a greater pressure tap density than previous studies. Cavity pressures were uniform when the orifice flow resistance across the panels was high relative to the cavity flow resistance (i.e., G/H was low) and a linear pressure drop along the cavity was found when the cavity flow resistance below the pavers was relatively high (i.e., G/H was high). A reduction in peak panels loads was attributed to the second condition, which is a similar finding as that by Bienkiewicz and Sun (1992) and Gerhardt and Janser (1994).

Errors introduced by scaling (which is necessary to capture flow behavior over entire structures) is a potential limitation of typical wind tunnel testing. The model buildings in most wind tunnels are required to be constructed to, at most, a 1:25 scale. With this reduction in size, it is physically difficult to accurately construct scaled cladding systems. Furthermore, scaling down cavities behind the cladding result in Reynolds effects where cavity air flow is forced laminar and/or flow structures developed at flow separation are modified by the greater relative strength of viscous to inertial forces when sealed.

Mooneghi et al. (2014) conducted testing using a facility with large fans to allow testing of a 1:2 scale building with roof pavers. The facility can reproduce high frequency wind gusts (greater than 1hz) by placing large spires between the fans and the test structure but not lower frequencies. Tests were done with G/H ratios of 0.028, 0.083, and 0.25 and the published results included mean and peak net pressure across the pavers. The results show that increases to G/H ratio decreased mean and peak net pressure across the pavers and that for low G/H ratios the pressures below the pavers become more uniform as found in previous studies. The decrease in net pressures was greater than for the mean than peak pressures.

The general finding of wind tunnel testing and the 1:2 scale testing is that cavity pressure become uniform when the cavity flow resistance is low relative to orifice flow resistance. This phenomenon clearly has a negative impact on pressure equalization. It should be noted that this effect would not be captured in the standard testing summarized in Section 1.1 because such tests do not incorporate spatial pressure gradients.

2.2.3   Full-Scale Measurements Using Air Boxes

The "airbox" approach used in ASTM D5206 testing was modified utilizing Pressure Load Actuators (PLAs) to allow replication of temporally realistic wind pressures as described by Kopp et. al. (2010). The design specifications for PLAs was to reach +5kPa to -15kPa with fluctuations as high as 4 Hz which the researchers found were needed to capture unsteady pressure fluctuations for roof surfaces within separation bubbles under high wind event conditions hour houses. Gavanski and Kopp (2012) found low PEF values similar to ATI (2002) when testing full-scale vinyl siding clad wall assemblies using PLAs. This testing was repeated by NAHB (2014) for a wider array of wall system with similar results. To incorporate spatial variation Miller et al. (2017) have developed an approach utilizing multiple air boxes attached to vinyl siding with flexible latex sheets to allow separation with limited constraint of siding deflection. The airboxes were controlled to varying pressures, and given adequate controls and PLA fan power, achieved airbox pressures following realistic high wind conditions. They measured higher PEF values than Gavanski and Kopp (2012) and NAHB (2014).

2.2.4   Full-Scale Wind Tunnel Measurements

A full-scale wind tunnel has been built by the Institute for Business and Home Safety (IBHS) which can replicate high wind conditions for small low-rise buildings (Morrison et al., 2012). Several studies have been conducted at the facility to measure wind loading and wind load resistance for building systems. One study (Cope et al., 2012) measured pressures at the outer surface of vinyl siding, cavity, batt space, and building interior for high wind conditions. PEF values derived from these measurements were 75 to 80% for the vinyl siding, 55 to 60% for the sheathing, and 50 to 60% for the drywall at peak design (suction) loads.

Moravej et al. (2016) measured pressures across vinyl siding installed on a small 2.43m by 2.74m gable roofed structure on turn table exposed to high wind from large fans with a series of spires to generate turbulence and vertical velocity gradient. Within this study the vinyl siding was installed over plywood sheathing with a felt paper weather resistive barrier. Vinyl siding surface and cavity (between the felt paper and vinyl siding)

pressures were measured at the gable roof end wall. The greatest suction pressures were found when the monitored wall was mounted at 80° to the wind. Wind loading was calculated using two approaches. In one approach, the peak measured cladding surface and cavity pressure coefficients were compared to determine the net peak pressure coefficient. Using this approach resulted in very low net peak pressure coefficient. However, as these peak pressures may not have been coincident, the authors suggested the approach may not have captured the actual net peak loading on the vinyl siding. They further measured instantaneous point PEF (suction) values of 71 to 106% and calculated instantaneous PEFs values for $1m^2$ tributary area of 40% to 75%. These values are more in line with those measured Cope et al. (2012). However, they did not report PEF values coincident with peak suction pressures. Hence, the results are presented cannot be directly compared to those measured by Cope et al. 2012. The values, however, are greater than those used in ASTM D3679 providing further evidence the current design standard underestimated wind loads on vinyl siding products. Furthermore, the Moravej et al. study monitored pressure on the gable end wall while Cope et al.'s measurements were on the side wall. Ideally both walls would be monitored to capture the highest suction loads.

2.3   Analytical pressure equalization models

Vented cladding systems consist of several openings or orifices in the cladding connecting to a cavity underneath. In this section, flow through orifices will be discussed first, followed by pressure equalization models for spaces (cavities) with large open internal volumes, flow through cavities, and finally models of cavities with multiple exterior orifice openings. Simplifications used in these models and findings relating to pressure equalization are presented. Loss coefficients for a variety related conditions will be presented, including measured values for actual vinyl siding.

2.3.1   Orifice flow

The pressure drop across a sharp-edged orifice for a given average orifice fluid velocity, v, and assuming a constant cross-sectional area through the length of the orifice can be calculated from the Bernoulli equation (assuming steady, incompressible flow and the

gravitational effects are negligible) with a loss coefficient, C_l, to account for flow separation energy losses as

$$p_i + C_l \cdot 0.5\rho v^2 = p_e \tag{5}$$

where ρ is the fluid density and v is the average fluid velocity within the orifice (assuming a constant cross sectional area through the length of the orifice).

Alternatively, the equation can be written in terms of flowrate, Q, as

$$p_i + C_l \cdot 0.5\rho\left(\frac{Q}{A}\right)^2 = p_e \tag{6}$$
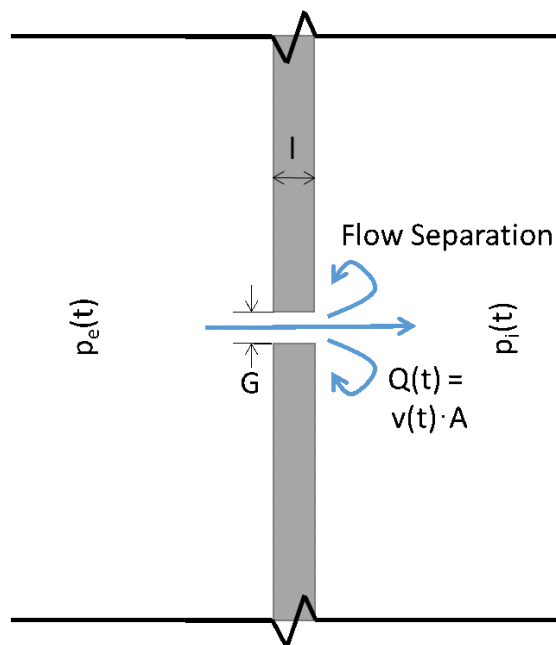
Figure 5: Illustration of Simple Orifice Flow

Alternatively, the equation can be rearranged to calculate flowrate or fluid velocity and use a discharge coefficient, k, to account for losses such that

$$v = k\left(\frac{p_e - p_i}{0.5\rho}\right)^{0.5} \text{ (i.e., } k = \sqrt{1/C_l}\text{)} \tag{7}$$

Researchers have measured a Reynolds number, Re_D, dependency of the discharge coefficient for circular orifices which have been summarized by Idelchik and Fried

(1986). These vary from 0.60 up to 0.67 and back down to 0.60 between Reynolds numbers of 5 to 1,000,000. For Reynolds numbers, Re_D, in the range of 1,000 to 10,000 discharge coefficients from 0.65 to 0.68 such that

$$k = 0.59 + \frac{0.27}{Re_D^{1/6}} \tag{8}$$

where

$$Re_D = \frac{\rho D v}{\mu} \tag{9}$$

and D is the diameter of opening and μ is the fluid dynamic viscosity.

For non-circular opening and ducts, Re_{D_h}, can be calculated as

$$Re_{D_h} = \frac{\rho D_h v}{\mu} \tag{10}$$

where the hydraulic diameter, D_h, for a slender slot (W>>G) can be calculated as follows

$$D_h = \frac{4 \cdot area}{wetted\ perimeter} = \frac{4 \cdot G \cdot W}{2G+2W} = \sim 2G \tag{11}$$

If the flow path through the opening is "tortuous" then wall shear stresses (i.e., frictional forces) are dominant and the pressure drop follows that for pipe-friction which can be calculated using the Darcy-Weisbach equation (Munson et al. 1998):

$$p_e - p_i = f \cdot 0.5\rho v^2 \cdot \frac{l}{D_h} \tag{12}$$

where l is the orifice length and f is friction factor. For laminar flow, the friction factor can be calculated for circular pipe openings (White 2011) as

$$f = \frac{64}{Re_D} \tag{13}$$

For flow between parallel plates, friction factor has been found (White 2011) to be

$$f = \frac{96}{Re_{Dh}} \tag{14}$$

Using this relationship, the fluid velocity can be calculated from equations (11) and (13) as follows:

$$v = \frac{D_h^2}{48\mu l}(p_e - p_i) \tag{15}$$

Hence, laminar flow velocity through openings is linearly proportional to the driving pressure difference. This aligns with Darcy's Law for flow through porous media (White 2011).

For flow between parallel plates the hydraulic diameter is equal to twice the distance (see equation (10)) between the plates and hence the equation can be further simplified to

$$v = \frac{G^2}{12\mu l}(p_e - p_i). \tag{16}$$

Friction factors for fully-developed turbulent flow depend on Reynolds number and surface roughness. Measurements by Beavers et al. (1971) found, for flow between smooth parallel plates that friction factors followed

$$f = 0.507 Re_{D_h}^{0.3}. \tag{17}$$

A study of critical Reynolds number (where flows transition from laminar to turbulent) between smooth parallel plates (Minkowycz 2009) found that, for flat and parabolic inlet profiles with entering turbulence intensities of 1%, the friction factor transitioned from following equation (13) to equation (16) at Reynolds numbers of 10,000. For an entering flow turbulence intensity of 5%, similar results were found for parabolic entering profile. For the flat entering profile, the friction factor followed equation (13) until a Reynolds number of 3000 and transitioned to follow equation (17) at a Reynolds number of 8000. For air flowing from orifices into perpendicular cavities (of interest in this study), the entering flows would have turbulence due to flow separation as it turns into the cavity and, further, would have a profile that is neither flat or parabolic. The critical Reynolds number for this scenario is unknown, but the study by Minkowycz (2009) suggests that it can be higher than the value of 2030 measured by Reynolds (see White, 2011) for flow in pipes.

Laminar flow through slot orifices can be modelled as the summation of discharge and friction losses (equations (5), (10), and (15)) such that

$$p_e - p_i = C_l \cdot 0.5\rho v^2 + \frac{12\mu l}{G^2} v \tag{18}$$

Another modelling option worth noting, due to its common use, is the Power Law where

$$v = C_p(p_e - p_i)^n \tag{19}$$

where n is a flow exponent with values close to 1.0 for long tortuous flow paths where the wall friction dominates (the second term in equation (17)) and values close to 0.5 occur where flow separation dominates (the first term in equation (17)). The dimensions of the coefficient would need to vary with the exponent which complicates the equation.

For unsteady flow, either a quasi-steady assumption can be made or an inertial term can be added. The quasi-steady assumption treats unsteady flows as steady flow for each instant in time (Munson et al. 1998) and utilizes mean coefficient values (Holmes 2001). The inertial term will be discussed section 2.3.2.

Ginger and Kim (2012) and Straube and Burnett (2001) have reported reductions in orifice flow discharge coefficient under unsteady 5 Hz and 1 Hz sinusoidal driving pressures, respectively. In both studies, the mean pressure and flow rate were used to calculate the discharge coefficient. Earles and Zarek (1963) studied the error with this approach for sharp-edged orifices used for metering pulsating pipe flow. They described a 'square-root-mean' non-linearity error for time varying pressures when such flowrates are calculated as follows:

$$\frac{1}{t}\int_0^t (p_e(t) - p_i(t))^{0.5}dt \neq \left[\frac{1}{t}\int_0^t (p_e(t) - p_i(t))dt\right]^{0.5} \tag{20}$$

This same error applies to the calculation approach used in orifice flow measurements. To calculate the impact of the square-root-mean error in these studies an adjusted discharge coefficient, k', has been calculated as follows:

$$k' = \bar{v} / \left[\sqrt{0.5\rho}\frac{1}{t}\int_0^t \left(\overline{(p_e - p_i)} + P \cdot \sin(2\pi ft)\right)^{0.5}dt\right] \tag{21}$$

where P is the the amplitude of a varying sinusoidal pressure trace with a frequency, f.

Equation 17 can be solved numerically using the trapezoid rule over a complete sinusoid cycle for various ratios of the pressure amplitude to the mean pressure difference and is plotted in Figure 6 and labelled "Num. Analysis". The results suggest that the 'square-root-mean' error explains most of the perceived reduction in discharge coefficient reported by Kim and Ginger (labelled with author names) and Straube and Burnett's (the remaining data points labelled for different vent screen product types). The results suggest that, for their test scenario, inertial effects have negligible impact on air flows. It is noted that Straube and Burnett's greater values for open brick joints are unexplained.
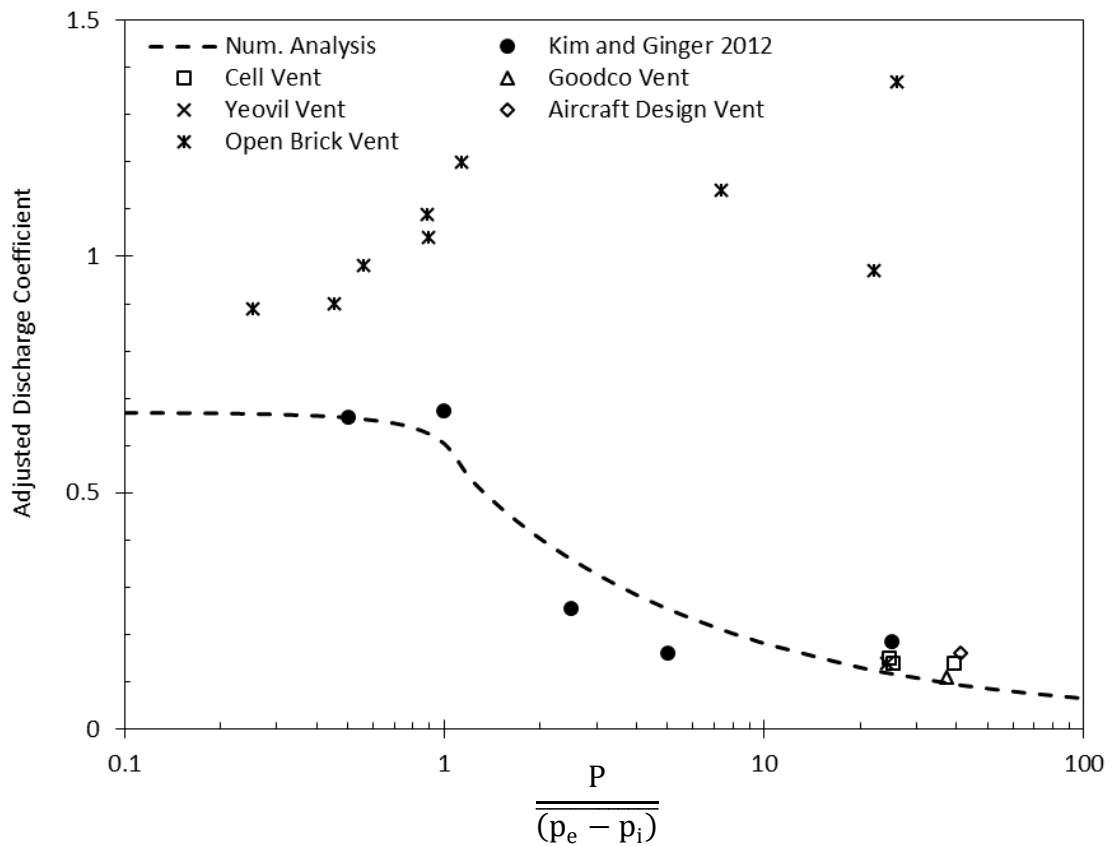
Figure 6: Comparison of numerical analysis results and values from Ginger and Kim (2012) and Straube and Burnett (2001)

2.3.2　Internal Building Pressures

Analytical models used in many studies for predicting performance of pressure equalized rainscreens are summarized by Kumar (2000). Many of these are like internal building pressure models in that they assume negligible losses for flow within the internal volume (cavity), as illustrated in in Figure 7.
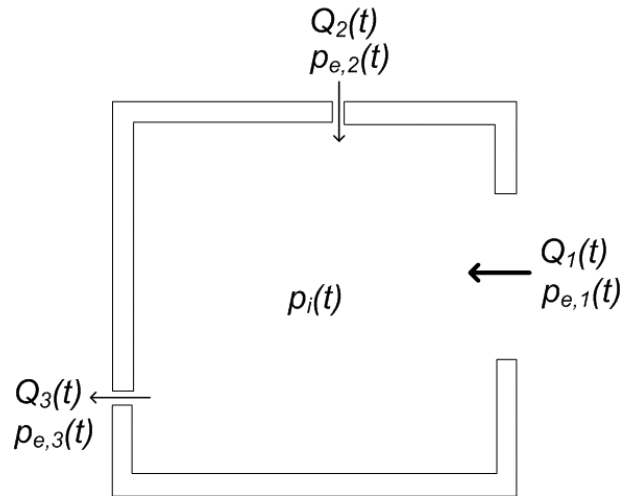
Figure 7: Example internal building pressure model with dominant opening

Assuming steady, incompressible flow, the net flow, Q, in and out of the volume, through the N openings, follows conservation of mass.

$$\sum_{j=1}^{N} \rho Q_j = 0 \tag{22}$$

Using the power law to model flow through each opening and assuming a relatively large volume with uniform internal pressure this equation can be rewritten as

$$\sum_{j=1}^{N} \rho \cdot A_j \cdot C_{p,j} \left(p_{e,j} - p_i \right)^{n_j} = 0 \tag{23}$$

where A_j is the area of openings. This approach can be applied to unsteady flow scenarios by assuming the quasi-steady state when inertial and compressibility (elastic) effects on the flow behaviour are negligible (Etheridge 2000).

Gudum (2003) compared cavity velocity measurements under low wind conditions (<6m/s) to a QS model with entrance and exit orifice losses model using equation (22). The wall system had a 25mm open cavity with upper and lower slot orifice vents. The cavity was assumed to contribute negligible flow resistance relative to the vents. The model predicted the ventilation flow rates within +/- 50%. The author attributed this error to driven wind pressure measurement uncertainty.

Vickery (1986) proposed an effective "slug" length, l_e to capture unsteady effects for orifice openings to large volumes as follows:

$$p_e - p_i = C_l \cdot 0.5\rho v^2 + \rho l_e \frac{\partial v}{\partial t} \qquad (24)$$

where $\frac{\partial v}{\partial t}$ is an acceleration term (it is a partial derivative because also varies spatially across the width of the orifice). He estimated the slug length as a function of orifice depth and width for square openings from wind tunnel measurements as the smaller of

$$l_e = l + 0.86G \qquad (25)$$

Or, for flow entering a relatively shallow perpendicular cavity,

$$l_e = l + H \qquad (26)$$

Laminar flow based orifice wall friction losses were added to equation (20) by Oh et al. (2007) as follows:

$$p_e - p_i = C_l \cdot 0.5\rho v^2 + \frac{48\mu l}{D_h^2} v + \rho l_e \frac{dv}{dt} \qquad (27)$$

Oh et al. (2007) modified the discharge term to utilize a variable flow exponent as part of fitting their experimental data as follows:

$$p_e - p_i = \left(\frac{1}{k}\right)^{1/n} (0.5\rho)^{1/2n} v \cdot |v|^{(1/n)-1} + \frac{48\mu l}{D_h^2} v + \rho l_e \frac{dv}{dt} \qquad (28)$$

They applied this equation for each orifice opening, along with an equation for conservation of mass within the volume (equation 21), in what they termed the Multiple

Discharge Equation (MDE) approach. The model accurately predicted internal pressures measured in wind tunnel testing irrespective of shifts of wind direction and upstream terrain impact on approaching wind velocity gradients and turbulence. However, the equation is complex because flow exponent, n, results in the discharge coefficient needing variable dimension units (similar to the power law equation). The model further cannot be used for cladding systems because it does not address cavity losses.

2.3.3   Cavity flow

Viscous flow through a thin cavity can be characterized as Couette flow (Currie 1974) which is flow between parallel plates. The Navier Stokes equations can be simplified for fully developed, laminar, incompressible, irrotational, steady flow with no gravity effects using the nomenclature in Figure 4, as

$$0 = -\frac{dp}{dx} + \mu \frac{d^2 u}{dy^2} \tag{29}$$

There will be a velocity gradient through the cavity depth direction, y, due to the wall shear stress. Integrating the equation twice with respected to y and solving the integration constants from the boundary conditions, $u(0) = u(H) = 0$, reveals a parabolic equation for the velocity across the cavity.

$$u(y) = \frac{1}{2\mu} \frac{dp}{dx} (y^2 - yH) \tag{30}$$

where pressure gradient along the cavity length, $\frac{dp}{dx}$, is constant. From this equation, we can find that the flow rate as

$$Q = \int_0^H u(y)\, dy \tag{31}$$

where substituting equation (29) results in

$$Q = \int_0^H \frac{1}{2\mu} \frac{dp}{dx} (y^2 - yH) \cdot dy = -\frac{H^3}{12\mu} \frac{dp}{dx}. \tag{32}$$

This can be rearranged to be expressed as a pressure drop over the cavity length, L, as

$$(p_{x=0} - p_{x=L}) = \frac{12\mu vL}{H^2} \qquad (33)$$

This equation is like equation (15) for slot orifice wall friction losses because the wall friction losses dominate in both scenarios.

Shear stress for this scenario can be calculated as

$$\tau(y) = \mu\frac{du}{dy} = \frac{1}{2}\frac{dp}{dx}(2y - H) \qquad (34)$$

and solved at the wall surface $(y = 0)$ as

$$\tau(y = 0) = -\frac{H}{2}\frac{dp}{dx} \qquad (35)$$

If a friction factor, f, is introduced such that (Potter and Wiggert 2002)

$$f = \frac{8 \cdot \tau(y=0)}{\rho u^2} \qquad (36)$$

Equations (32), (34) and (35) can be combined such that

$$f = \frac{8}{\rho u^2}\left(-\frac{H}{2}\frac{dp}{dx}\right) = \frac{8}{\rho u^2}\left(-\frac{H}{2}\right)\left(-\frac{12\mu uL}{H^2}\right) = \frac{48\mu}{\rho Hu} \qquad (37)$$

For Reynolds number based on hydraulic diameter of a slender cavity, Re_{2H} (see equation (10), the equation can be rewritten as

$$f = \frac{96}{Re_{2H}} \qquad (38)$$

This equation is like equation (13) for wall friction losses for flow through slender slot orifices. Friction factor is used in the Darcy-Weisbach equation for flow between parallel plates as follows

$$P_{c,x=0} - P_{c,x=L} = f \cdot 0.5\rho u|u| \cdot \frac{L}{2H} \qquad (39)$$

For unsteady flow, the acceleration term, $\frac{\partial u}{\partial t}$, is retained in the Navier-Stokes equations. Given a sinusoidal, pulsating driving pressure, $p(t) = P \cdot \sin(2\pi ft)$, Currie (1974) provided an exact solution for this case in the form of

$$u(y,t) = \text{real}\left[\left(1 - \frac{\cosh\left[(1+i)\sqrt{\frac{2\pi f\rho}{2\mu}}\cdot y\right]}{\cosh\left[(1+i)\sqrt{\frac{2\pi f\rho}{2\mu}}\cdot\frac{H}{2}\right]}\right) \cdot e^{i2\pi ft}\right] \tag{40}$$

where real $[\ldots]$ indicates the real component and *i* is sqrt(-1).

The unsteady effects for highly oscillating flows with relatively low viscous (friction) forces result in Richardson annulus effect (Richardson and Tyler 1929), which is a non-parabolic velocity gradient across the cavity cross section as plotted in Figure 8.
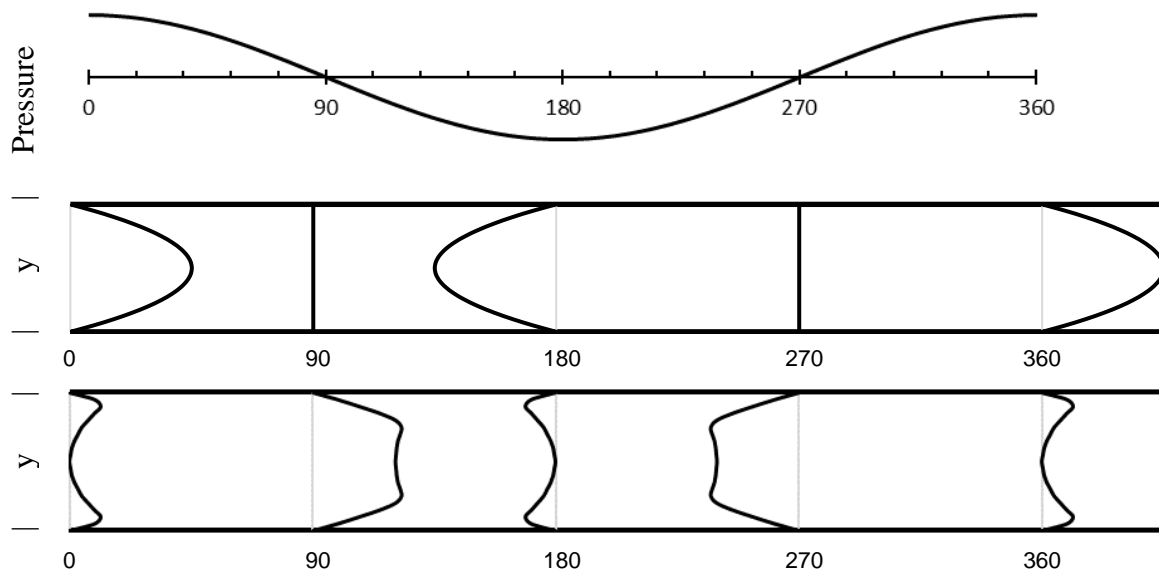
Figure 8: Sinusoidal pressure signal (top), velocity profiles for flow between parallel plates a 90° phase steps assuming negligible inertial effects or quassi-steady (middle), and unsteady velocity gradients between parallel plate with Richardson annulus effects (bottom)

Yakhot et al. (1999) gave a numerical solution to these velocity profiles across the cavity for unsteady flows as follows:

$$u(y,t) = A(y)\cos(2\pi ft) + B(y)\sin(2\pi ft) \tag{41}$$

where

$$A(y) = \frac{P}{\rho 2\pi f} \cdot \left[\frac{\cosh(yC)\cdot\cos((H-y)C)+\cos(yC)\cdot\cosh((H-y)C)}{\cosh(HC)+\cos(HC)} - 1 \right] \tag{42}$$

$$B(y) = \frac{P}{\rho 2\pi f} \cdot \left[\frac{\sinh(yC)\cdot\sin((H-y)C)+\sin(yC)\cdot\sinh((H-y)C)}{\cosh(HC)+\cos(HC)} \right] \tag{43}$$

where

$$C = \frac{\rho 2\pi f}{2\mu} \tag{44}$$

They introduced a cavity velocity phase shift term, $\varphi_u(y)$ calculated as follows:

$$\tan(\varphi_u(y)) = \frac{A(y)}{B(y)} \tag{45}$$

They also calculated the mean value of this term across the cavity depth relative to a non-dimensional number describing the ratio of oscillating forces to viscous forces. This non-dimensional term is like the Roshko number, Ro, (Ormieres and Provansal 1999) which is calculated as follows:

$$Ro = Re \cdot St = \frac{\rho Hu}{\mu} \cdot \frac{2\pi fH}{u} = \left(H\sqrt{\rho 2\pi f/\mu} \right)^2 \tag{46}$$
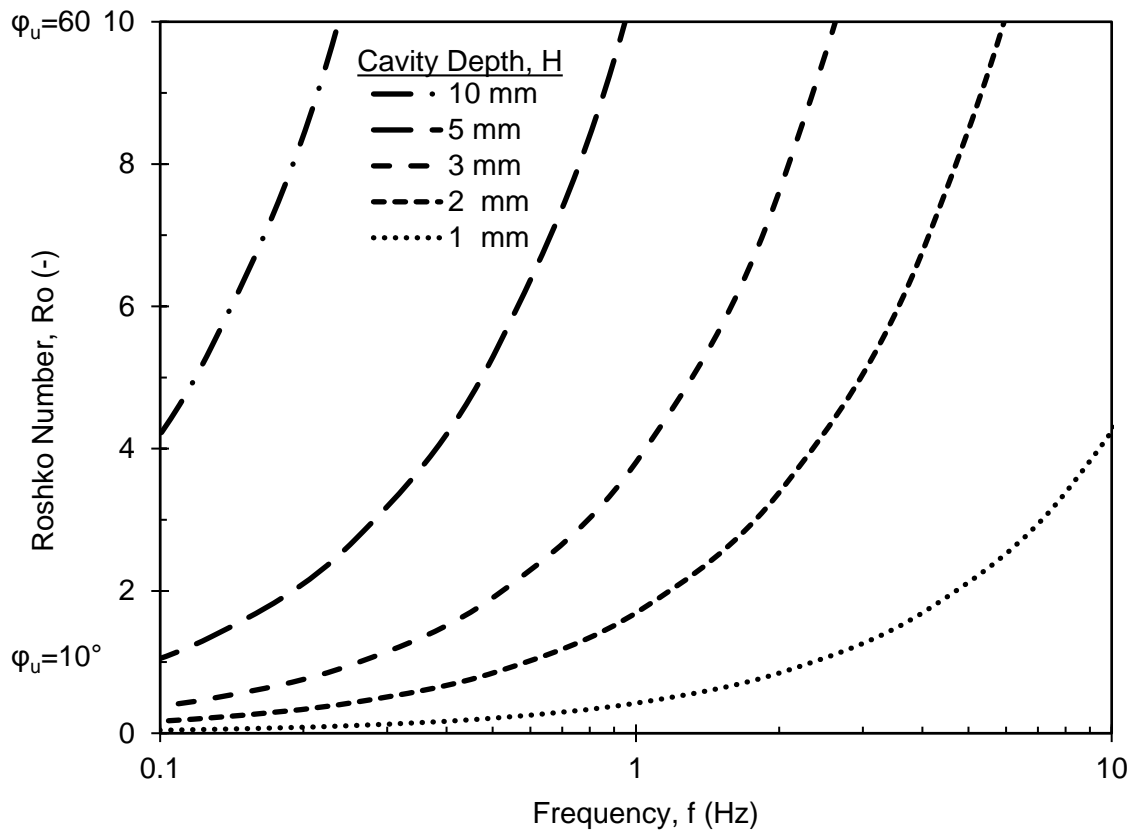
Figure 9: Plot of Roshko number as a function of frequency and cavity depth

Yakhot et al. (1999) predicted that for wide cavities (width, W, is much greater than depth, H), a (10°) phase shift at Ro = 1 and phase shifts exceeding 60° at Ro= 10. Roshko numbers are plotted in Figure 9 as a function of frequency for air flow through slender cavities of varying depths. For a shallow 1mm cavity, pulsating frequencies greater than 2Hz reach Roshko numbers of 1. For a deep 10mm greater cavity depths $10°$ phase shifts are expected even for low frequency pressure changes. During scaled wind tunnel testing the cavities behind cladding are quite shallow and hence this phenomenon may be inhibited in such testing and be issue for validation of pressure equalization models.

2.3.4   Cavities with Orifice Openings

Sun and Bienkiewicz (1993) put forth a numerical model for predicting the mean pressure distribution between and below roofing pavers. They applied Darcy's law (like

equations (12) and (29)) for flow through gaps in the pavers with gap widths, G, and along the cavities underneath the pavers with cavity depths, H. Within their model, the pressure equalization across the paver increased with higher G/H ratios and matched well with the mean pressure coefficient measured in their wind tunnel study (Bienkiewicz and Sun (1992)). However, they did not provided comparison to RMS or peak values so it is unclear how accurately their model predicts design wind loads.

Bofah et al. (1996) presented a similar model of flow under roof pavers and wall cladding. They used the sharp-edged orifice equation to model the flow through porous pavers and cladding. Their findings were similar Sun and Bienkiewicz (1993) in that G/H ratios had a positive correlation with pressure equalization and good agreement for mean pressures.

The two models both assume quasi-steady (QS) conditions. As RMS and peak pressures were not reported in their studies, it is unclear if the QS model is accurate for wind load design applications.

Oh and Kopp (2014) adapted the MDE model for ventilated cavities behind roof mounted solar panels. The orifice flow equations were updated for a constant flow exponent (addressing the dimensional complication) as follows:

$$p_{e1} - p_{c1} = C_l \cdot 0.5\rho v_1 |v_1| + \frac{48\mu l}{(2G)^2} v_1 + \rho l_e \frac{dv_1}{dt} \tag{47}$$

The effective slug length, l_e, was calculated per equations (24) and (25) and a constant loss coefficient, C_l, of 2.5 was used.

Cavity flow losses were calculated as follows:

$$p_{c1} - p_{c2} = \frac{48\mu L}{(2H)^2} u_1 + \rho L_e \frac{du_1}{dt} \tag{48}$$

where viscous (wall friction) losses are considered along with inertial effects using the cavity length, L, as the effective slug length, L_e.

Equations (45) and (48) along with accompanying MDE model continuity equations were solved numerically. Mean pressures were predicted within +/-5% but 5% to 15% higher RMS pressure values were predicted relative to accompanying wind tunnel measurements. The author proposed that RMS error was caused by the external pressures having been measured close to the opening and influenced by flow entrainment at the orifice openings. Vickery (1986) found that relatively large orifice openings can influence external pressures on wind tunnel models of buildings due to aerodynamic "flow through" effects. To limit the impact of these effects on the measurements they used span-wise averaged external pressures in lieu of point measured pressures. However, the pressure taps they used for these calculations were quite far from the vents and resulted in a high degree of attenuation of predicted RMS pressures. Oh and Kopp (2014) conducted further wind tunnel testing of a greater range of G and H combinations with greater pressure taps density to further explore these issues and further analyze the contributions of the inertial term for the orifices and the cavities. The inertial terms have a negligible impact on mean pressure predictions which may explain why Sun and Bienkiewicz (1993)'s and Bofah et al. (1996)'s quassi-steady models accurately predicted mean wind tunnel measurements. Predicted time series pressures were also analyzed showing that the inertial term is high for rapidly fluctuating and peak pressures. Furthermore, the inertial term is predicted to act out of phase with other loss terms.

Oh and Kopp's model is a considerable improvement over existing models because it accounts for inertial effect under unsteady conditions. However, their validation using wind tunnel measurements may be affected by Reynolds number effects, Richardson annulus effects, and other flow structures affected by scaling. The authors recommended that full-scale testing be conducted to validate such models, which will be pursued in this thesis study.

2.3.5   Interactions at Cavities and Openings

The reviewed models assume that cavities and orifice openings can be modelled as independent components with fully developed flow in between. However, flow from an orifice transitioning into a perpendicular cavity will have different flow structures (and losses) than flow through an orifice to an open space. Empirical data of loss coefficients

for flow configurations with transitions to perpendicular cavities are presented in this section drawn from publications for HVAC ductwork (ASHRAE 2001). Furthermore, some length of cavity is necessary for flow development within which friction losses differ from fully developed flow (Munson et. al. 1998). Such entrance lengths will also be reviewed in this section.

Loss coefficients for flow within a wide rectangular duct from an orifice to a cavity around a sharp 90° elbow for flow from an orifice with width, G, to a cavity with depth, H, can be estimated using the empirical equation (Straube 1995)

$$C_l = 0.866(H/G)^{0.85} \tag{49}$$

A similar equation with reversed H and G terms is used for flow from a cavity to an orifice.

Straube and Burnett (1995) used the 90° elbows along with entrance (C_l=0.5) and exit (C_l=1.0) loss coefficients in their ventilation model whose total values are plotted in Figure 10. The model was found to be relatively accurate by Basset and McNeil (2009) in their tracer gas measurements of brick cladding cavity ventilation driven by buoyancy (due to solar heating) and low wind exposure induced ventilation rates when averaged over a day. The loss coefficients are dependent on flow direction for cases where G and H are dissimilar.
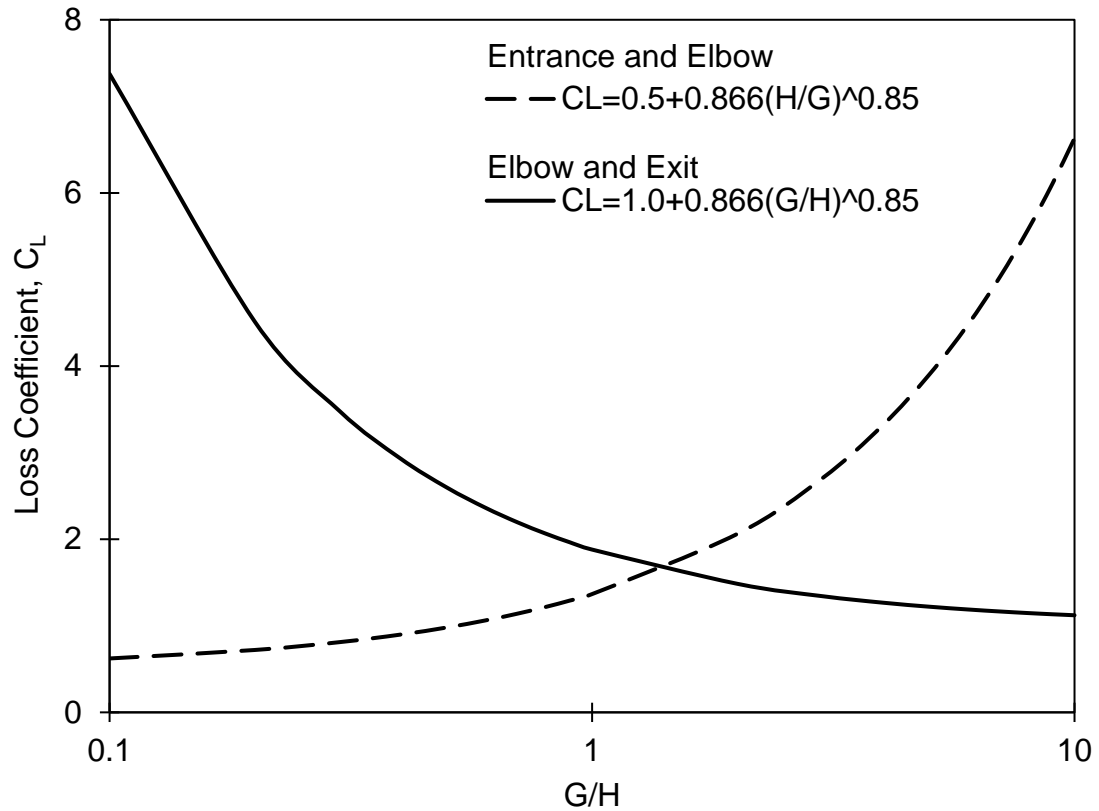
Figure 10: Plot of loss coefficients for flow either into a slot orifice and around a sharp 90° rectangular elbow or from a cavity through a sharp 90° rectangular elbow and out a slot orifice

Idelchik and Fried (1986) provided loss coefficient calculations for flow between a mid-span slot orifice and a perpendicular cavity or branch for merging flows (along with an exit coefficient) of

$$C_L = 1 + (G/H)^2 + 3(G/H)^2[(Q_c/Q_o)^2 + Q_c/Q_o] + 1 \tag{50}$$

and for diverging flows (along with an entrance coefficient)

$$C_L = 1 + k(Q_c/Q_o)^2(G/H)^2 + 0.5 \tag{51}$$

where Q_c is the branch or cavity flowrate along the branch of interest, Q_o is the flowrate through the orifice, and k is a constant equaling 0.3 for welded (smooth) connections.

Loss coefficients calculated from equations (48) and (49) are plotted for select orifice width to cavity depth ratios over a range of flow ratios between the two branches of the cavity in Figure 11.
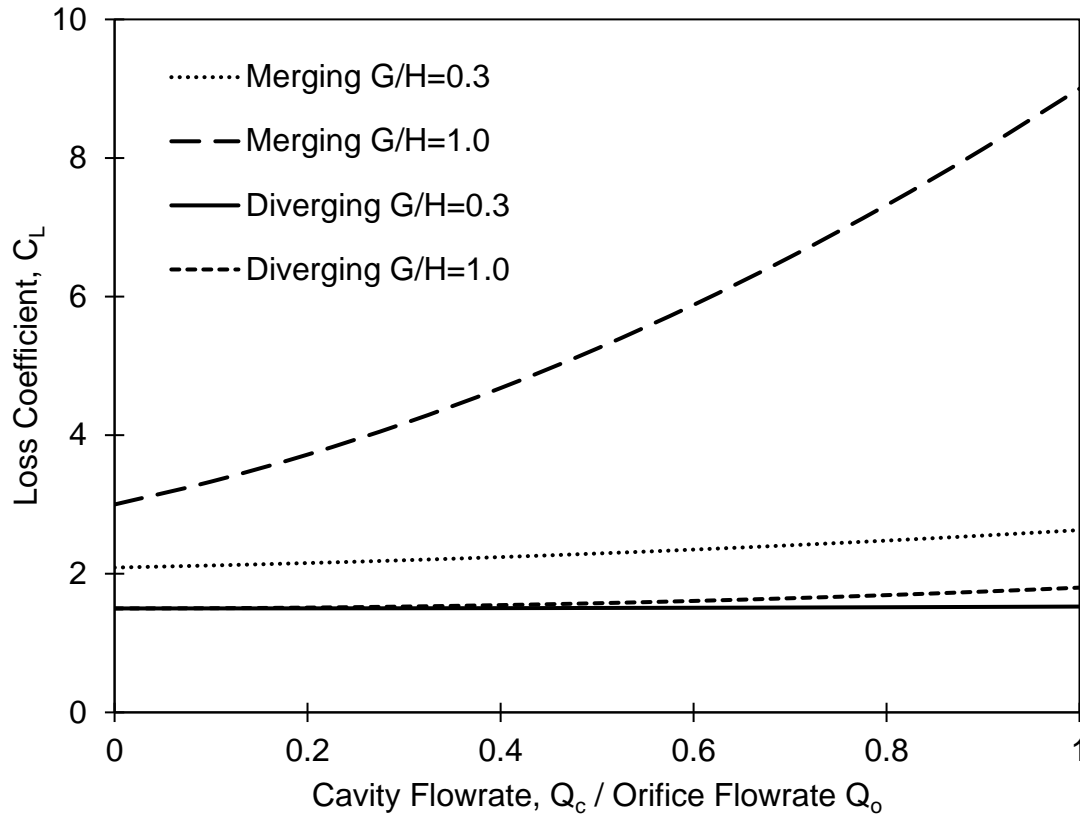
Figure 11: Plot of loss coefficients for diverging and merging tee with sharp 90 degree corners and entrance and exit losses

Loss coefficients for cavity flow to a sharp edged rectangular branch are given in ASHRAE 2001 Table 5.5. An exit loss coefficient of 0.5 has been added to the data provided in the table and plotted in Figure 13. Linear regression using method of least squares was used to fit the indicated equations to these data points. The plot shows that branch flow loss coefficients are greatest when the branch orifice width, G, is equal to or larger than the cavity depth, H, (higher G/H ratios) and when a smaller portion of the cavity flow exits along the branch.
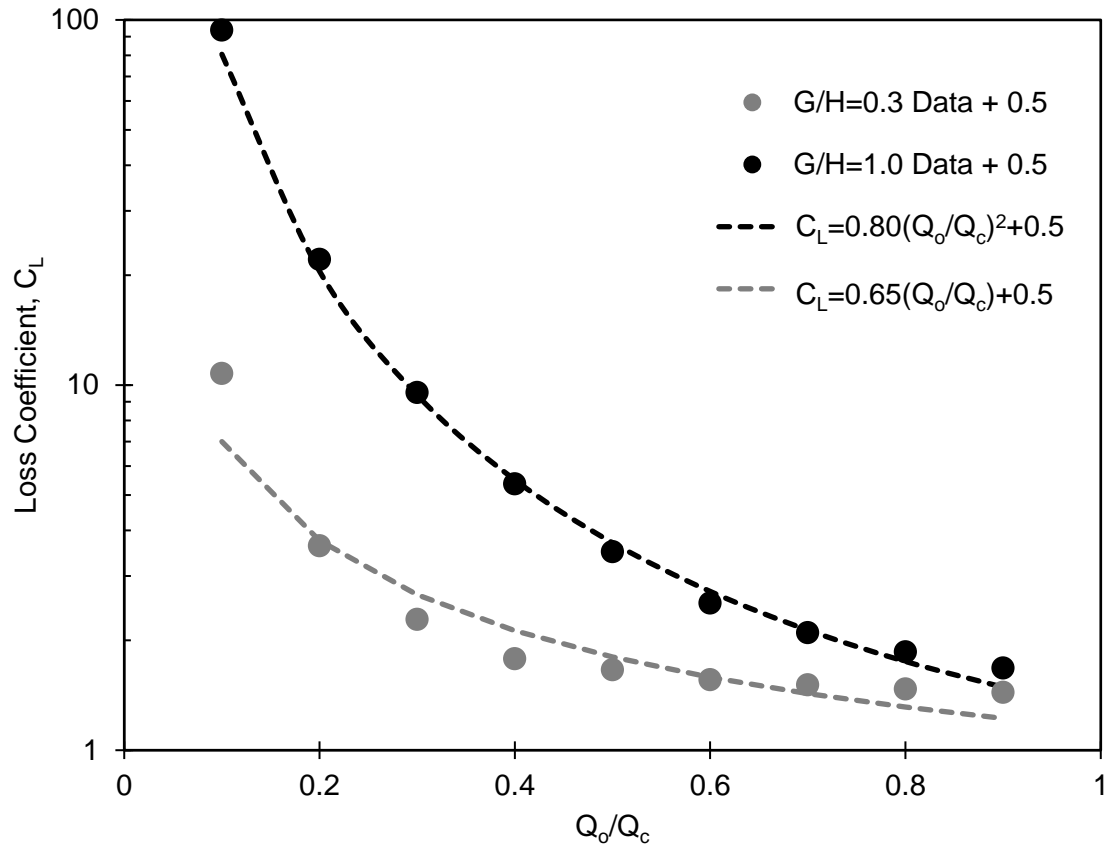
Figure 12: Plot of loss coefficients values for flow from a cavity into a branching orifice and an exit

Loss coefficients for cavity flow past a sharp edged rectangular branch is also given in ASHRAE 2001 Table 5.5 plotted in Figure 13. Linear regression using method of least squares was used to fit the indicated equations to these data points. The plot shows that branch flow loss coefficients are greatest when a larger of the cavity flow exits along the branch.
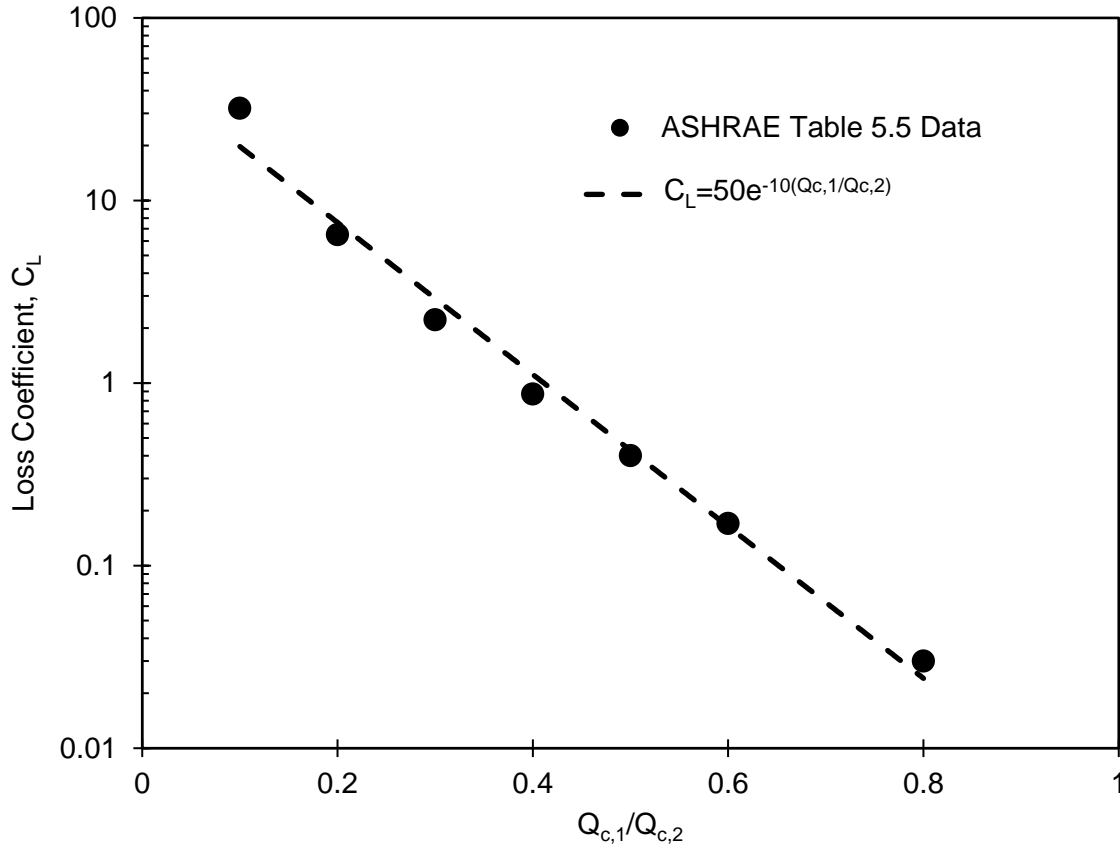
Figure 13: Plot of loss coefficients for cavity flow past a sharp edge orifice branch

The described losses differ from constant loss coefficients used in pressure equalization models. Furthermore, these losses may be greater for turbulent flow (in HVAC applications) than laminar flow (typical for cladding cavity flows), and this may explain why such losses have not had a pronounced effect in previous wind tunnel studies (where flow is forced laminar by scaling effects). This potential issue reinforced the need for full-scale experimental examination.

The length of cavity required for full flow development of the entrance length, L_e, can be calculated for laminar flow (Munson et al. 1998) as

$$L_e = 0.06 Re_{2H} \cdot 2H \tag{52}$$

and for turbulent flow as

$$L_e = 4.4 Re_{2H}^{1/6} \cdot 2H \tag{53}$$

These entrance lengths are plotted for select cavity depths over a range of Reynolds numbers in Figure 14. The entrance lengths for turbulent flows tend to be shorter than for laminar flows and that cavity depth has an impact. These lengths will be further discussed in context of flow through an idealized full-scale cladding system in Chapter 3.
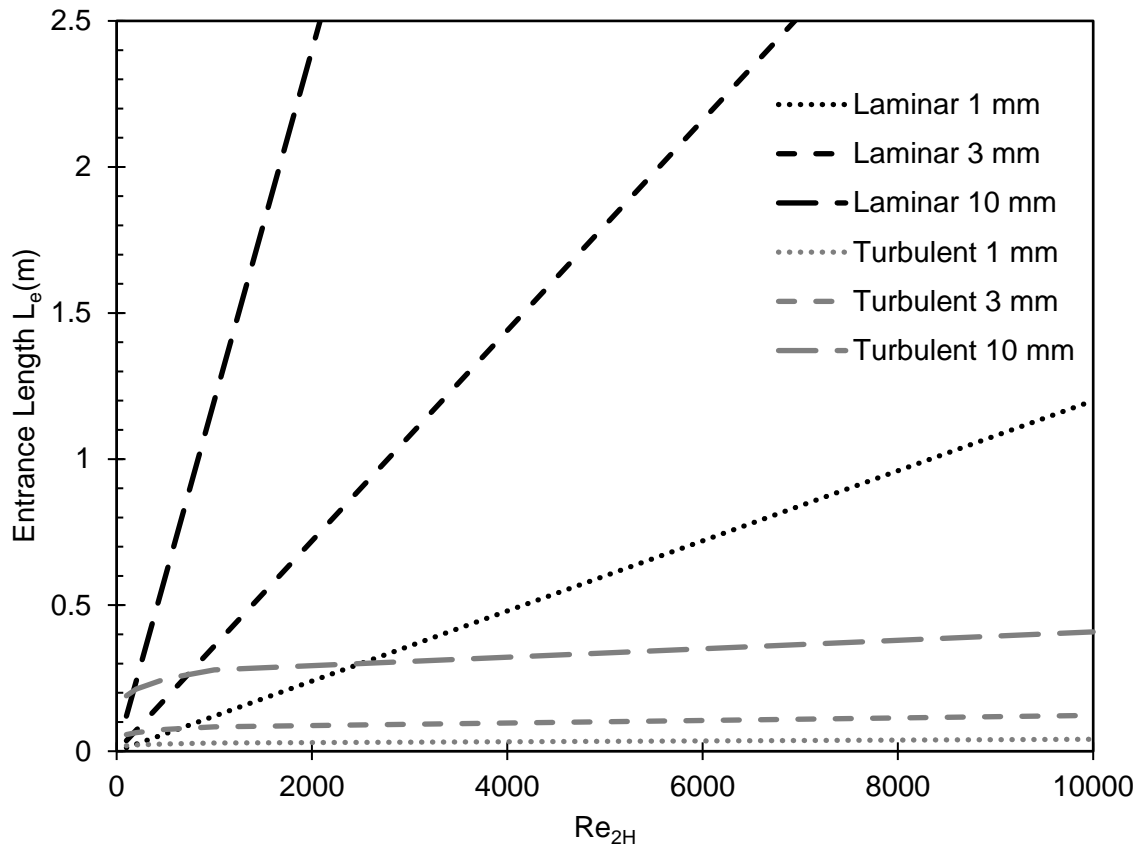
Figure 14: Plot of entrance length for select cavity depths for a range of Reynold numbers

2.3.6   Vinyl Siding Airflow Resistance

As vinyl siding is a focus of this these study, it is important to understand its air flow resistance characteristics. Vinyl siding has many openings which typically include vertical joints at least every 7.3m (12ft), horizontal joints every 0.2m (8in), and weep holes as shown in Figure 15. These openings are connected to common horizontal cavities created by the siding profile.
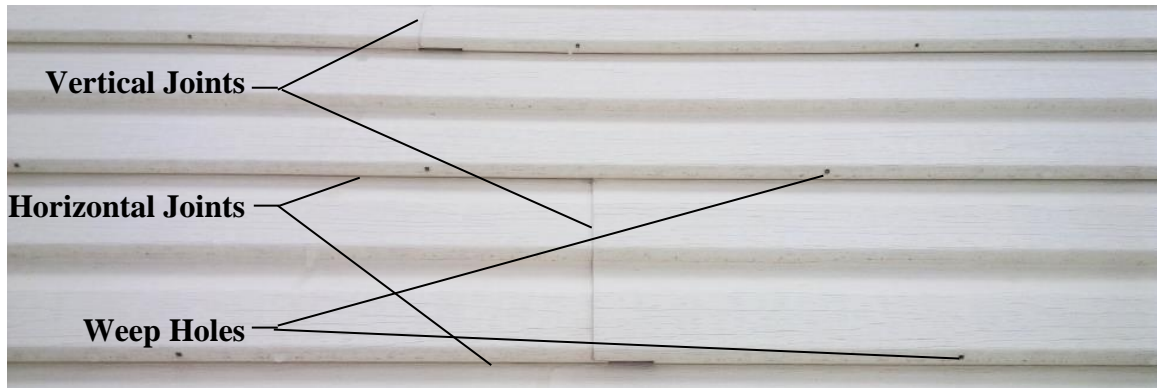
Figure 15 Photo of joints and holes in typical vinyl siding

Airflow resistance characteristics for vinyl siding have been previously measured (Van Straaten 2004) as part of a study of wall system drying (it was found that walls dry readily outward through vinyl siding due to the ventilation of the cavity underneath). The flow resistance for three flow paths were measured including out-of-plane flow through the vinyl siding (i.e., air permeability) of the siding and in-plane horizontal and vertical cavity flow as indicated in Figure 16. During the in-plane tests, the cladding was sealed and pressure across the face of the siding was varied from -100Pa to 100Pa to determine the influence of the siding being pulled away (suction) or pushed toward the sheathing underneath.
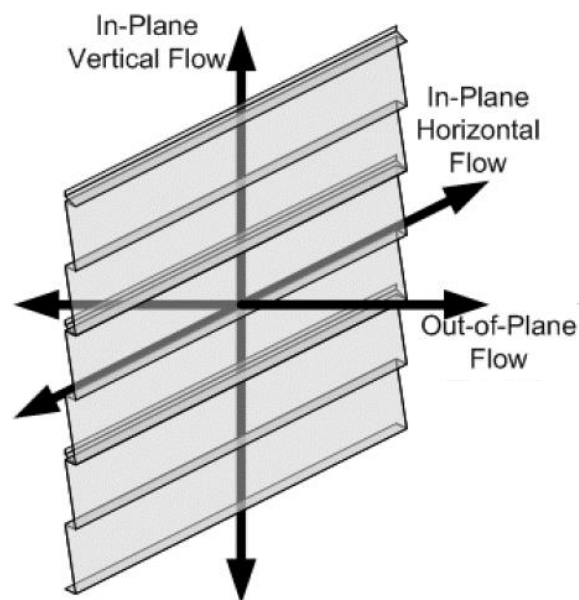
Figure 16: Flow path labelling for air flow resistance measurements

For in-plane flow the horizontal flow resistance was found similar to a 10mm rectangular cavity when under suction pressures (drawing the siding away from the sheathing). Under pressure (pushing the siding against the sheathing) the flow resistance was similar to a 5mm rectangular cavity. The vertical cavity flow resistance behind the siding was found to be equivalent to a 1 to 2mm rectangular cavity, which is so low because the vertical profile rests against the sheathing restricting airflow.

The measured flow resistance for flow through the siding face approximately fit the discharge equation as follows:

$$p_e - p_c = C_l \cdot 0.5\rho \left(\frac{Q}{OA}\right)^2 \tag{54}$$

where A is the area of cladding and Q is the measured flow. Van Straaten (2004) found that the measured relationships fit a loss coefficient, C_l, of 2.5 and open leakage area, O, of 0.12% for the range of tested pressures

2.3.7   Other Practical Limitations of Modelling

There are other wall system variables that may affect pressure equalization under high wind conditions, which are reviewed in this section.

System geometries have been assumed to have constant dimensions. However, wall system components may shift and/or flex during high wind load conditions. Deflections may have an additional unsteady flow resistance effect and separate inertial force effect on the system. Choi and Wang (1998) carried out a series of full-scale tests to study curtainwall spandrel panels, finding the flexibility of the aluminum back panels in these systems moderate the air pressure differential across the facing. Choi and Wang (1998) also found that the degree of flexibility of the back panel lowers the natural resonance frequency of the cavity pressure and can thus reduce the magnitude of resonance induced peak cavity pressures.

Some wall systems also incorporate loose membranes within the cavity. Kumar (2000) stated that the stiffness of the air barrier membrane is an important feature in achieving pressure equalization. Compared to the back panels studied by Choi and Wang (1998),

such loose laid membranes are much more flexible and may have similar or more drastic effects. Loose sheet materials may alternatively act like the plastic sheet used in standard wind load resistance testing (ASTM D 5206 2006) to transfer wind loads completely to the cladding.

Kumar (2000) suggested that the air tightness of the sheathing layer may also affect pressure equalization as it allows airflow out of the cavity like the additional openings in equation (22).

2.4 Closure

Previous work has shown that spatial variations in pressure on ventilated cladding significantly affect pressure equalization, identifying a need to modify the current ASTM D5206 testing. More sophisticated testing, supplemented by models, appears necessary to accurately capture pressure equalization of cladding systems.

The objective of the research in this thesis is to determine if modifications are needed to the multiple discharge equation analytical model to account for effects not seen in scaled wind tunnel testing. From the review of previous research, the potential issues are as follows:

- Viscous losses may be significantly different for wide cavities and orifices due to Reynolds number effects.
- The MDE model assumes fully developed laminar flow through the cavity, which may not hold in full scale assemblies where cavity Reynolds numbers are larger.
- Richardson annulus effects are affected by scaling such that they would be negligible for scaled conditions and pronounced under full-scale conditions.
- Losses for flow around geometries, such as elbow and tee intersections, are not captured in the MDE model but such effects may be significant in full-scale.

If such models are going to be used to inform pressure equalization allowances, such as that in ASTM D3679, it will be important to verify the model is accurate in full-scale.

Chapter 3

3 Simplified Full-Scale Cladding System Measurements

Chapter 1 introduced the concept of pressure equalization and its importance to wind loading on wall cladding. A review of pressure equalization laboratory measurements and analytical models were presented in Chapter 2 revealing that the basis for allowance in ASTM D3679 is questionable because it doesn't capture the effects of spatial pressure variances. The use of the MDE model is shown to be a potentially suitable method to predict such effects including spatial variation. However, the model has not been verified with full-scale testing.

This chapter presents full-scale laboratory measurements of an idealized cladding system intended to evaluate of specific analytical model components to determine necessary modifications to address the unknowns identified in Chapter 2. Specifically, discharge loss, friction loss, and inertial terms for the orifice and cavity are evaluated. These terms are evaluated in full-scale on assemblies with varying geometries and exposure to both steady and unsteady pressures.

The first section of this chapter describes the test approach. In the next section test results are presented and compared with predictions from the MDE model. Conclusions and modelling recommendations are given in the final section along with recommendations for further research.

3.1 Test Approach

A test rig was constructed to subject a full-scale ventilated cladding system to temporally and spatially varying surface pressures. The test rig's flow system included several simplifications relative to cladding systems used on buildings. A sketch of a simple ventilated cladding system including adopted nomenclature was given in Figure 4 and is repeated in Figure 17 with identified simplifications for this idealized cladding relative to real wall systems. The simplified align with the MDE model assumptions.
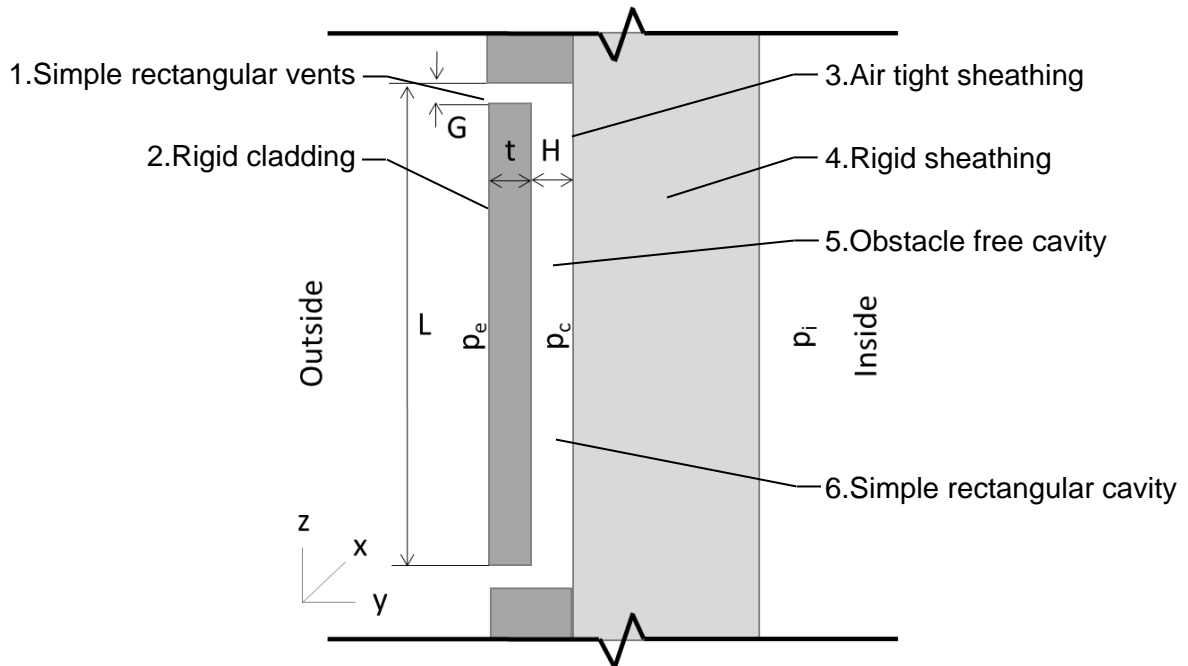
Figure 17: Wall cladding schematic with dimension nomenclature

The idealized cladding system simplifications include the following:

1. Simple rectangular vents: The vents are slots (i.e. W>>G). When measuring along the middle of the slot width, this allows the influence of the slot ends to be ignored and the system modelled as a simple network. Having constant vent dimensions further simplify the model dimensions.

2. Rigid cladding: along with the rigid sheathing, this allows the system to be modelled with a constant cavity depth, H, and unsteady effects related to the movement of the cavity wall to be assumed negligible.

3. Air tight sheathing layer: This allows flow through wall sheathing to the inside of a building to be ignored.

4. Rigid sheathing: along with the rigid cladding, this allows the system to be modelled with a constant cavity depth, H, and unsteady effects related to the movement of the sheathing wall to be assumed negligible.

5. Obstacle free cavity: this allows potential contribution of obstacles to flow resistance and resulting development of flow structures to be ignored.

6. Simple rectangular cavity: this allows the flow to be modelled as flow between parallel plates which has been well studied (see Section 2.2.3). Having constant dimensions along the cavity length and height simplify the modelling of wall friction losses and air volume used in the model's inertial components.

The study test scenarios are listed in Table 1. These test setups, along with their report sections, are listed the table for reader guidance.

Measurements are taken under steady and unsteady pressures to capture the relative impact of the inertial terms and determine if loss terms are affected by unsteady flows. A range of steady pressures from 0.3 kPa to 2 kPa was used because a) they were high enough to minimize uncertainty (+/- 16 Pa uncertainty is +/-5% of 0.3 kPa) and b) they captured the peak surface pressures measured in vinyl siding testing by Cope et. al. (2012) of around 1 kPa. A sinusoidal frequency of 5Hz was a) the highest that could be generated for 1 kPa amplitudes within the airboxes with the number of PLAs that could accommodated within the laboratory test rig and b) was the high end of high wind induced loading frequencies used in testing of low-slope roofing systems which include similar suction loading within separation bubbles which define design conditions (Baskaran 2002).

Table 1: Test Scenarios for Simplified Cladding System Study

Chapter Section	Pressure	Config	Orifice Width, G	Orifice Length, l	Cavity Depth, H	Cavity Length, L	Flowrate
3.2.1	0.3 kPa 0.5 kPa	End Slot	2.44mm	6.45mm	2.58mm	604mm	Measured
				160mm	2.58mm		
3.2.2	1 kPa			160mm	9.46mm		
3.2.3	1.5 kPa 2 kPa Steady	Slot Inter-mediate		6.45mm	2.58mm		
				160mm	2.58mm		
3.2.4				160mm	9.46mm		
3.3.1	1 kPa 5 Hz Sinusoid	End Slot		160mm	2.58mm		Not Measured
3.3.2				160mm	9.46mm		
3.3.3		Slot Inter-mediate		160mm	2.58mm		
3.3.4				160mm	9.46mm		

The steady and sinusoidal pressures are applied to each slot independently to capture both end and intermediate slot conditions. These conditions are tested for two separate slots to assess measurement repeatability. The cladding system can be set up with two slot lengths, l, and two cavity depths, H. The orifice width, G, and cavity length between orifice, L, are fixed. The tests include pressurization and depressurization to capture the impact of flow direction (such as merging and diverging flows) on loss coefficients.

Previous studies of pressure equalization have shown a dependence on the ratio of vent orifice to cavity flow resistance (simplified to G/H ratio). Furthermore, the effect of scaling of turbulence within the cavity is a potential issue with previous wind tunnel tests. For this study, cavity depths, H, of 2.58mm and 9.46mm were selected because they are within the range of those behind full scale cladding systems and resulted in one condition with minimal cavity pressure gradient and one with high cavity pressure gradient along its lengths. The ratio of orifice to cavity flow resistance termed, φ, by Oh and Kopp (2014) can be approximated based on equations (5), (37), and (39) as

$$\varphi = \frac{C_l \cdot 0.5\rho v^2}{96/Re \cdot 0.5\rho(v\frac{G}{H})^2 \cdot L/2H} = \frac{C_l\rho vH^2}{24\mu L} = \frac{2.5 \cdot 1.2 \cdot vH^2}{24 \cdot 0.000018 \cdot 0.604} = 11500vH^2 \qquad (55)$$

where C_l is the loss coefficient for which a value of 2.5 was used by Oh and Kopp (2014) as discussed in Chapter 2, ρ is the density of air of 1.2 kg/m^3, μ is the dynamic viscosity of air of 1.8 E-5 Pa s, L is the cavity length of 0.6m (discussed later in this chapter), u is the cavity air velocity which is expected to be on the order of 1 to 10 m/s based on published field measurements (Gulum 2003).

For a range of cavity velocities from 1 to 10 m/s the 9.46mm cavity is expected to have $\varphi = 1.2$ to 11.5 and for 2.58mm cavity$\varphi = 0.1$ to 1.0. Hence, the vent orifice pressure drop is expected to be higher than the cavity pressure drop for the 9.46mm cavity resulting in minimal cavity pressure gradient and similar or greater than the orifice pressure loss for the 2.58mm cavity and a high cavity pressure gradient.

Details for the 2.58mm and 9.46mm cavity depth test setups are given in Figure 20 and Figure 19. These are shown for an end slot configuration (Airbox#1 pressurization).

The cladding was constructed of a 1.2 x 2.4m (4 x 8ft) aluminum plate with slot orifices cut for each of the four airboxes, as shown in a photo in Figure 18. The thickness of the aluminum plate set the 6.45mm slot length. This was thick enough to ensure sufficient plate stiffness for the rigidity assumption (measured deflections are included in the uncertainty analysis in Appendix 1). However, this minimum slot length was short enough so that the wall friction of the orifice was negligible relative to discharge losses effectively forming a sharp-edged orifice. The 2.44mm (overall mean) slot width, G, was the narrowest cut that could be made by a local laser cutting company through the aluminum sheet. The height of these slots set the maximum cavity width, W, of 500mm.

Figure 18: Photo of laser cut orifice slot in test aluminum "cladding" sheet
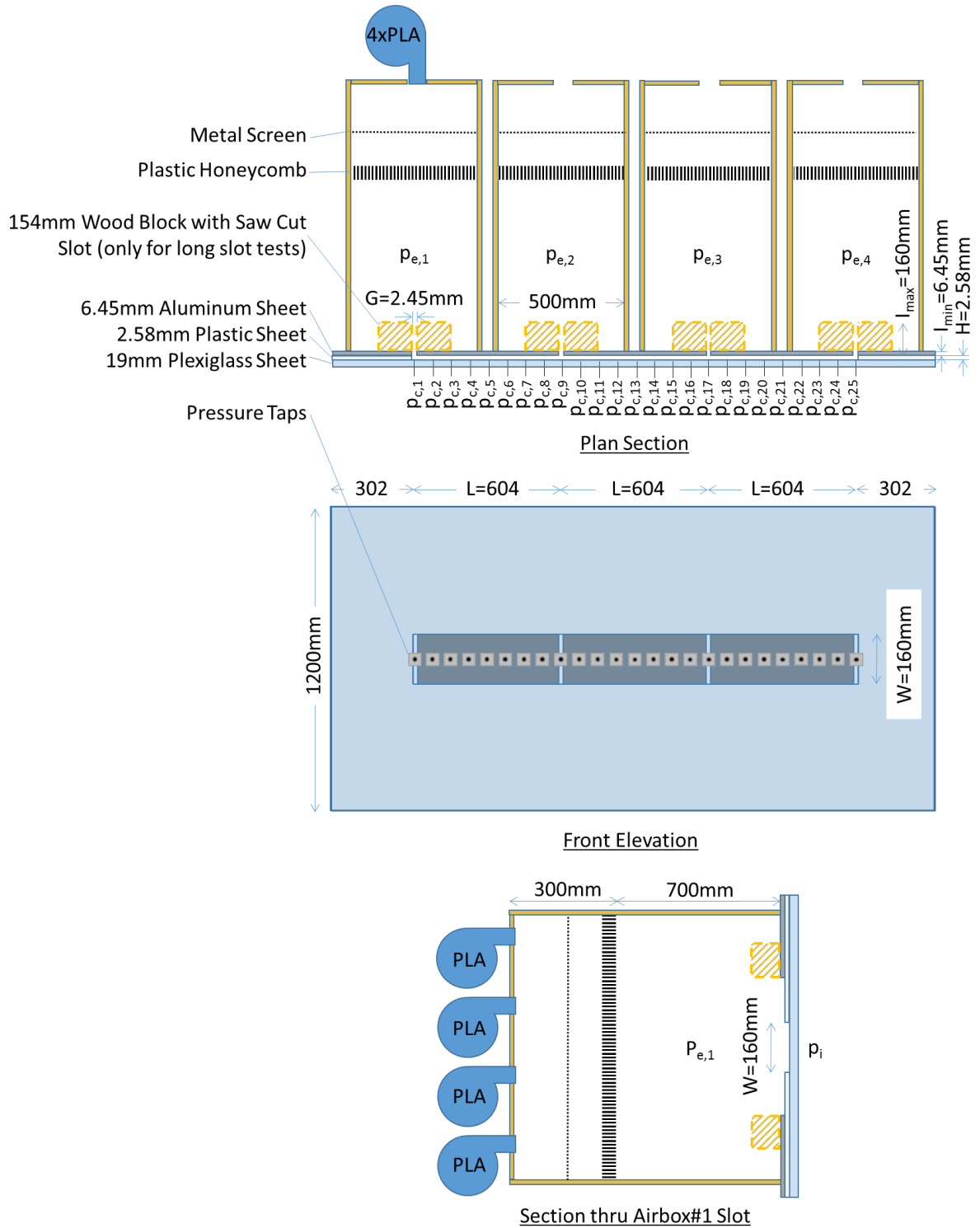
Figure 19: Airbox design and labelling for 2.58mm deep slot setup and 6.45 or 160mm orifice lengths (pressurization of Airbox#1 shown)

Figure 20: Airbox design and labelling for deep 9.48mm slot setup and 6.45 or 160mm orifice lengths (pressurization of Airbox#1 shown)

The cavity depths were set by the thickness of plastic spacer sheets with measured thicknesses 2.58mm and 9.42mm setting the cavity depth, H. For the 9.42mm cavity width, W, was 500mm resulting in a high width to depth ratio (greater than 50), as detailed in Figure 20. For this cavity depth scenario, spacers (streamlined to minimize generation of turbulence) were included within the cavity (shown in the photo in Figure 22) to accurately set the cavity depth and minimize deflections. The spacers were 12.5mm wide at their widest part, which resulted in a maximum 5% blockage of cross sectional area. The 2.58mm cavity depth setup is detailed in Figure 19. The width of the cavity was reduced to 150mm limiting deflections without use of the spacers (see photo in Figure 21) while maintaining a high width to depth ratio (greater than 50).

The cavity interior (opposite the aluminum sheet) was enclosed by a ¾" thick acrylic sheet. The sheet was clear, allowing visual inspection of the cavity. The thickness was adequate to minimize deflections maintaining the rigid sheathing assumption. The plastic sheet which sets the cavity depth, is air-sealed to the aluminum and clear acrylic sheets with silicone caulking. This can be seen compressed around the edges of the cavity in the photo in Figure 21.

Airboxes are mounted to the aluminum sheets and generate varying pressures at each of the four slot orifices. The interior of the air boxes was 500mm wide and 1m high. Four of them were mounted side-by-side along the 2.4m length of sheet. The slots were positioned along the centre of airboxes. The airboxes were further designed to limit eddies entrained within the airflow approaching the slot. To achieve this condition, the airboxes had screens to make the airflow spatially uniform across the cross-sectional area of the airbox interior followed by a honeycomb grid to remove entrained eddies. There is a 500mm space between the honeycomb and the slot openings to allow flow development in front of slot orifices. The airboxes were pressurized using Pressure Load Actuators (PLAs). It was found that a 5 Hz pressure signal with a 1000 Pa amplitude could be generated by connecting four PLAs to each airbox. A 5 Hz pressure fluctuation it at the high limit of wind fluctuations (as described in Chapter 2) and should be high enough to capture surface pressure fluctuation as described by Kopp et. al. (2010) in the design of the PLA system.
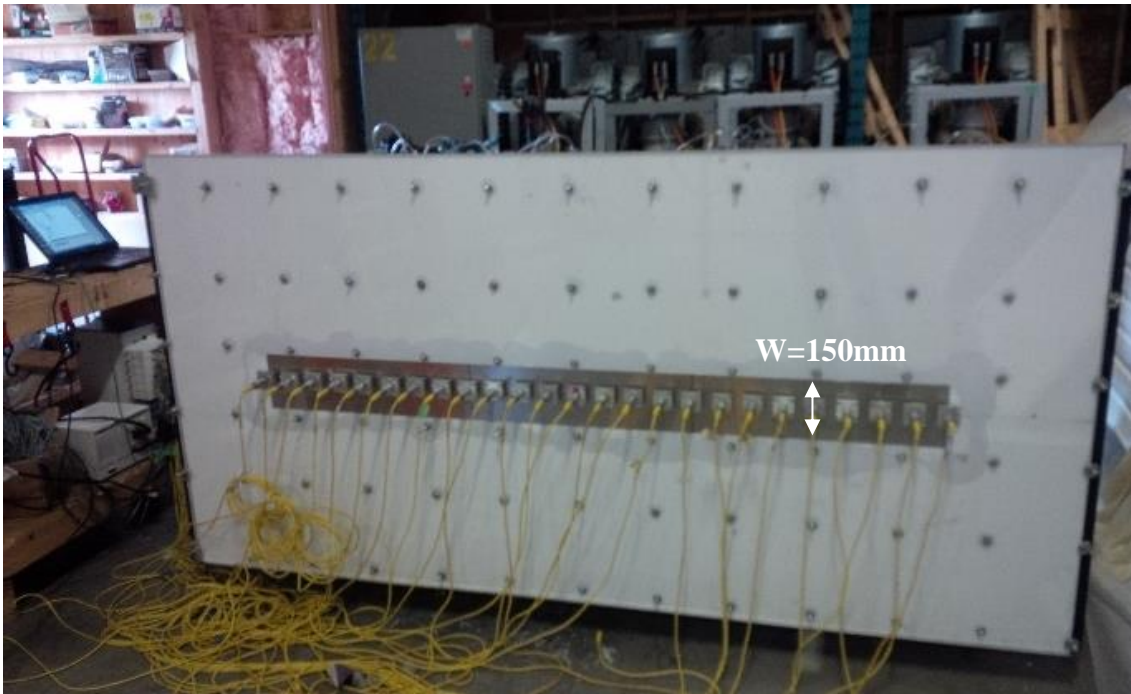
Figure 21: Photo of test setup for 2.58mm deep cavity
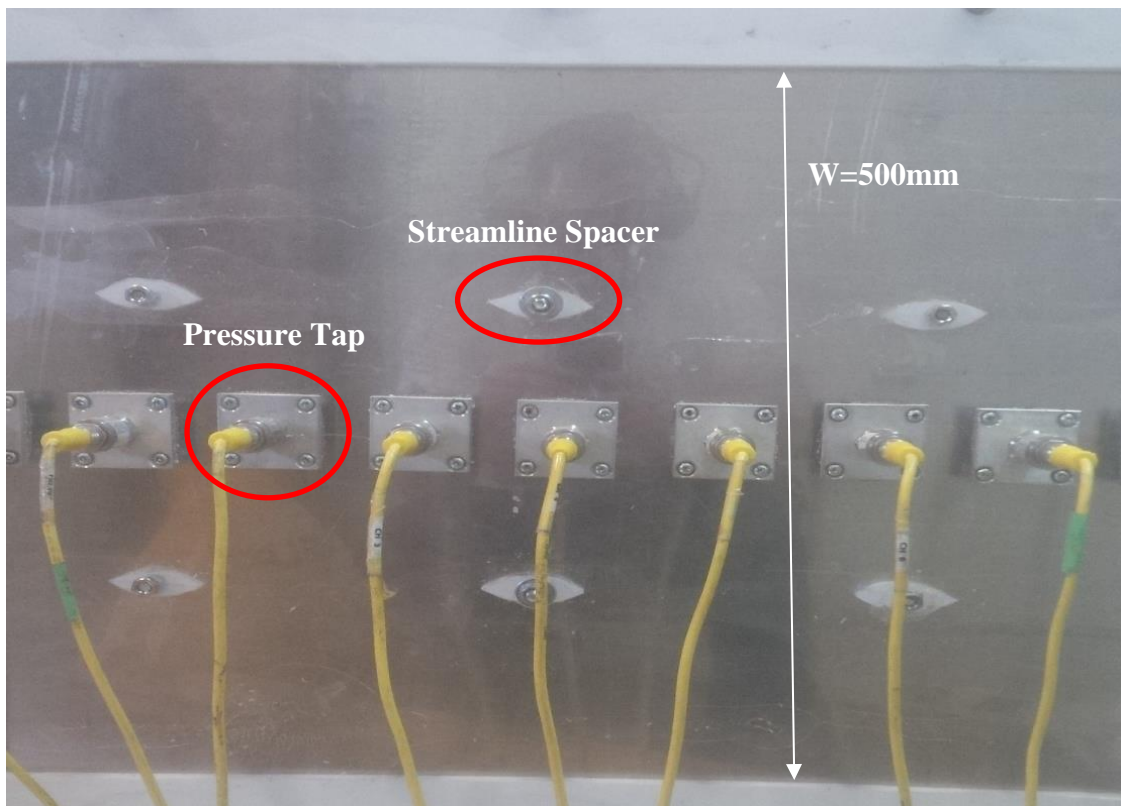
Figure 22: Photo of streamline spacers for 9.42mm deep cavity

The airflow rate between the PLA and airbox was measured for steady flow tests by a Merriam 50MC Series Laminar Flow Element (LFE). A 2m length of 150mm diameter pipe was installed before and after the LFE to avoid flow disturbances (as recommended by the manufacturer). The flow rate through the LFE was determined by measuring the pressure drop across it's honeycomb core using a Dwyer Series 250-AF inclined manometer.   Airflow rate could only be measured for steady flow scenarios because of response time limitations.

The airbox pressures were measured for steady flow scenarios using a simple U-tube water filled manometers and wall-mounted pressure transducers for unsteady conditions. The cavity pressures were measured by pressure transducers spaced 76mm on centre providing seven equally spaced pressure taps along the cavity between slot openings. This results in a total of 25 cavity pressure taps, as indicated in Figure 20 and Figure 22. This is a similar spacing to that used in Oh and Kopp's (2014) wind tunnel measurements (when brought to full scale). The cavity pressure transducers were mounted in 6mm (¼") FPT threaded holes in an aluminum plate mounted over the acrylic sheet. The acrylic sheet had 1.6mm (1/16") holes drilled to reach from these holes to the cavity. It is assumed that these holes were small enough to not affect the airflow. The volume of the holes resulting in a tap volume of 0.1 to 1% of the cavity air volume between adjacent taps for the range of cavity dimensions which is assumed to have a negligible effect on measurements and air flow.

For unsteady flows, the measurements from the cavity and airbox pressure transducers were recorded by a data acquisition system at a rate of 1000 Hz. The dataset was filtered using a low pass Butterworth filter at 100 Hz prior to analysis to remove electrical noise. The results of these measurements and comparisons to the MDE analytical model will be discussed in the next section.

An illustration of the anticipated flow through a short 6.45mm orifice and shallow 2.58 mm cavity is illustrated in Figure 23 for pressurization of end orifices (Airbox#1 or Airbox#4) on the left and intermediate orifices (Airbox#2 or Airbox#3) on the right. During pressurization air blown into the cavity separates at the inside corner of sharp

corners. An eddy is also expected to form in the "dead" space of the outer corner through the elbow. During depressurization shown in Figure 24, air is flowing in the opposite direction and the inside corner separation bubble would form in the orifice in lieu of the cavity. An eddy is once again anticipated at the outside corner. Similar illustrations for the long 160mm slot orifice are shown for pressurization and depressurization in Figure 25 and Figure 26. The anticipated flow structures would be like those occurring for the short orifice except there would be a greater length for flow development in the orifice segment. Finally, illustrations are shown for the long 160mm slot orifice and a deep 9.46mm cavity are shown in Figure 27 and Figure 28. The flow structures would be like those occurring for the shallow cavity except the dead space at the outside corner of the elbow is expected to be larger. The separation bubble forming during pressurization at the inside corner is less confined by air flowing in the cavity and may be larger thus. For depressurization, the airflow from cavity airflow into the orifice is less restrained and can more easily flow around the corner resulting in a smaller separation bubble in the orifice.
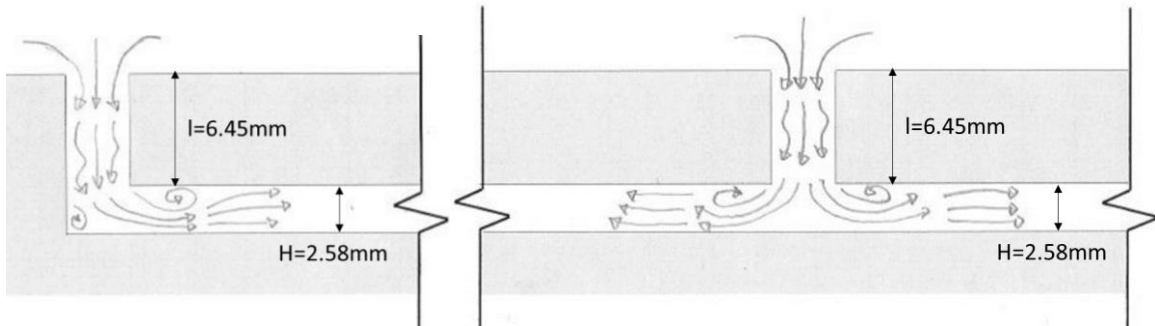
Figure 23: Expected flow structures for pressurization of an end airbox (left) and an intermediate airbox (right) for l=6.45mm, H=2.58mm geometry
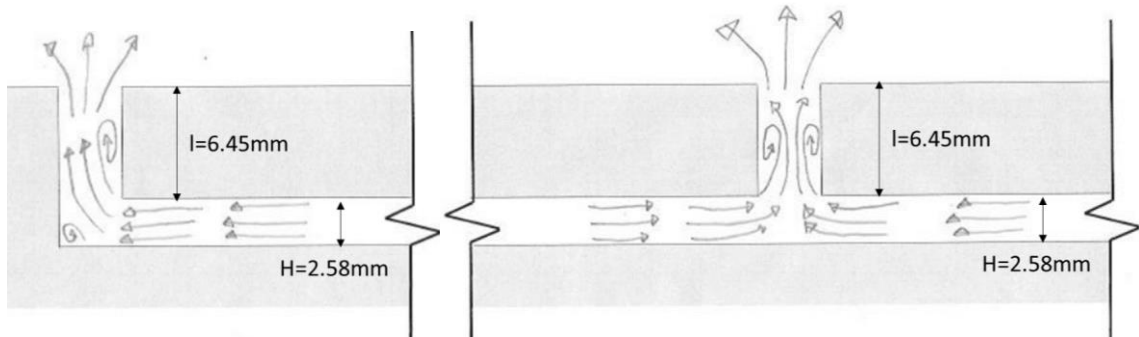
Figure 24: Expected flow structures for depressurization of an end airbox (left) and an intermediate airbox (right) for l=6.45mm, H=2.58mm geometry
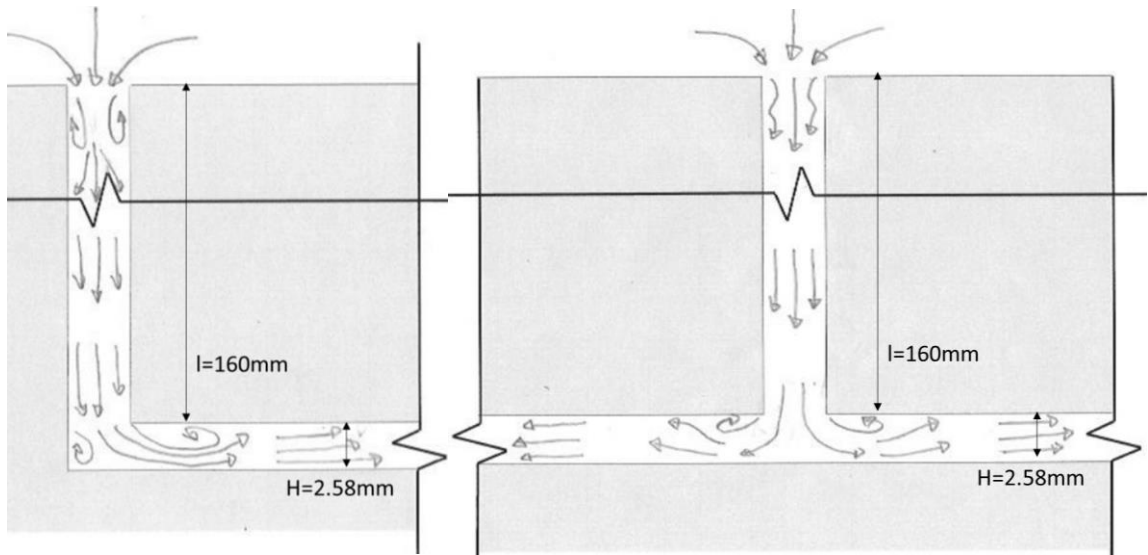
Figure 25: Expected flow structures for pressurization of an end airbox (left) and an intermediate airbox (right) for l=160mm, H=2.58mm geometry
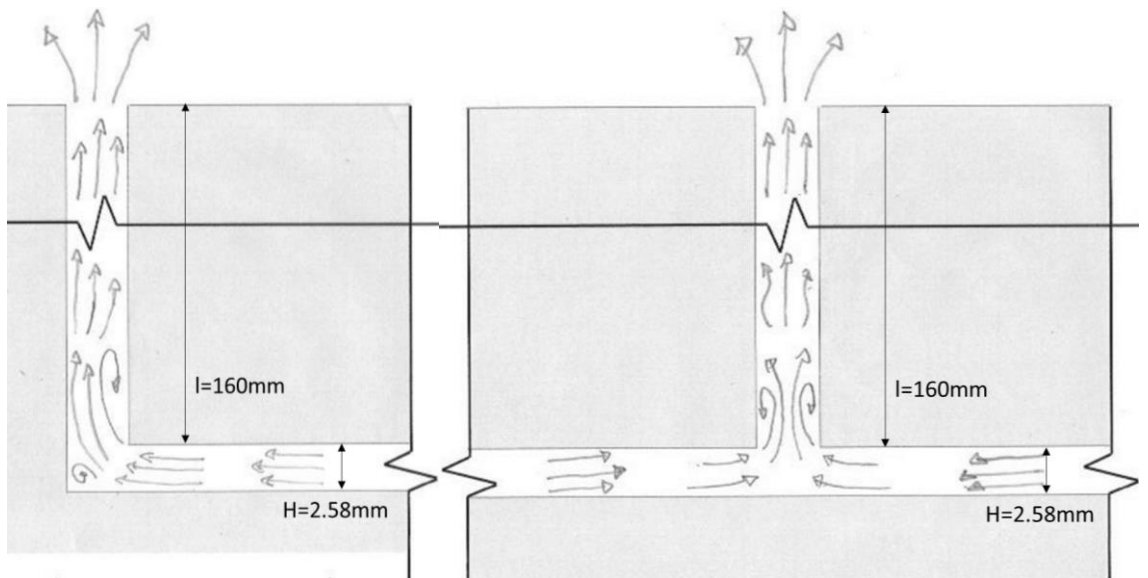
Figure 26: Expected flow structures for pressurization of an end airbox (left) and an intermediate airbox (right) for l=160mm, H=2.58mm geometry
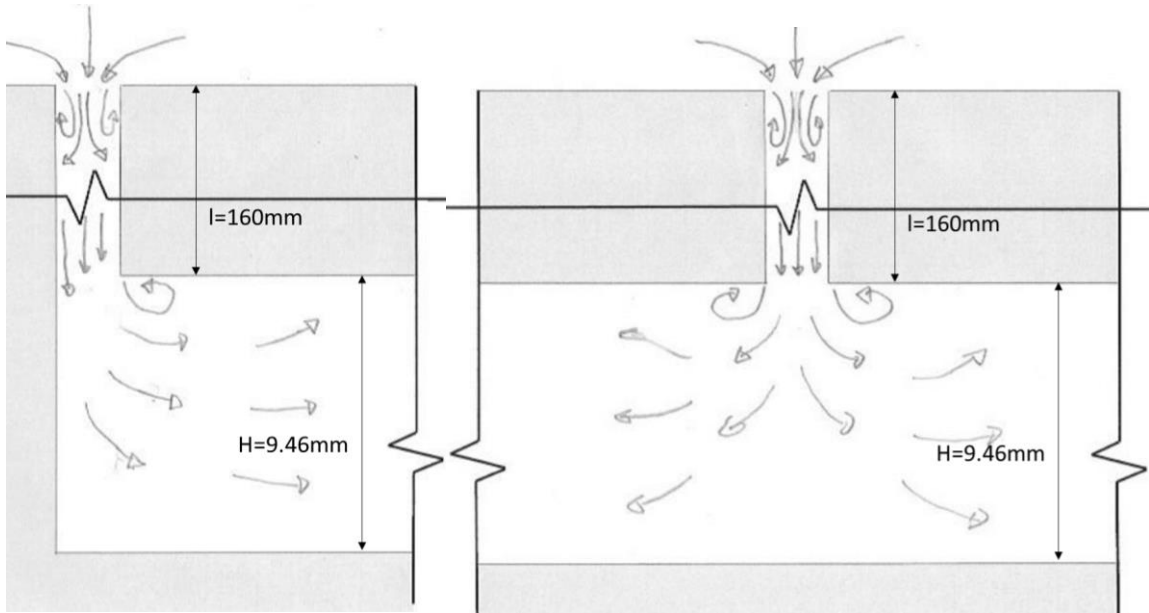
Figure 27: Expected flow structures for pressurization of an end airbox (left) and an intermediate airbox (right) for l=160mm, H=9.46mm geometry
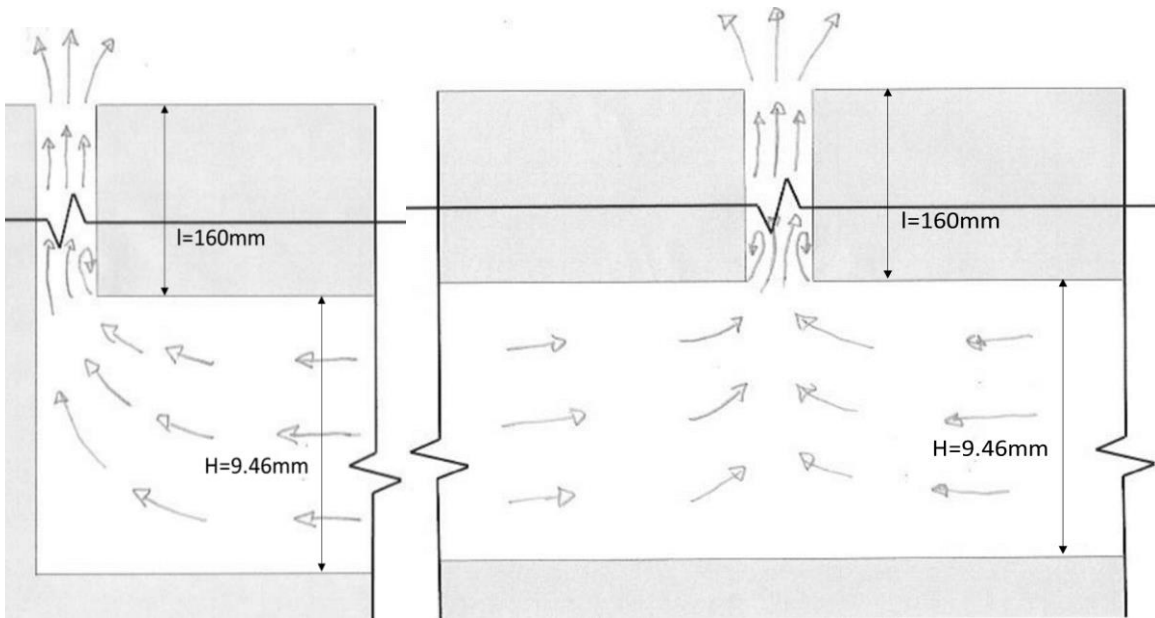
Figure 28: Expected flow structures for depressurization of an end airbox (left) and an intermediate airbox (right) for l=160mm, H=9.46mm geometry

3.2   Steady Flow Results

The airboxes are pressurized using PLAs to provide steady state pressures at the individual orifices. Results are presented for orifice flow through both orifices at the end of the cavity (forming an elbow) and intermediate orifices (forming a tee intersection). The sections are further divided for the shallow and deep cavity geometries. These sections further include comparisons to analytical model components for these various setups.

3.2.1   Steady Flow Results for End of a Shallow Cavity

Flow schematics and measurement labels are shown in Figure 29 and Figure 30. In Figure 29, Airbox#1 is pressurized and Airbox#4 is pressurized in Figure 30. The remaining airboxes are left open to the lab environment. The resultant airflow directions for airbox pressurization are indicated in the illustrations: the opposite flow directions would occur for depressurization.
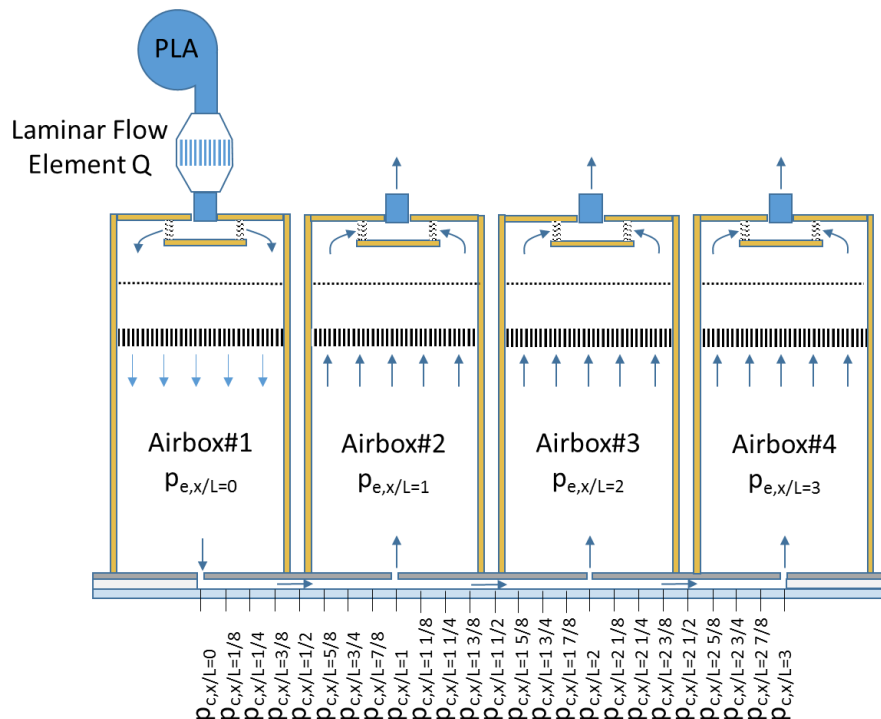
Figure 29: Flow schematic for steady pressurization of Airbox#1
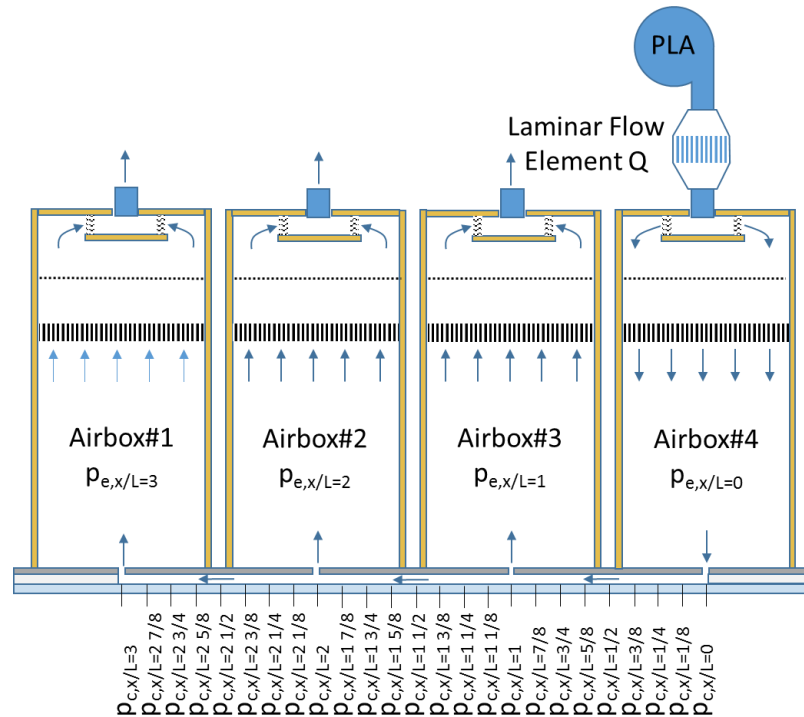
Figure 30: Flow schematic for steady pressurization of Airbox#4

Measurements of cavity pressures for steady 1kPa pressurization of Airbox#1 for the shallow 2.58mm cavity and short 6.45mm slot orifice are plotted in Figure 31. To allow positive and negative pressurization results to be directly compared cavity pressure measurements were converted into non-dimensional terms by dividing by the pressure in the pressurized airbox. Dividing by the airbox pressurization further allowed comparison between experiments with small variations in airbox pressurization. Linear curve fits of the measured data are also shown. These curve fits are based on mid-cavity pressure measurements ($x/L = \frac{1}{4}$ to $x/L = \frac{3}{4}$) excluding measurements close to the orifice to avoid being influenced by flow structure at orifice to cavity interfaces. Projections of these curve fits are also shown as dashed lines to approximate the complete cavity length pressure gradients extending all the way to the orifice slots.
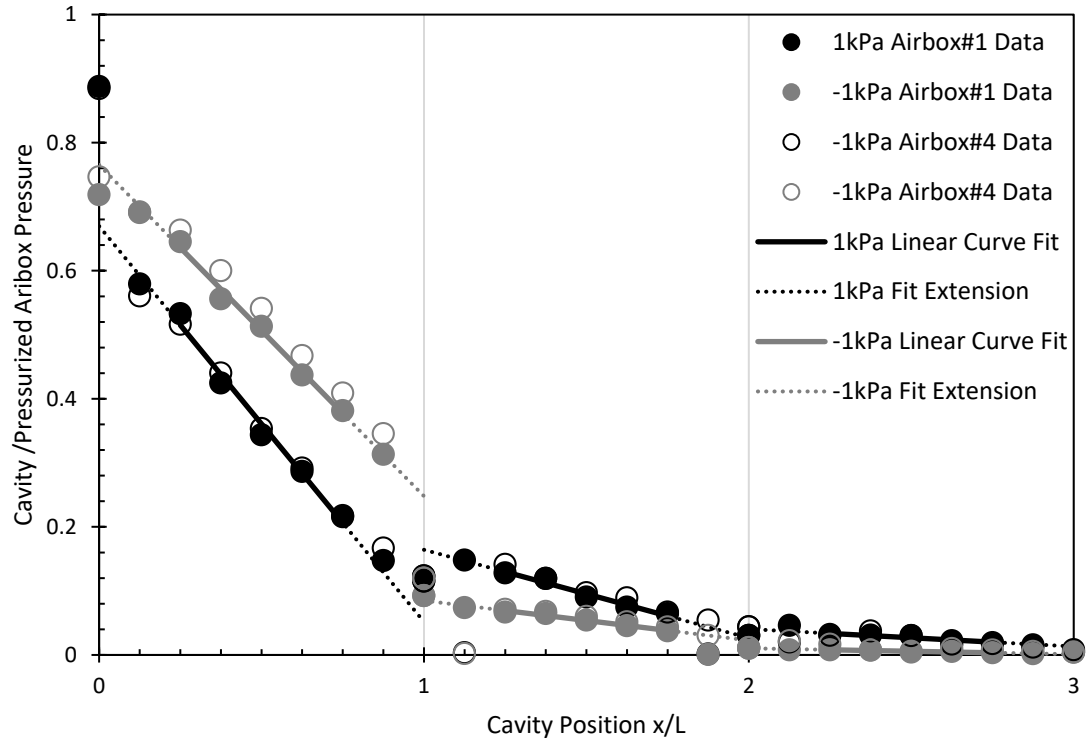
Figure 31: Measured cavity pressures for steady -1kPa pressurization of Airbox#1 (and Airbox#4) l=6.45mm, H=2.58mm, and G=2.44mm geometry with linear gradients shown

The measurements for Airbox#1 and Airbox#4 pressurization and depressurization are also shown in Figure 31 revealing similar results and, hence, good experimental repeatability for this setup. A decreasing pressure gradient is seen between x/L=0 and the x/L=1. A slight cavity gradient can also be seen between the slot orifice opening at x/L=1 and x/L=2. This gradient is due to cavity airflow resistance and is reduced at the orifice at x/L=1 because a portion of the airflow is exiting the cavity at that location. The pressures and pressure gradient is quite low between x/L=2 and x/L=3. This is because once again a portion of the flow is exiting at the orifice at x/L=2 and the airflow through this portion of the cavity is quite low.

Results for the long 160mm slot orifice are plotted in Figure 32. The results are similar as for the short 6.45mm orifice case, except that the y-axis intercepts are slightly lower.
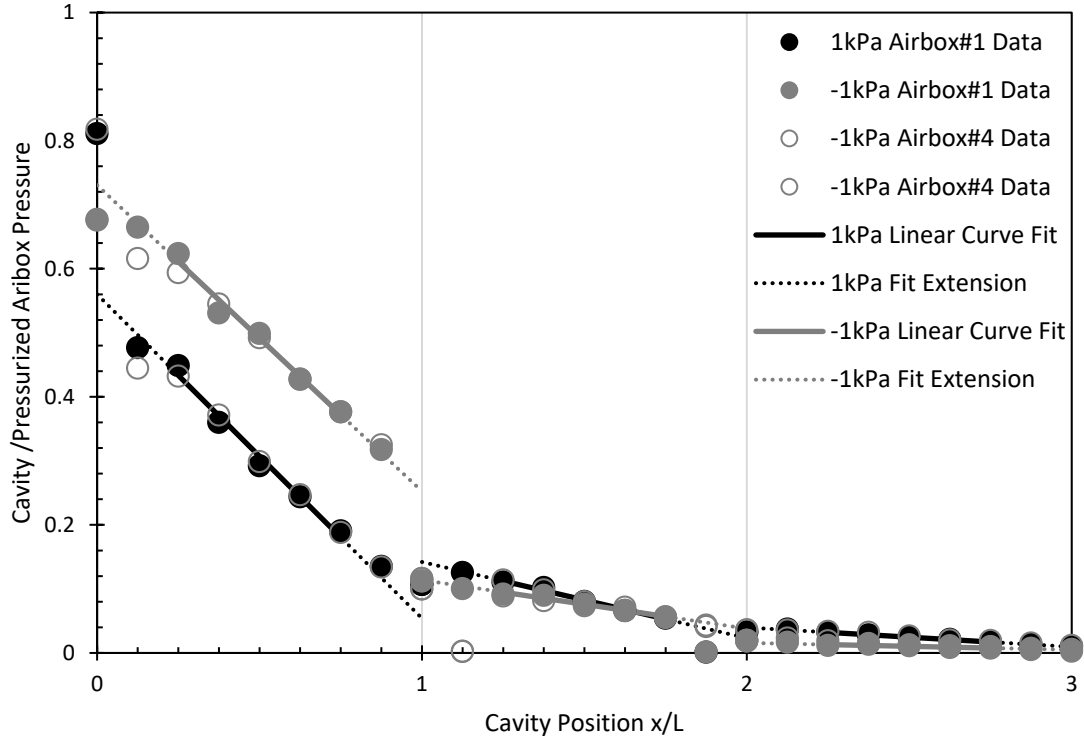
Figure 32: Measured cavity pressures for steady pressurization of Airbox#1 (and Airbox#4) l=160mm, H=2.58mm, G=2.44mm geometry with linear gradients shown

Assuming laminar flow in the cavity (see equation (32)) the portion of the airflow exiting at x/L=1 can be estimated as follows:

$$Q_2/Q_1 = (p_{x/L=0.25} - p_{x/L=0.75})/(p_{x/L=1.25} - p_{x/L=1.75}) \qquad (56)$$

Based on the pressure gradients shown in Figure 31 and Figure 32 about 80% and 90% of the airflow exits at the x/L=1 orifice for the pressurization and depressurization cases, respectively.

The pressure loss across the orifice at the pressurized airbox, $[p_{e,x/L=0} - p_{c,x/L=0}]$, for pressurization and depressurization were estimated based on the difference between the airbox pressure and these y-axis intercepts. Measured orifice loss coefficients were then determined as

$$C_l = [p_{e,x/L=0} - p_{c,x/L=0}]\Big/\Big[0.5\rho\left(\frac{Q}{GW}\right)^2\Big] \qquad (57)$$

The measured orifice loss coefficients are plotted along with predicted orifice loss coefficients below relative to Reynolds numbers calculated from measured flowrates using equation (9) in Figure 33.

Sharp Edged Orifice

$$C_l = 2.5 + \left[\frac{48\mu lQ}{(2G)^2 GW}\right]\Big/\left[0.5\rho\left(\frac{Q}{GW}\right)^2\right] \tag{58}$$

Entrance and Elbow

$$C_l = 0.5 + 0.886\left(\frac{H}{G}\right)^{0.85} + \left[\frac{48\mu lQ}{(2G)^2 GW}\right]\Big/\left[0.5\rho\left(\frac{Q}{GW}\right)^2\right] \tag{59}$$

Elbow and Exit

$$C_l = 1.0 + 0.886\left(\frac{G}{H}\right)^{0.85} + \left[\frac{48\mu lQ}{(2G)^2 GW}\right]\Big/\left[0.5\rho\left(\frac{Q}{GW}\right)^2\right] \tag{60}$$

The measured loss coefficients show high error at lower Reynolds numbers, as was predicted by the uncertainty analysis in Appendix A. At higher Reynolds numbers, the measurements follow the entrance/exit with elbow loss coefficients within +/- 0.5 which is in line with the predicted uncertainty. These loss coefficients are higher for pressurization than those for depressurization as predicted.
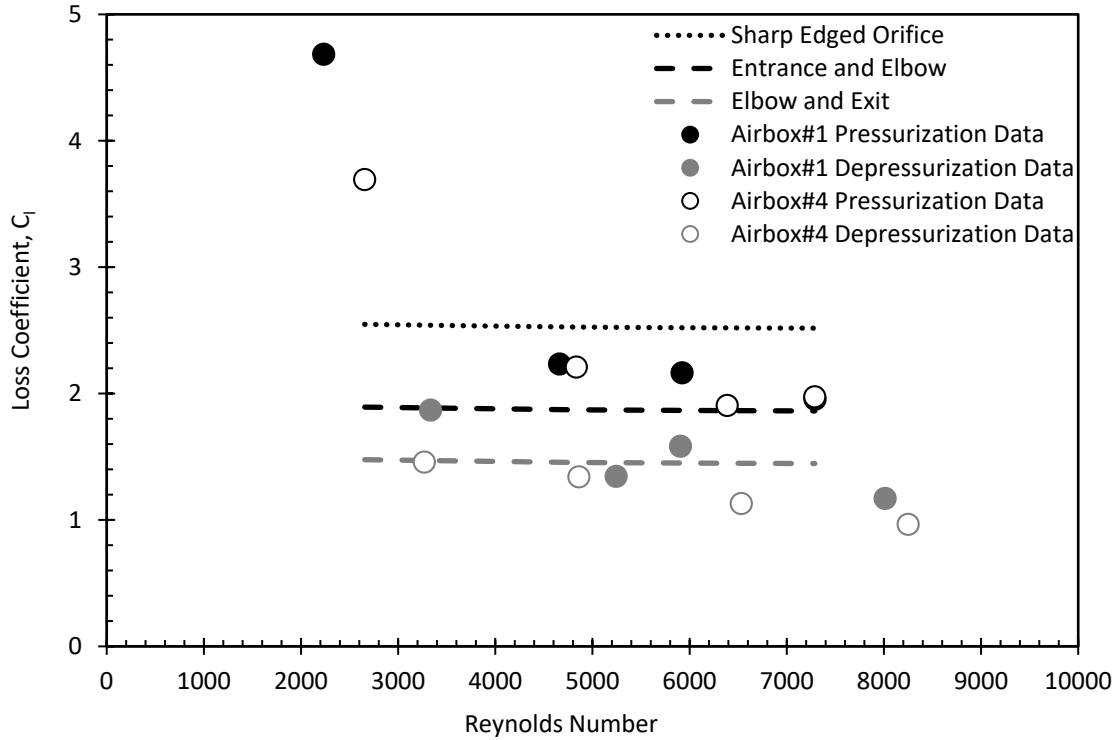
Figure 33: Loss coefficients for orifice flow Reynolds numbers for Airbox#1 and Airbox#4 pressurization for l=6.45mm, G=2.44mm, and H=2.58mm geometry along with discharge equation and elbow flow resistance models with laminar orifice wall friction loss

Friction factors, f, were calculated based on the measured cavity pressure gradients, dp/dx, and measured flowrate, Q, from equation (11) as follows:

$$f = \text{dp/dx}\frac{2A^2}{\rho Q^2}D_h = \text{dp/dx}\frac{2(HW)^2}{\rho Q^2}(2H) \tag{61}$$

Measured cavity flow friction factors relative to Reynolds number (calculated using equation (9)) for a range of flowrates for the short 6.45mm orifice length are plotted in Figure 34. The plot is repeated in Figure 35 for the long 160mm orifice. The plot also includes friction factor approximations from equation (13) for laminar flow and equation (16) for turbulent flow between parallel plates.

The measurements are generally between these two equations for both cases. It is noted that the Reynolds number uncertainty calculated in Appendix A is +/-780 which

contributes high error for the low Reynolds number measurements. The friction factor uncertainty is 0.044 at low flowrate drops to 0.05 at higher flowrates.   These uncertainties may explain the low friction factor values in at Reynolds numbers between 2000 and 6000 in Figure 35. The uncertainty at higher Reynolds numbers, however, is not sufficient to explain the friction factors variation from the laminar flow model, so that these variations are expected to be real.

Within the range of Reynolds number of 3000 to 10000, for the 2.58mm deep cavity the entrance lengths can be estimated using equation (50) for laminar flow to be from 900 to 3000mm. For turbulent flow entrance lengths for the same Reynolds number range are estimated to be 90 to 100mm, based on equation (51). Hence, the flow does not develop fully for part or the entire length of the cavity between the orifices. This issue further complicates modelling of cavity pressure losses and the flow resistance within the entrance may differ from fully developed laminar flow.
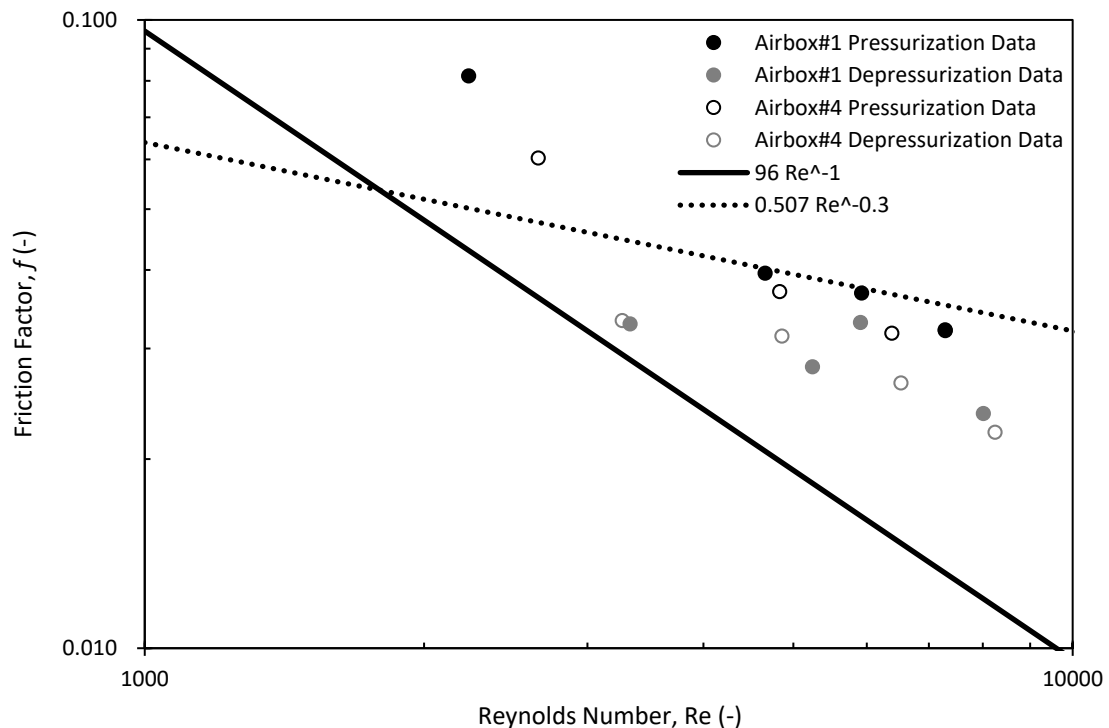
Figure 34: Measured friction factor and Reynolds number values for pressurization and depressurization of Airbox#1 (and Airbox#4) for l=6.45mm and H=2.58mm with predictions based on laminar and turbulent flow approximations
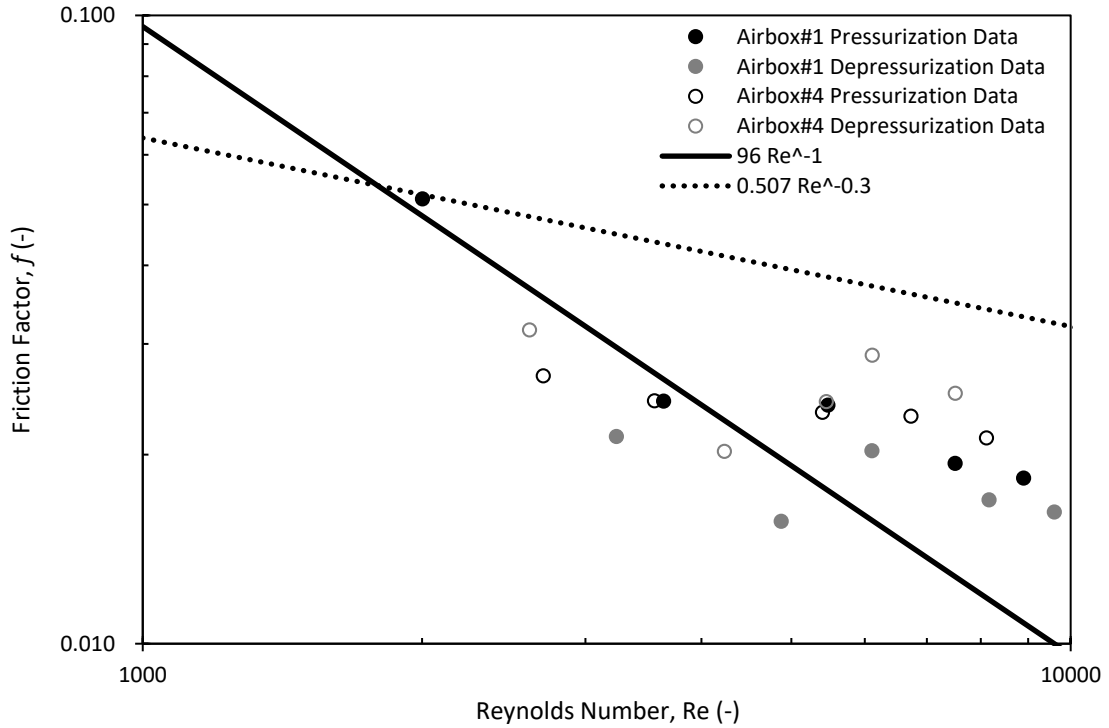
Figure 35: Measured friction factor and Reynolds number values for pressurization and depressurization of Airbox#1 (and Airbox#4) for l=160mm and H=2.58mm with predictions based on laminar and turbulent flow approximations

Pressure loss coefficient measurements for flow from the cavity through the adjacent intermediate orifice were calculated based on the pressure difference between the linear curve fit extensions at x/L=1 as follows:

$$C_l = \left[p_{c,x/L=1} - p_{e,x/L=1}\right] / \left[0.5\rho \left(\frac{Q_b}{GW}\right)^2\right] \tag{62}$$

where $p_{c,x/L=1}$ is the projected pressure at the x/L=1 based on the extension of the earlier described linear curve fit for the $p_{x/L=0.25}$ and $p_{x/L=0.75}$ measurements, $p_{e,x/L=1}$ is the pressure within the airbox adjacent to the pressurized airbox (open to the lab), Q_b is the branch flow to this adjacent airbox. Q_b is predicted based on cavity pressure gradients as follows:

$$Q_b = Q\left[1 - \left(p_{c,x/L=1\,1/4} - p_{c,x/L=1\,3/4}\right) / \left(p_{c,x/L=1/4} - p_{c,x/L=3/4}\right)\right] \tag{63}$$

These measurements are plotted for the 6.45mm and 160mm long orifice setups in Figure 36 and Figure 37, respectively. Predicted loss coefficients are also plotted as calculated below.

<u>Branch, Entrance and Wall Friction</u>

$$C_l = C_p \left(p_{e,x/L=1} - p_{c,x/L=1} \right)^n + 0.5 + \left[\frac{48\mu l Q_b}{(2G)^2 GW} \right] \bigg/ \left[0.5\rho \left(\frac{Q_b}{GW} \right)^2 \right] \tag{64}$$

<u>Branch, Exit and Wall Friction</u>

$$C_l = C_p \left(p_{c,x/L=1} - p_{e,x/L=1} \right)^n + 1.0 + \left[\frac{48\mu l Q_b}{(2G)^2 GW} \right] \bigg/ \left[0.5\rho \left(\frac{Q_b}{GW} \right)^2 \right] \tag{65}$$

where c and n are power law coefficients predicted from ASHRAE (2001) values given in Figure 13.
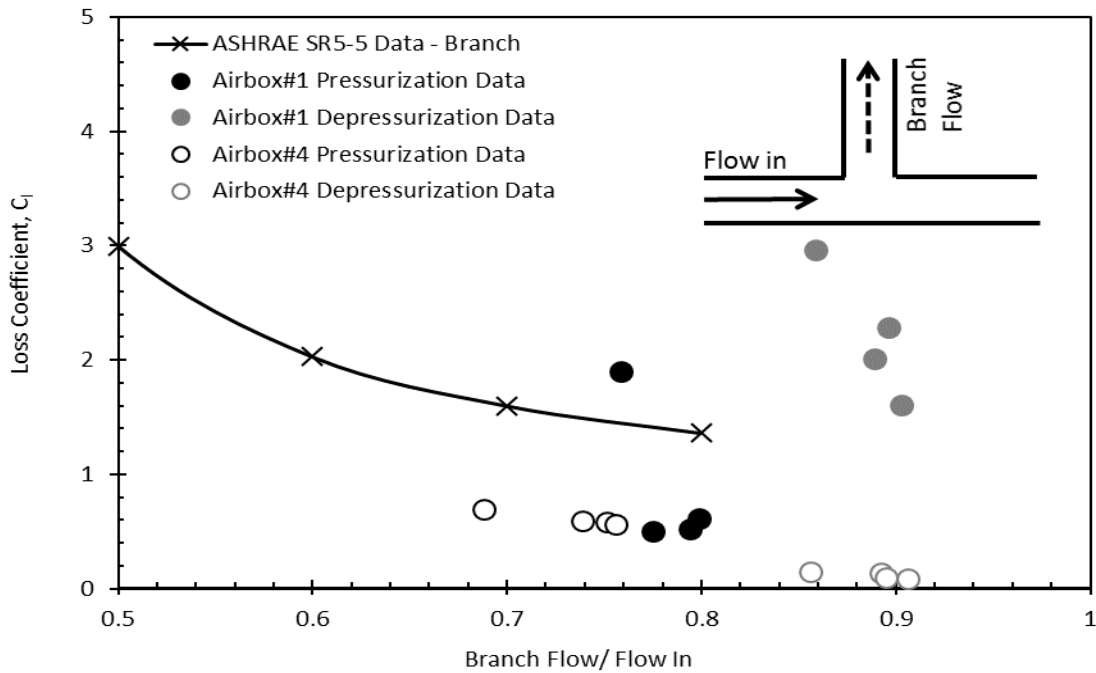
Figure 36: Measured and predicted branch (orifice) loss coefficients for l=6.45mm, G=2.44mm, and H=2.58mm
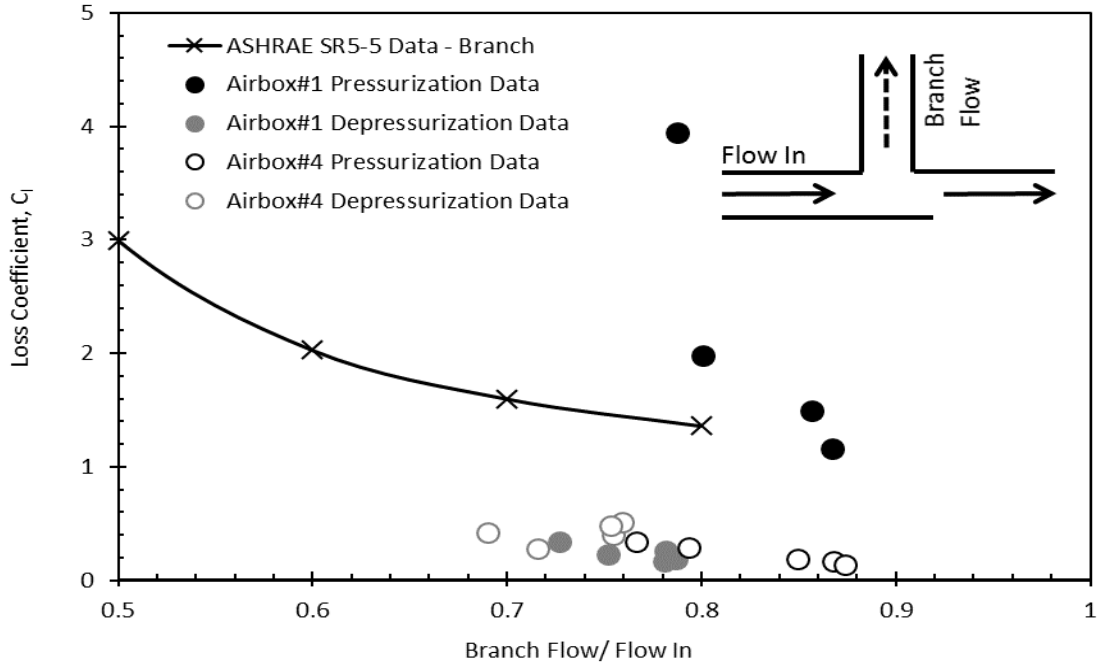
Figure 37: Measured and predicted branch (orifice) loss coefficients for l=160mm, G=2.44mm, and H=2.58mm

Measured loss coefficients were typically lower than predicted values. However, measurements of Airbox#1 depressurization in Figure 36 and pressurization in Figure 37 differed in that they were greater. Furthermore, as the range of flowrate ratios in the measurements was narrow it could not be confirmed if loss coefficients rise with lower flow ratio. The branching flowrate uncertainty calculated in Appendix A is high and its contribution to the loss coefficient likely explains these finding.

Measured loss coefficients for flow along the cavity through the tee intersections were predicted based on the pressure difference between the linear curve fit extensions meeting at x/L=1 as follows

$$C_l = \left[p_{c,x/L=1} - p'_{c,x/L=1} \right] / \left[0.5\rho \left(\frac{Q_t}{HW} \right)^2 \right] \tag{66}$$

where $p_{c,x/L=1}$ is the projected pressure at the x/L=1 orifice based on the extension of the earlier described linear curve fit for the $p_{c,x/L=0.25}$ to $p_{c,x/L=0.75}$ measurements, $p'_{c,x/L=1}$

for the $p_{c,x/L=1.25}$ to $p_{c,x/L=1.75}$ measurements, and cavity flowrate through the tee intersection, Q_t, is calculated from the ratio of pressure gradients as

$$Q_t = Q \cdot \left(p_{c,x/L=1\,1/4} - p_{c,x/L=1\,3/4}\right) / \left(p_{c,x/L=1/4} - p_{c,x/L=3/4}\right) \qquad (67)$$

These measurements are plotted for the 6.45mm and 160mm long orifice setups in Figure 38 and Figure 39, respectively. Predicted loss coefficients are also plotted as calculated follows:

$$C_l = C_p\left(p_{c,x/L=1} - p_{c,x/L=1\prime}\right)^n \qquad (68)$$

where c and n are power law coefficients predicted from ASHRAE (2001) values given in Figure 13. In both in Figure 38 and Figure 39, the measured loss coefficients generally followed but were higher than those predicted using the ASHRAE (2001). The uncertainty of the loss coefficient calculated in Appendix A is high which may explain the scatter in the measured and the difference from the predicted values. However, the results suggest that pressure losses do occur for flow past an intermediate orifice.
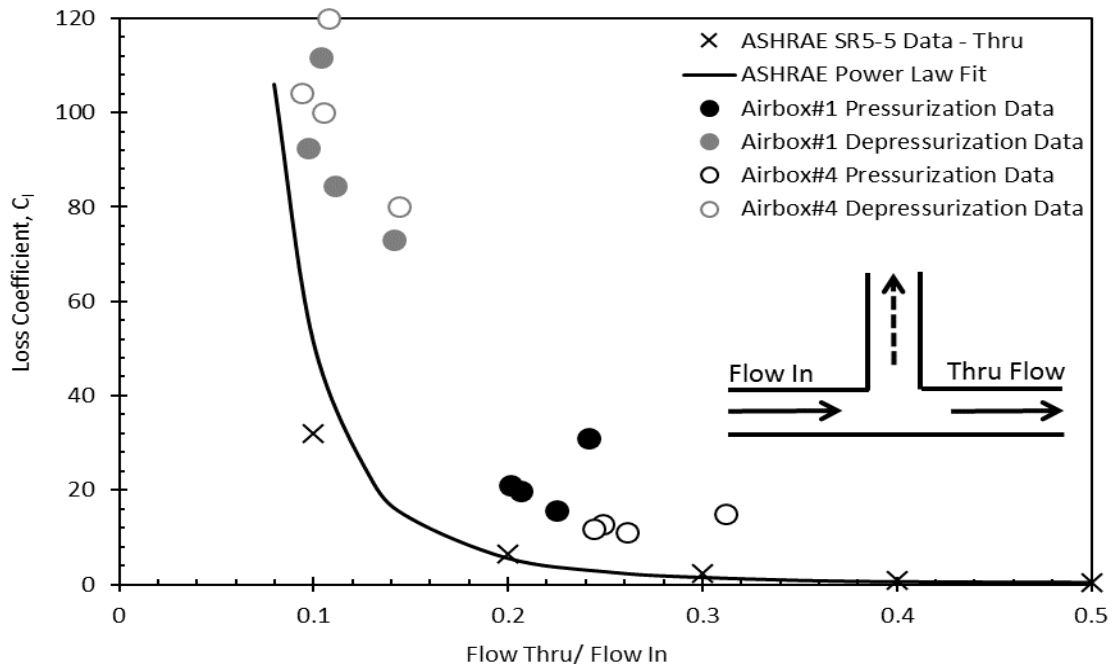
Figure 38: Measured and predicted cavity loss coefficient for cavity flow through a junction for l=6.45mm, G=2.44mm, and H=2.58mm
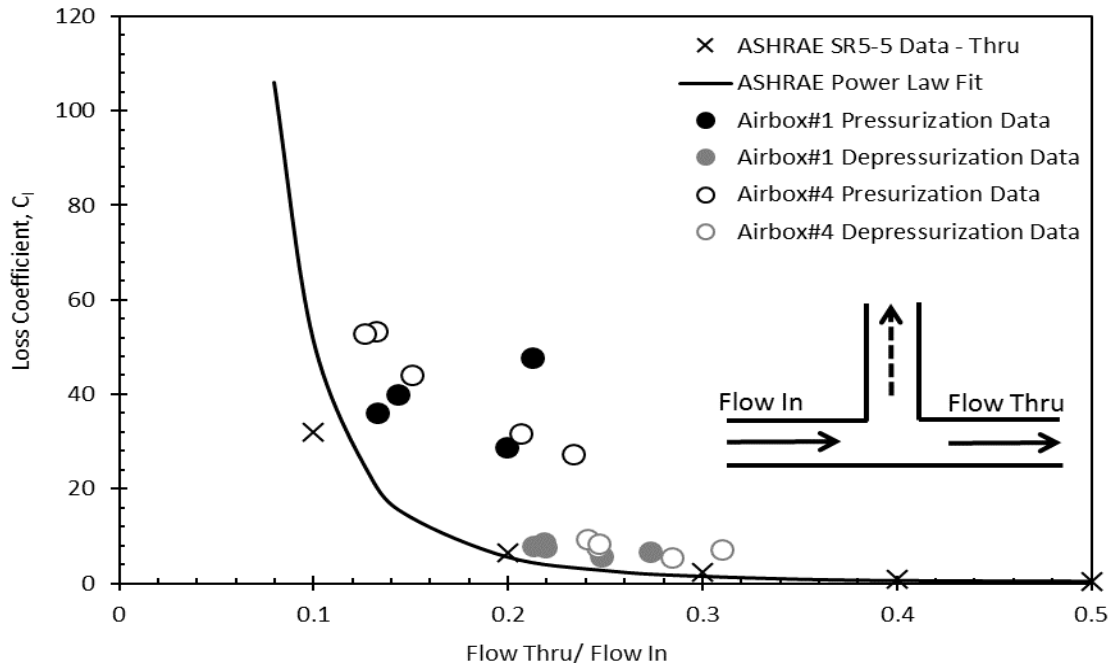
Figure 39: Measured and predicted cavity loss coefficient for cavity flow through a junction for l=160mm, G=2.44mm, and H=2.58mm

3.2.2 Steady Flow Results for End of a Deep Cavity

Cavity pressure measurements for steady 1kPa and -1kPa pressurization for Airbox#1 and Airbox#4 are given in Figure 40. Overall, the cavity pressures are much lower than for the shallow 2.58mm cavity measurements presented in sections 3.2.1, in addition, there is minimal gradient of the pressures along the cavity length. The results are similar for pressurization and depressurization.

Figure 40: Measured non-dimensional cavity pressures for steady pressurization of Airbox#1 and Airbox#4 l=160mm, H=9.46mm, G=2.44mm geometry with linear gradients shown

The loss coefficients for pressure drop across the orifice were predicted like those in 3.2.1 and plotted in Figure 41. The measured values were within +/-0.7 of the sharp-edged orifice equation when orifice wall friction losses are added. There was not a clear difference between entrance/elbow and elbow/exit flows. Furthermore, there was a decline in loss coefficient values at higher Reynolds numbers (suggesting orifice wall friction losses are high). The scatter in measured loss coefficient is high at low Reynolds numbers and better fits the sharp-edged orifice equation at high Reynolds. This aligns with high measurement uncertainty calculated in Appendix A for the lower Reynolds numbers. The sharp-edged orifice equation is a better fit for this scenario than the elbow and entrance/exit loss coefficients. This could because the flow turning to run perpendicular within the cavity is less constrained. Friction factor have not been plotted for this case because pressure gradient along the cavity is too small for this calculation.
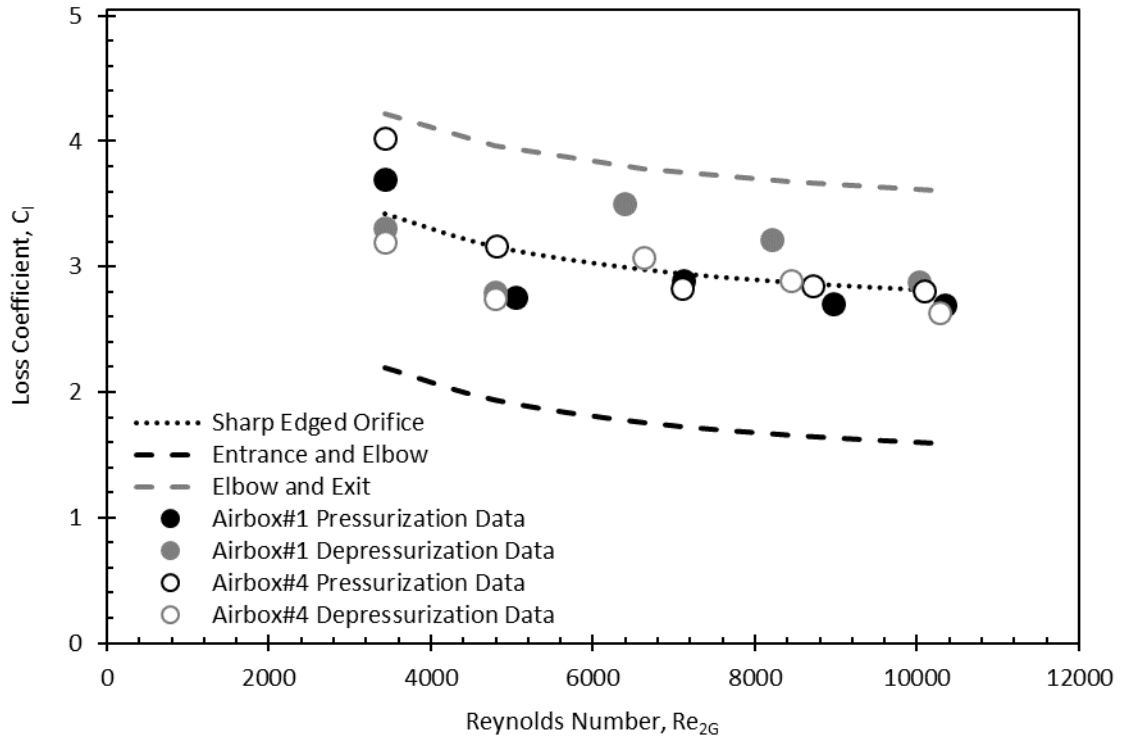
Figure 41: Loss coefficients as a function of Reynolds number, Re2G, for the flow from the Airbox into the cavity for the case: l=160mm, G=2.44mm, and H=9.46mm. Also included are the modeled equations, assuming laminar flow

3.2.3   Steady Flow Through Intermediate Orifice and Shallow Cavity

Flow schematics for pressurization and depressurization of Airbox#2 or Airbox#3 are shown in Figure 42 and Figure 43. The remaining airboxes are left open to the lab environment.
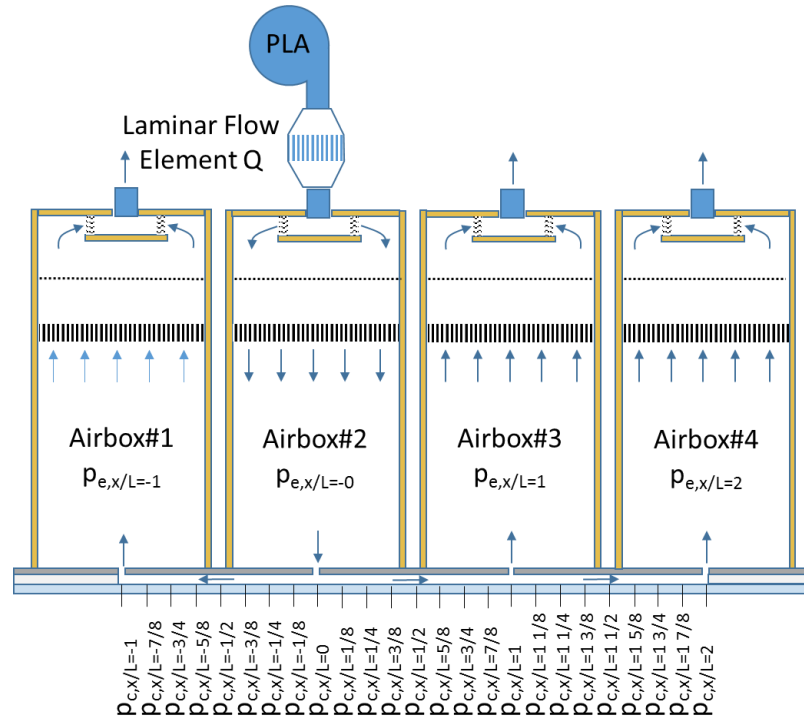
Figure 42: Flow schematic for steady pressurization of Airbox#2
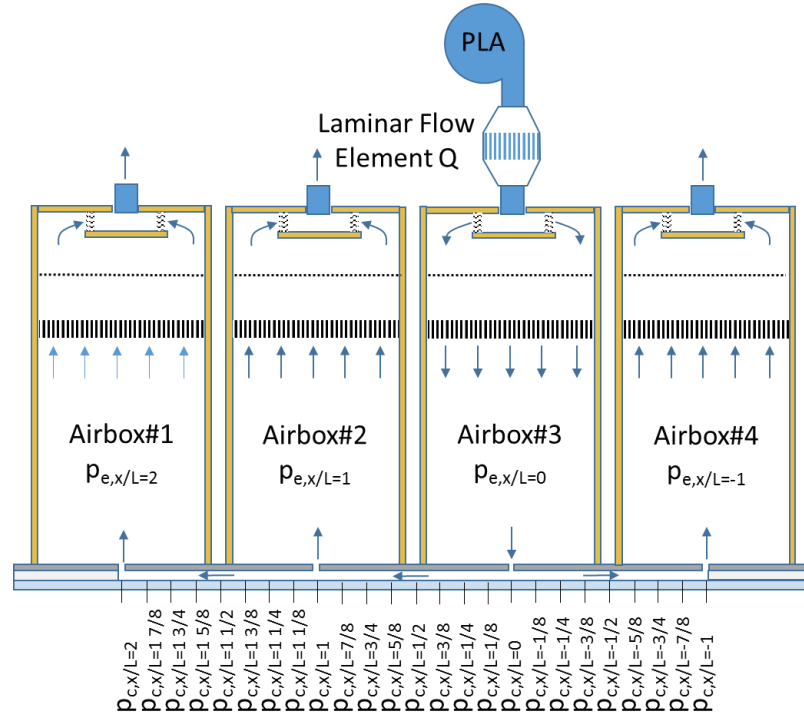
Figure 43: Flow schematic for steady pressurization of Airbox#3

Cavity pressure measurements and linear curve fits and extensions are given in normalized terms Figure 44 for 6.45mm orifice length and 2.58mm cavity depth. As air flow is two directions from the orifice into the cavity, high pressure gradients are found leaving away from the orifice at the pressurized airbox in both directions. A pressure loss for flow across the orifice at x/L=1 can also be seen. This loss is expected to be due to flow through losses as discussed in section 3.2.1. Furthermore, for this setup the measurements are similar for pressurization and depressurization and for Airbox#2 and Airbox#3 showing good experimental repeatability.
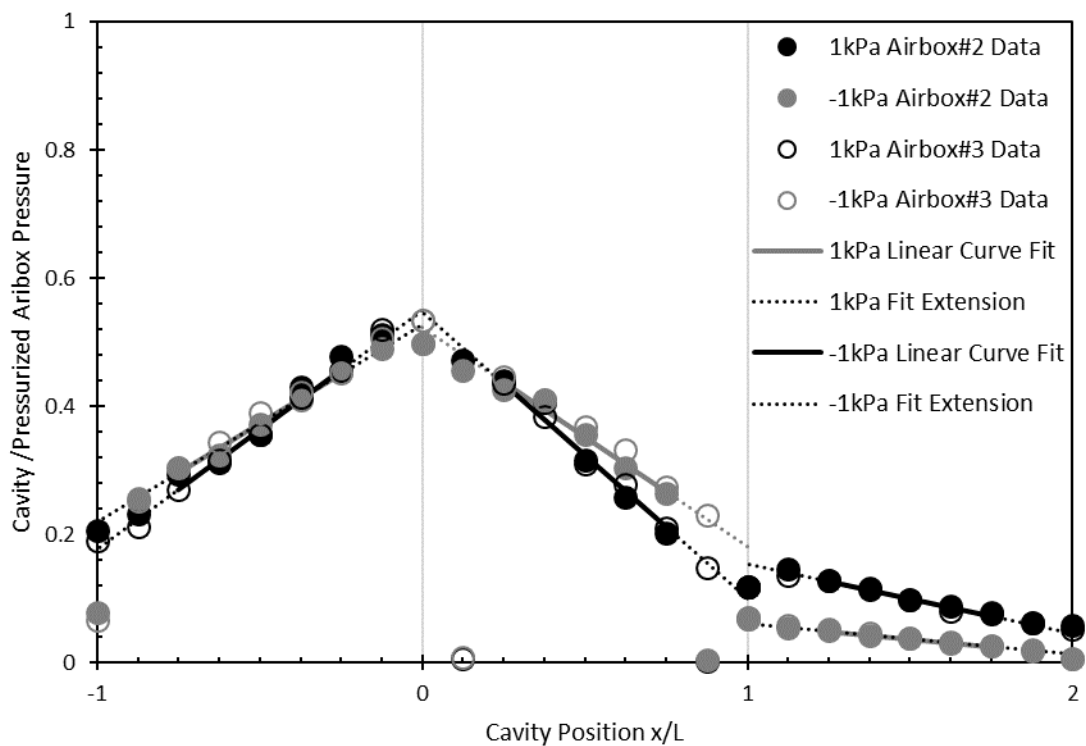
Figure 44: Measured non-dimensional cavity pressures for steady pressurization of Airbox#2 and Airbox#3 l=6.45mm, H=2.58mm, G=2.44mm geometry with linear gradients shown

The same data are plotted in Figure 45 for the long 160mm slot length setups. The pressures are lower than the results for the short 6.45mm slot length setups. Furthermore, there is high variation between the different test configurations, which may due to poor dimensional control of the long slot widths cut through the wood blocks and its alignment with the slots cut through the aluminum sheets.
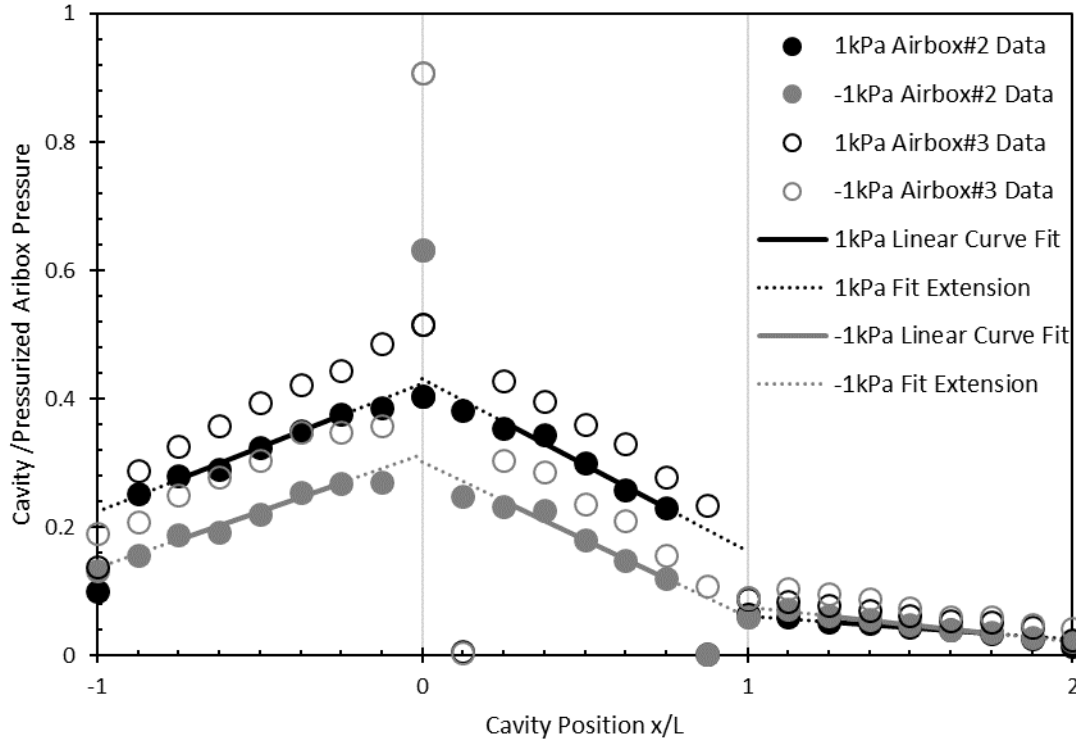
Figure 45: Measured non-dimensional cavity pressures for steady pressurization of Airbox#2 and Airbox#3 l=160mm, H=2.58mm, G=2.44mm geometry with linear gradients shown

The measured orifice loss coefficients have been calculated using equation (54) for a range of flowrates (plotted as orifice flow Reynolds numbers) in Figure 46 for short 6.45mm slot configurations. This data is plotted relative to sharp edged orifice equation (see equation (55)) and approximations for merging and diverging flow (from Idelchik and Fried (1986)) along with entrance or exit loss coefficients and orifice wall friction losses as predicted below. Note that the flowrate within the cavity from either direction out of (or into) the orifice is assumed to be equally divided, which is supported by the similarity of the pressure gradients in the cavity.

$$C_l = 1 + 0.3(2)^2(G/H)^2 + 0.5 + \left[\frac{48\mu l Q}{(2G)^2 GW}\right] \Big/ \left[0.5\rho \left(\frac{Q}{GW}\right)^2\right] \tag{69}$$

$$C_l = 1 + (G/H)^2 + 3(G/H)^2[(0.5)^2 + 0.5] + 1 + \left[\frac{48\mu l Q}{(2G)^2 GW}\right] \Big/ \left[0.5\rho \left(\frac{Q}{GW}\right)^2\right] \tag{70}$$

The short orifice measured loss coefficients are 0.2 to 0.4 greater than the tee loss coefficients from Idelchik and Fried (1986) and the values for merging flow are greater than those for diverging flow for higher Reynolds number (above 6000). These differences are in line with the measurement uncertainty calculated in appendix A. The values are all lower (0.5 to 1.5) than the sharp-edged orifice equation. Hence, the interaction with the perpendicular cavity appears to have an effect for this shallow cavity scenario.
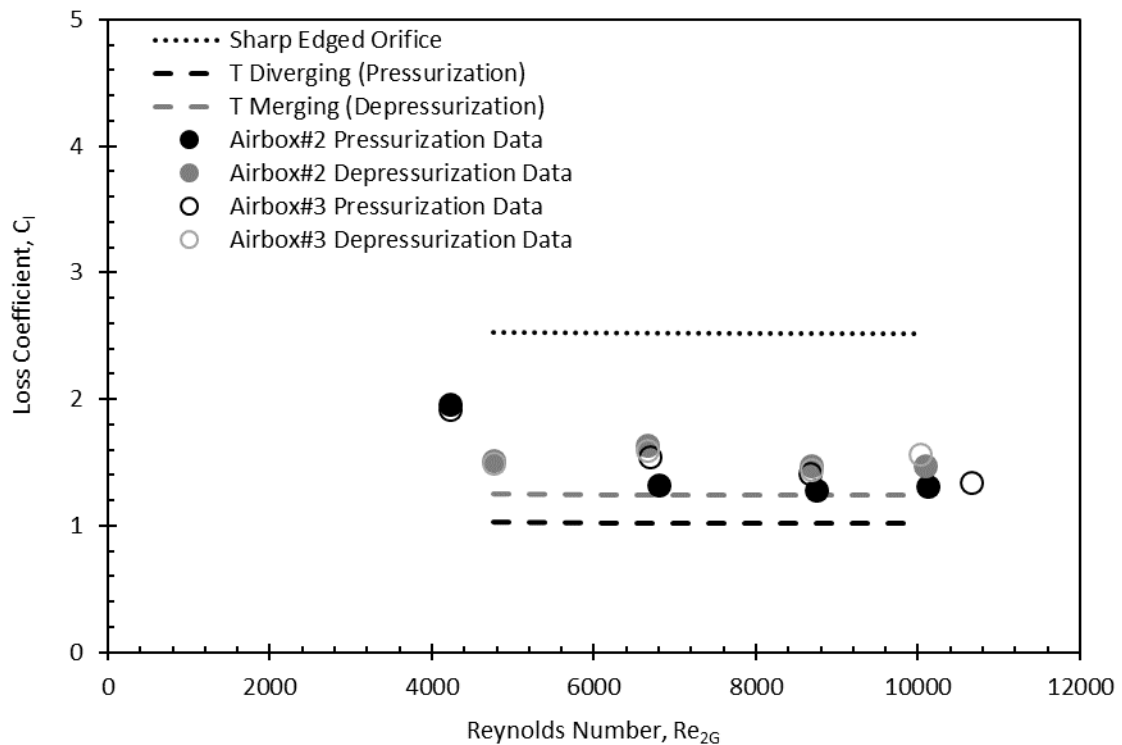
Figure 46: Measured loss coefficient for flow diverging or merging at tee intersection for pressurization and depressurization of Airbox#2 and Airbox#3 for l=160mm, G=2.44mm, and H=2.58mm and Sharp Edged Orifice equation and merging and diverging tee loss coefficients

3.2.4   Steady Flow Through Intermediate Orifice and Deep Cavity

Orifice loss coefficients for the orifice at the pressurized airbox were calculated from measured flowrate and cavity pressures like section 3.2.3 and plotted relative to similar loss coefficient models in Figure 38. The measurements are generally greater but within

0.7 of the sharp-edged orifice equation which is slightly higher than the measurement uncertainty calculated in appendix A. They are greater (more than 1.5) than predictions from Idelchik and Fried (1986). This finding would suggest the flow from an intermediate orifice into the deeper cavity is less constrained like the end cavity orifices.
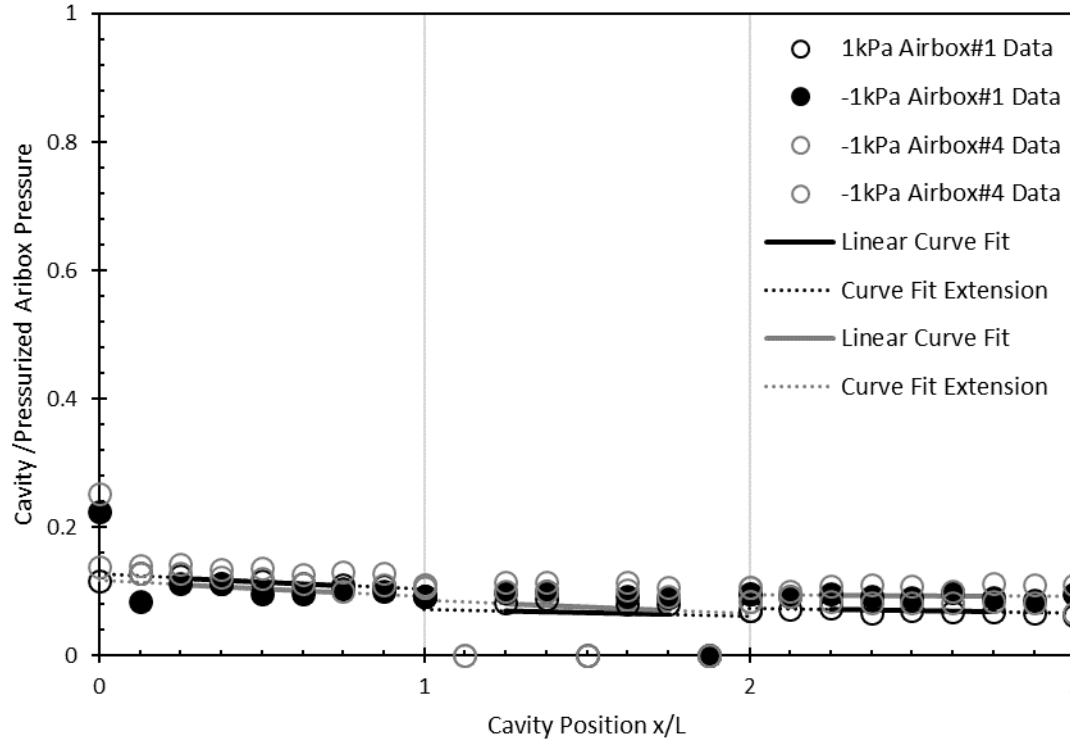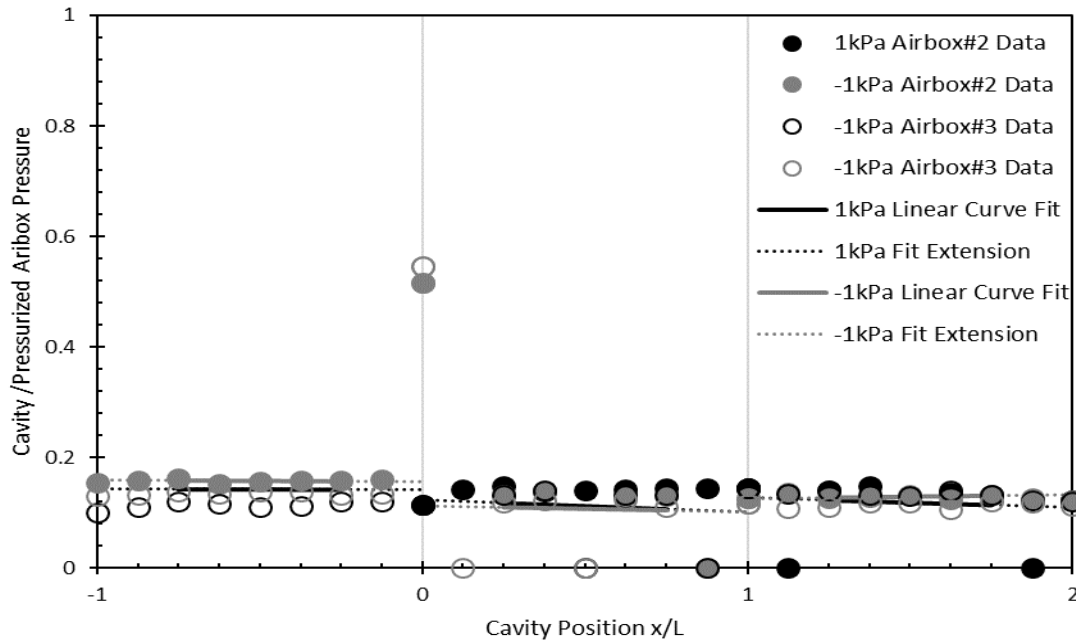

Figure 47: Measured non-dimensional cavity pressures for steady pressurization of Airbox#2 and Airbox#3 l=160mm, H=9.46mm, G=2.44mm with linear gradients shown
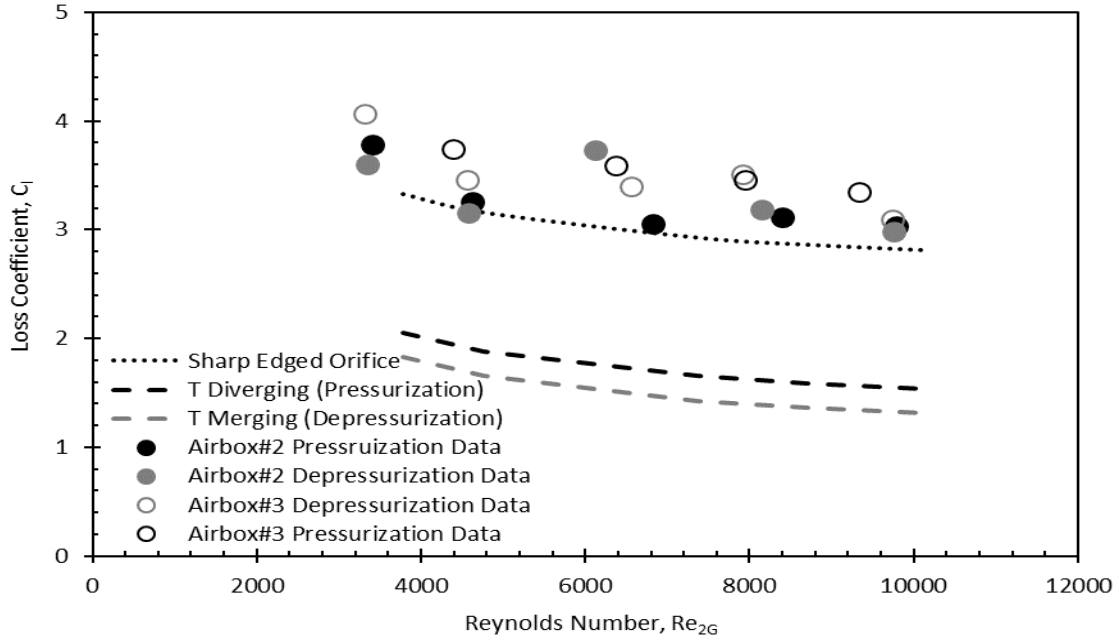
Figure 48: Predicted and measured loss coefficient for flow diverging or merging at tee intersection for pressurization and depressurization of Airbox#2 and Airbox#3 for l=160mm, G=2.44mm, and H=9.46mm and Sharp Edged Orifice equation

3.3   Sinusoid Varying Unsteady Flow

Unsteady flow test scenarios were summarized in Table 1. These tests were run to see if discharge loss terms derived from steady flows hold for unsteady flow and to determine if inertial terms, used by Oh and Kopp (2014) and discussed in Chapter 2, capture full scale effects. The airboxes have been pressurized following simple sinusoidal pressure traces with 1kPa amplitude and 5Hz frequency. Like the steady state tests an individual airbox is pressurized and the remaining airboxes are opened to the lab. Results are presented along with analytical model predictions.

3.3.1   Unsteady Flow Results for End of a Shallow Cavity

Test setup details for the pressurization tests using Airbox#1 (or Airbox#4) were the same as shown in Figure 29 and Figure 30. Varying between pressurization and depressurization within an unsteady flow scenario involves transitions between the flow structures. It is uncertain how pressure equalization would be affected by the high

frequency formation of these structures, particularly with the potentially non-parabolic cavity velocity profiles predicted by Yakhot et al. (1999).

Measured airbox pressures and select cavity pressures, $p_{c,x/L=1/4}$ and $p_{c,x/L=3/4}$, are plotted in Figure 49 and Figure 50 for Airbox#1 and Airbox#4. These pressure taps were selected to show the greatest pressure variation along the length of the cavity while avoiding the effects of flow structures around the opening on pressure taps across from the orifice as discussed in the previous section for steady flows. The data was converted to non-dimensional terms by divided the pressure measurements by the pressurized airbox amplitude (the greater of the positive and negative pressure), P, and time was converted to degrees of a single measured sinusoid cycled. A high cavity pressure gradient occurs. The $p_{c=x/L=1/8}$ pressures are found to rise quickly upon pressurization and peak about 30° before the pressurized airbox peak pressure and then decline.
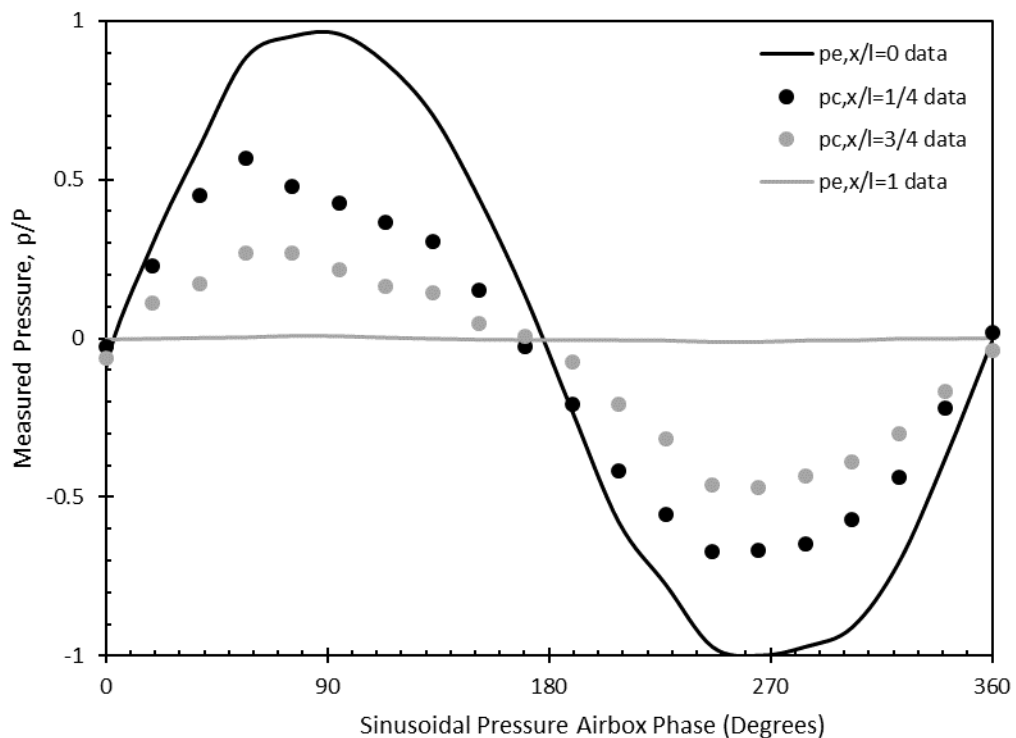
Figure 49: Measured pressures for Airbox#1, unsteady 5Hz pressure trace, l=160mm, G=2.44mm, and H=2.58mm scenario
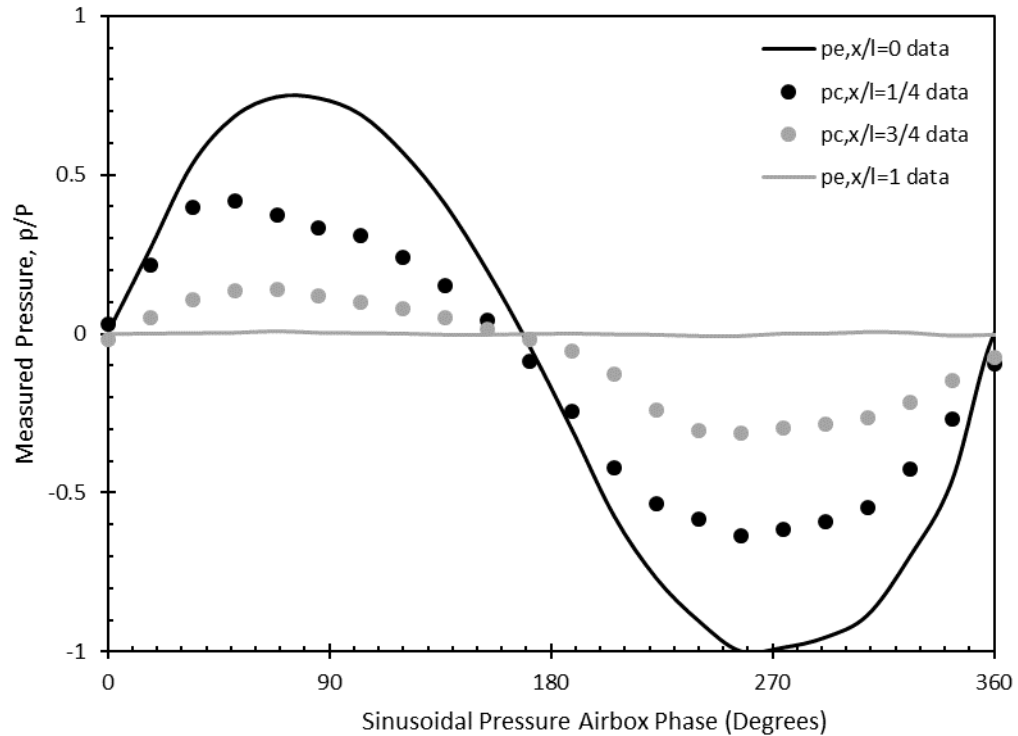
Figure 50: Measured pressures for Airbox#4, unsteady 5Hz pressure trace, l=160mm, G=2.44mm, and H=2.58mm scenario

Oh and Kopp's (2014) model was setup for this simplified cladding configuration as illustrated in Figure 51. This model consisted of 4 continuity equations (at $p_{c,x/L=0}$, $p_{c,x/L=1}$, $p_{c,x/L=2}$, and $p_{c,x/L=2}$), 4 pressure loss equations for orifice flow (for v_1, v_2, v_3, and v_4), and 24 pressure loss equations for cavity flow (between each cavity pressure tap). As the pressure drop within the cavity between the slot orifices is linear, the conditions can be calculated based on just 4 cavity pressures. However, intermediate cavity pressures are calculated for comparison to the measured cavity pressures plotted in Figure 49 and Figure 50.

$p_{c,x/L=0}$ $p_{c,x/L=1/8}$ $p_{c,x/L=1/4}$ $p_{c,x/L=3/8}$ $p_{c,x/L=1/2}$ $p_{c,x/L=5/8}$ $p_{c,x/L=3/4}$ $p_{c,x/L=7/8}$ $p_{c,x/L=1}$ $p_{c,x/L=1\,1/8}$ $p_{c,x/L=1\,1/4}$ $p_{c,x/L=1\,3/8}$ $p_{c,x/L=1\,1/2}$ $p_{c,x/L=1\,5/8}$ $p_{c,x/L=1\,3/4}$ $p_{c,x/L=1\,7/8}$ $p_{c,x/L=2}$ $p_{c,x/L=2\,1/8}$ $p_{c,x/L=2\,1/4}$ $p_{c,x/L=2\,3/8}$ $p_{c,x/L=2\,1/2}$ $p_{c,x/L=2\,5/8}$ $p_{c,x/L=2\,3/4}$ $p_{c,x/L=2\,7/8}$ $p_{c,x/L=3}$

u_3 u_2 u_1

v_4 v_3 v_2 v_1

$p_{e,x/L=2}$ $p_{e,x/L=2}$ $p_{e,x/L=1}$ $p_{e,x/L=0}$
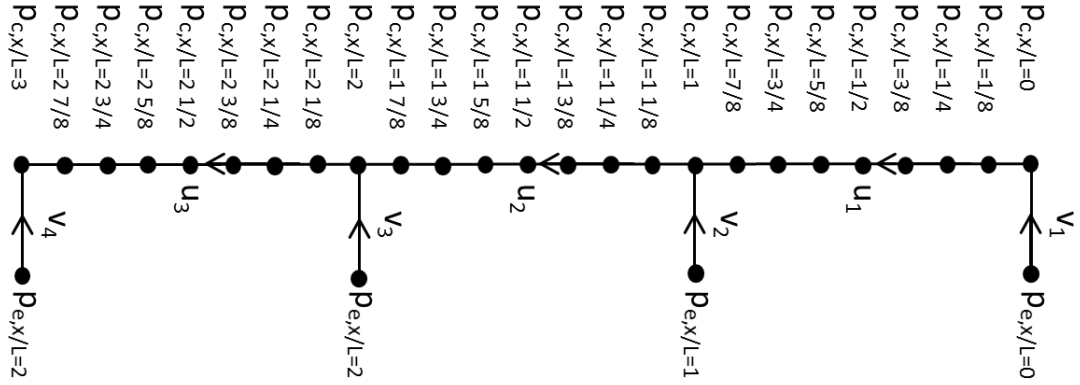
Figure 51: Analytical model for end cavity Airbox#1 and Airbox#4 pressurization

The continuity equations were as follows:

$$v_1(t) = u_1(t) \tag{71}$$

$$v_2(t) = u_1(t) - v_1(t) \tag{72}$$

$$v_3(t) = u_2(t) - v_2(t) \tag{73}$$

$$v_4(t) = -u_3(t) \tag{74}$$

The orifice pressure losses equations were as follows:

$$p_{e,x/L=0}(t) - p_{c,x/L=0}(t) = C_l \frac{1}{2}\rho v_1^2(t) + 12\mu l/G^2 \cdot \frac{1}{2}\rho v_1^2(t) + l_e\rho \frac{dv_1(t)}{dt} \tag{75}$$

…

$$p_{e,x/L=3}(t) - p_{c,x/L=3}(t) = C_l \frac{1}{2}\rho v_4^2(t) + 12\mu l/G^2 \cdot \frac{1}{2}\rho v_4^2(t) + l_e\rho \frac{dv_4(t)}{dt} \tag{76}$$

and

$$p_{c,x/L=0}(t) - p_{c,x/L=1/8}(t) = 12\,\mu L/H^2 \cdot \frac{1}{2}\rho u_1^2(t) + L_e\rho \frac{du_1(t)}{dt} \tag{77}$$

…

$$p_{c,x/L=2\,7/8}(t) - p_{c,x/L=3}(t) = 12\,\mu L/H^2 \cdot \frac{1}{2}\rho u_3^2(t) + L_e\rho \frac{du_3(t)}{dt} \tag{78}$$

The last terms in these equations are the inertial terms which includes acceleration terms, $\frac{dv}{dt}$ and $\frac{du}{dt}$ estimated using a 2nd order, backward differencing numerical approximation of the derivative as follows (Oh and Kopp 2014),

$$\frac{dv(t)}{dt} = \frac{3v(t) - 4v(t-1) + v(t-2)}{2 \cdot dt} \tag{79}$$

and

$$\frac{du(t)}{dt} = \frac{3u(t) - 4u(t-1) + u(t-2)}{2 \cdot dt} \tag{80}$$

where $t = 1, 2, \ldots, n$ in the index, dt is a time step (in the case 0.01s as dictated by the measurement frequency used in the analysis).

Constant model geometries are used based on the average measured geometries (G=2.54mm, l=6.45, H=2.58, W=500mm, L=0.604mm) in the model. The density and dynamic viscosity of air are based on measured airbox air temperature and atmospheric pressure from local airport weather station (see Appendix A for specific calculations). The model did not include loss for flow through the cavity across the tees or more complex elbow/entrance and branch loss coefficients. These were attempted but the resultant model was unable to converge given these more complex loss coefficient calculations and the modelling approach taken. Future modelling effort may overcome these convergence issues allowing use of more complex loss coefficients. However, for this study the model uses a constant loss coefficients, C_l, of 2.5 is used.

The model was run for the previously plotted Airbox#1 and Airbox#4 sinusoidal pressure and compare to measured cavity pressures in Figure 52 and Figure 53. The model matched well with measurements between $0°$ and $180°$ but underestimated the magnitude of negative pressures between $180°$ and $360°$. It is unclear if the difference is due to experimental due to poor geometric control or model error due to the use of a simple constant discharge coefficient.

Figure 52: Measured and predicted pressures for Airbox#1, unsteady 5Hz pressure trace, l=160mm, G=2.44mm, and H=2.58mm scenario

Figure 53: Measured and predicted pressures for Airbox#4, unsteady 5Hz pressure trace, l=160mm, G=2.44mm, and H=2.58mm scenario

The loss and inertial terms predicted for unsteady pressurization are plotted in Figure 54. The greatest magnitude terms are the pressurized airbox orifice discharge loss term, $C_l \frac{1}{2}\rho v_1^2$, the same term for the adjacent airbox orifice (as most of the air exiting at this location) and the cavity friction loss term, $12 \ \mu L/H \cdot \frac{1}{2}\rho u_1^2$. The cavity inertial term, $L_e\rho \frac{du_1(t)}{dt}$, is also high. The loss terms all follow the airbox pressurization while the inertial terms at 30° out of phase. The inertial terms further have a much sharper (less rounded) peak. The orifice friction loss terms are small even for this "long" orifice case. The remaining loss and inertial terms are small as there is little airflow through the remainder of the flow network.
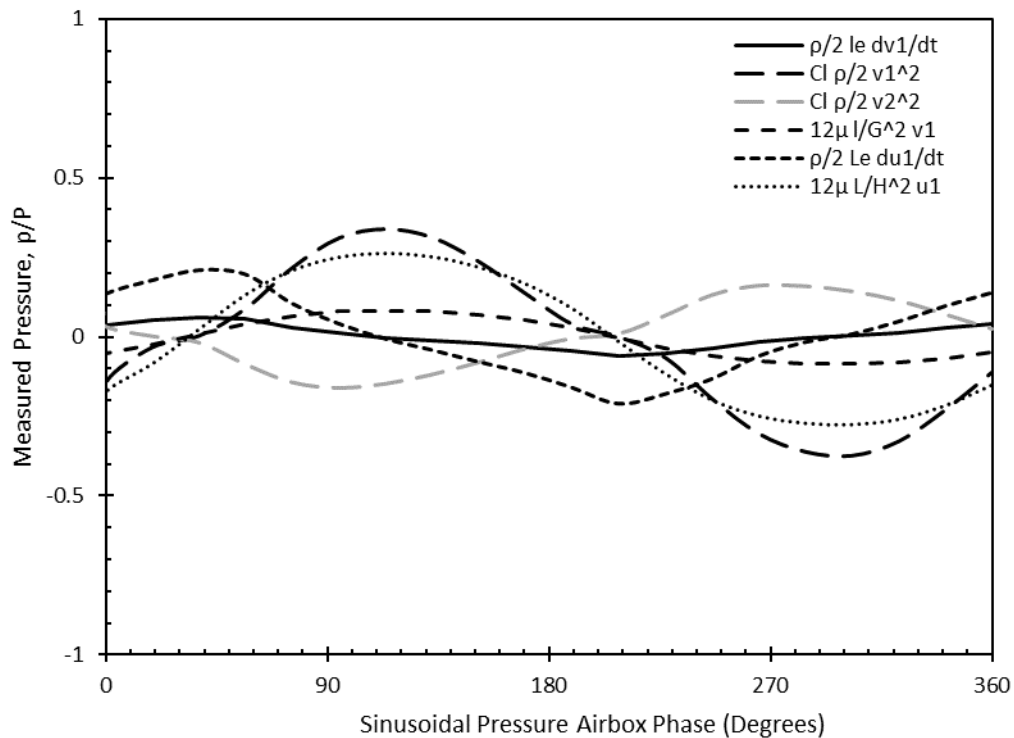
Figure 54: Predicted model loss and inertial terms for Airbox#1, unsteady 5Hz pressure trace, l=160mm, G=2.44mm, and H=2.58mm scenario

3.3.2   Unsteady Flow Results for End Orifice and Deep Cavity

Unsteady phenomenon discussed in section 3.3.1 for the shallow cavity are expected to be greater for the deep cavity because the flow structures are less constrained and the Richardson annulus effects are predicted to be greater as shown in section 2.3.5.

Airbox pressures and select cavity pressures are plotted in Figure 55 and Figure 56 in similar non-dimensional terms as section 3.3.1 for Airbox#1 and Airbox#4. The cavity pressures are 20% to 30% lower than for the shallow 2.58mm cavity configuration. The pressures were found to rise quickly upon pressurization and depressurization, peak at about 30° before the peak airbox pressure like the shallow 2.58mm cavity.
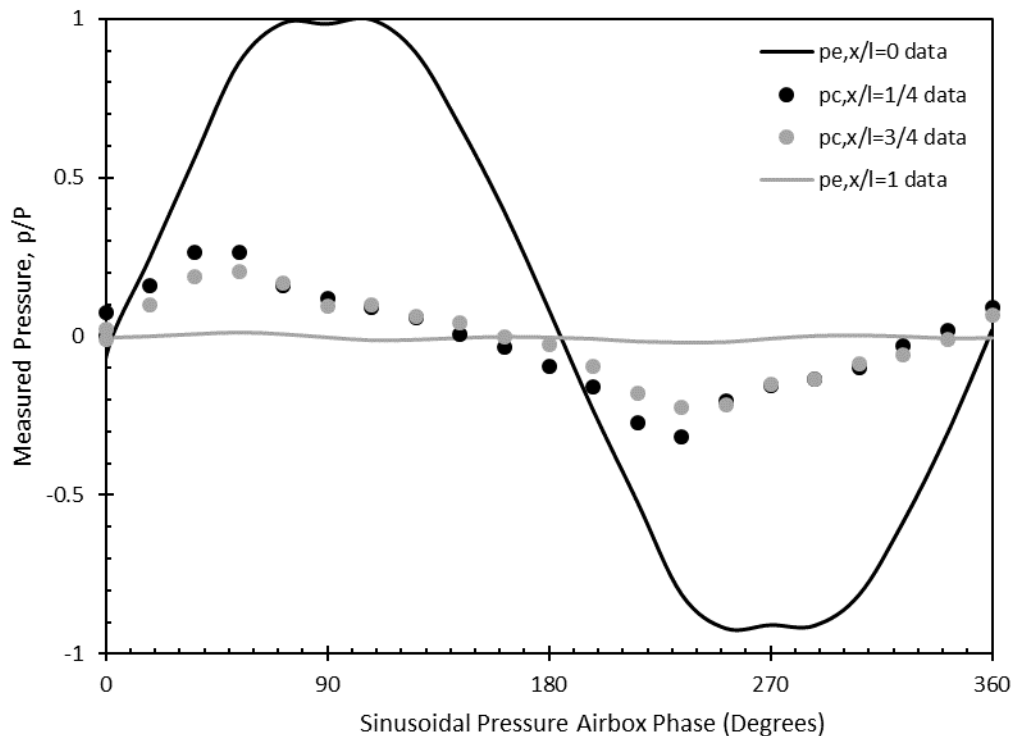
Figure 55: Measured pressures for Airbox#1, unsteady 5Hz pressure trace, l=160mm, G=2.44mm, and H=9.46mm scenario
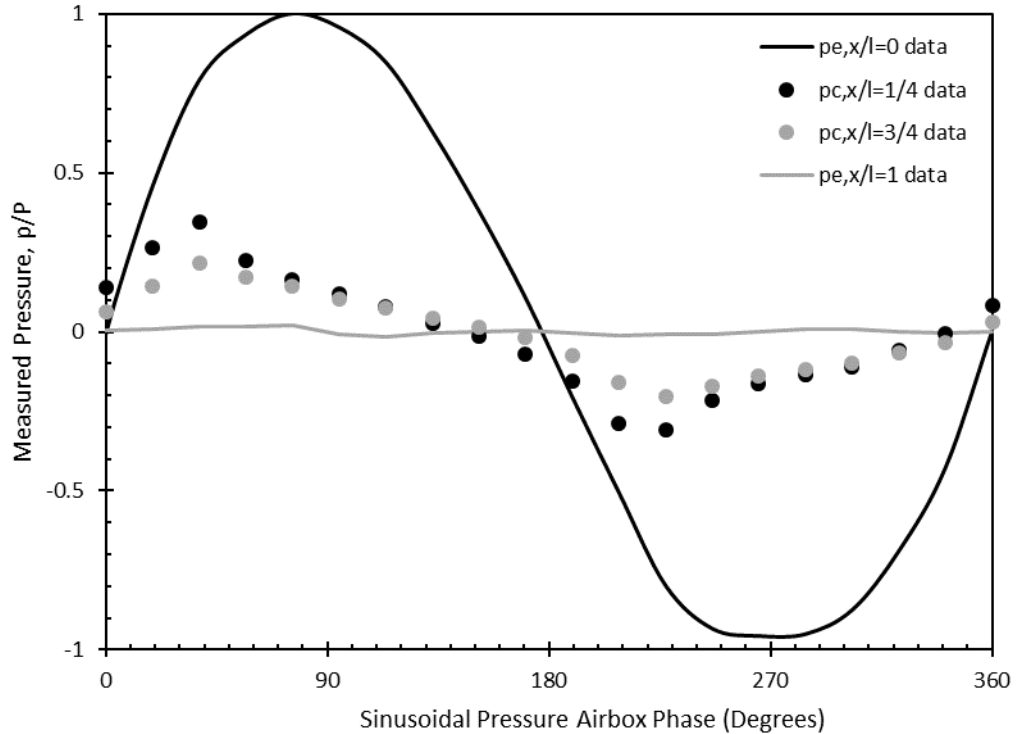
Figure 56: Measured pressures for Airbox#4, unsteady 5Hz pressure trace, l=160mm, G=2.44mm, and H=9.46mm scenario

An analytical model was setup identical to that used for the shallow cavity in section 3.3.1 but with H set to 9.46mm. The model results for pressurization of airbox#1 and airbox#4 given in Figure 57 and Figure 58 show that the model accurately predicted cavity pressures within +/- 5% of 1kPa amplitude. This is greater than the 16Pa calculated pressure measurement uncertainty and may be due the limited accuracy of discharge loss calculations in the model. Furthermore, the model accurately predict cavity pressures for both pressurization and depressurization. This may differ from the shallow cavity measurements because of the directional loss coefficient dependency.
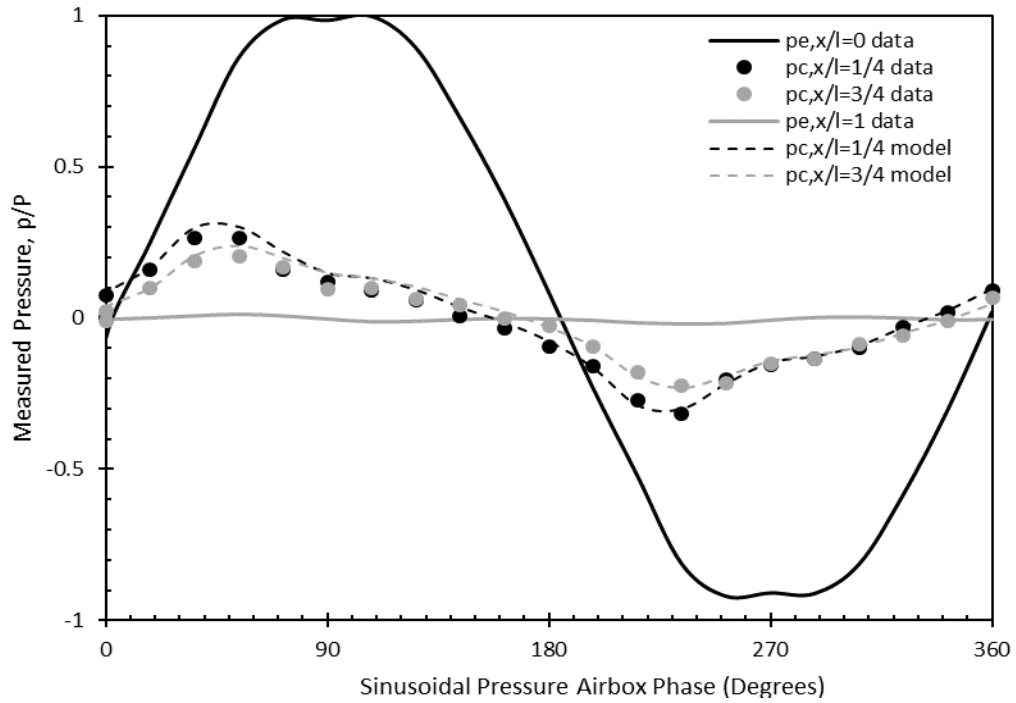
Figure 57: Measured and predicted pressures for Airbox#1, unsteady 5Hz pressure trace, l=160mm, G=2.44mm, and H=9.46mm scenario

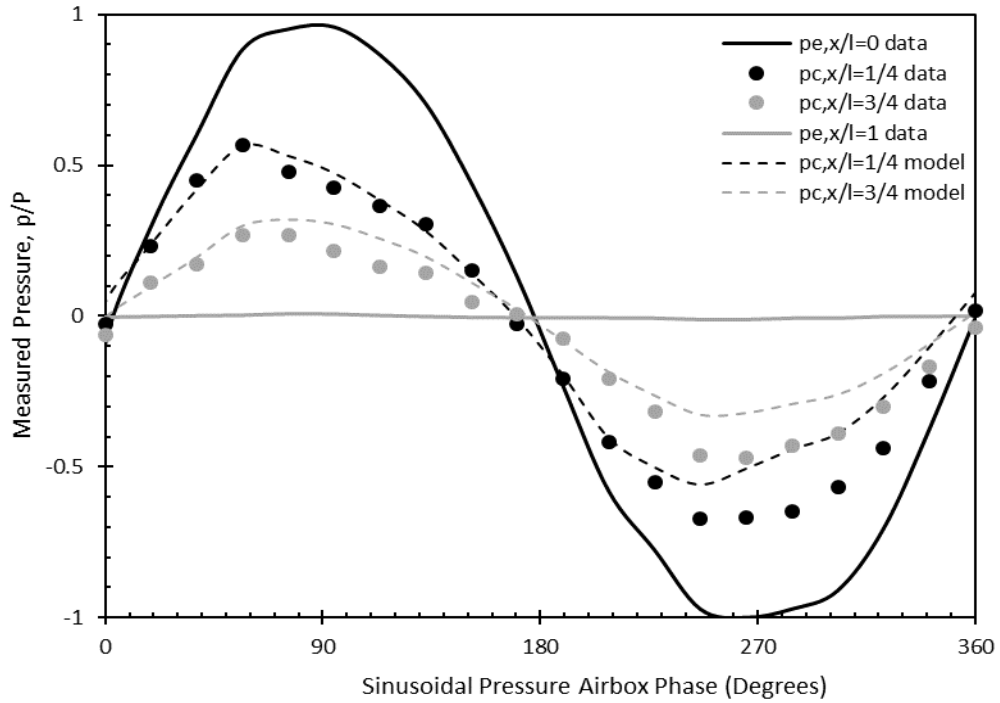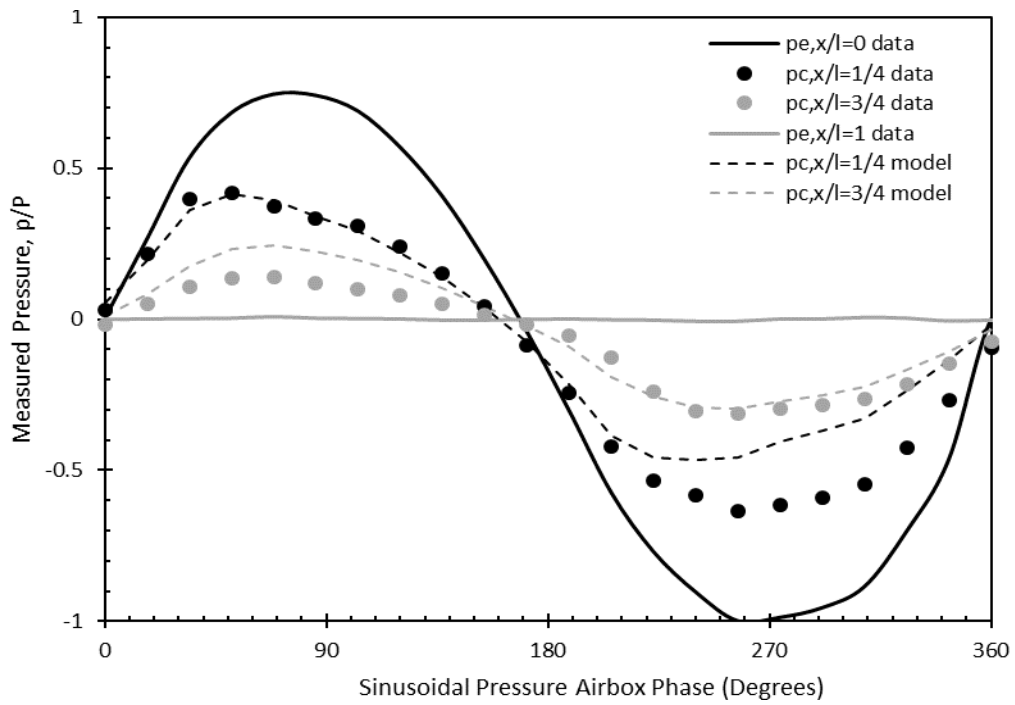Figure 58: Measured and predicted pressures for Airbox#4, unsteady 5Hz pressure trace, l=160mm, G=2.44mm, and H=9.46mm scenario

The loss and inertial terms predicted for unsteady pressurization are plotted in Figure 59. The pressurized airbox orifice discharge loss term, $C_l \frac{1}{2}\rho v_1^2$ is much greater than the remaining terms and explains why the cavity pressures are lower for this deep cavity scenario. This term along with the same term for adjacent airbox and the cavity friction loss term, $12\,\mu L/H \cdot \frac{1}{2}\rho u_1^2$ follow the airbox sinusoidal pressures while once again the inertial terms are 30° out of phase. The remaining terms are small.

Figure 59: Predicted model loss and inertial terms for Airbox#1, unsteady 5Hz pressure trace, l=160mm, G=2.44mm, and H=9.46mm scenario

3.3.3 Unsteady Flow Through an Intermediate Orifice and Shallow Cavity

Test setup details for pressurization for Airbox#2 and Airbox#3 are the same as shown in Figure 42 and Figure 43. Varying between pressurization and depressurization within an unsteady flow scenario involves transitions between the flow structures. It is uncertain how pressure equalization would be affected by high frequency transitions between these

structures and potential non-parabolic cavity velocity profiles as predicted by Yakhot et al. (1999).

Airbox pressures and select cavity pressures are plotted in Figure 61 and Figure 56 in similar non-dimensional terms as section 3.3.1 for Airbox#1 and Airbox#4. The cavity pressures and pressure gradient are like that for the pressurization of the end of cavity airboxes. The pressures were found to rise quickly upon pressurization and depressurization, peak about 30° before the pressurized airbox peak pressure and then slowly decline like the shallow 2.58mm cavity under pressurization. The reason why the phase shift occurs in this case for both pressurization and depressurization may be because the discharge loss coefficients are more similar under both conditions than for merging and diverging flows than for elbows.

An analytical model was setup identical to that used for the shallow cavity in section 3.3.1 but with different nomenclature to match the cavity pressure nomenclature as shown in Figure 60. The model results for pressurization of airbox#1 and airbox#4 given in Figure 57 and Figure 58 show that the model predicted cavity pressures as much as 15% of 1kPa amplitude lower than measured for positive pressures and as much as 25% lower in magnitude for negative pressure while predicting negative pressure peaks somewhat early
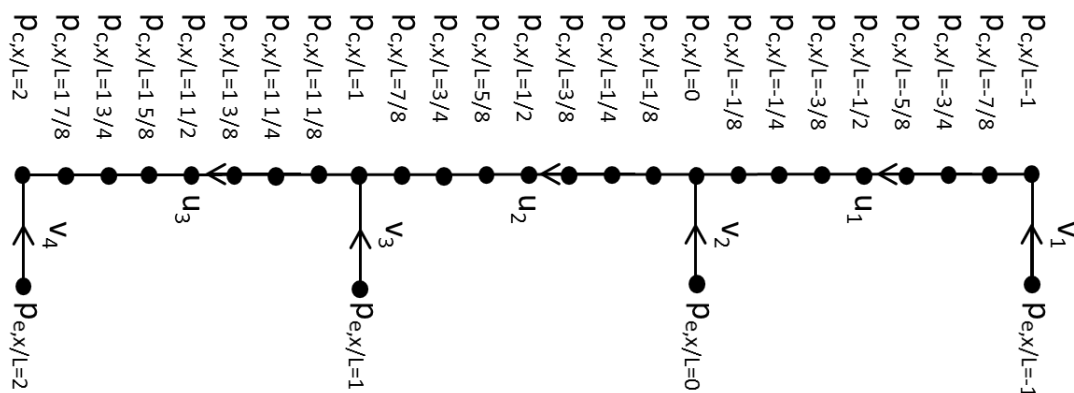
Figure 60: Analytical model for mid cavity Airbox#2 and Airbox#3 pressurization

The loss and inertial terms predicted for the Airbox#1 unsteady pressurization are plotted in Figure 59. The pressurized airbox orifice discharge loss term, $C_1 \frac{1}{2}\rho v_1^2$ is much greater than the remaining terms as the cavity losses are reduced due to the division of flow. Otherwise the terms are like end of cavity models in that the discharge losses for adjacent airbox orifice and cavity friction loss, $12\frac{\mu L}{H} \cdot \frac{1}{2}\rho u_1^2$ are high and following the airbox sinusoidal pressures while once again the inertial terms are 30° out of phase and the cavity terms is high. The remaining terms are small.
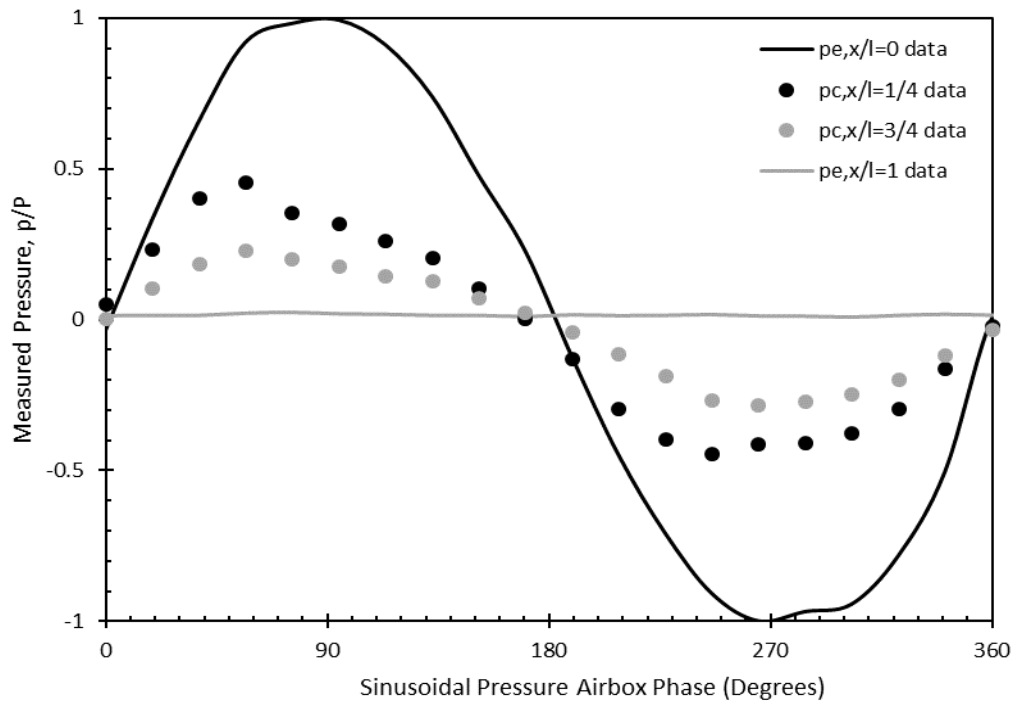
Figure 61: Measured pressures for Airbox#2, unsteady 5Hz pressure trace, l=160mm, G=2.44mm, and H=2.58mm scenario
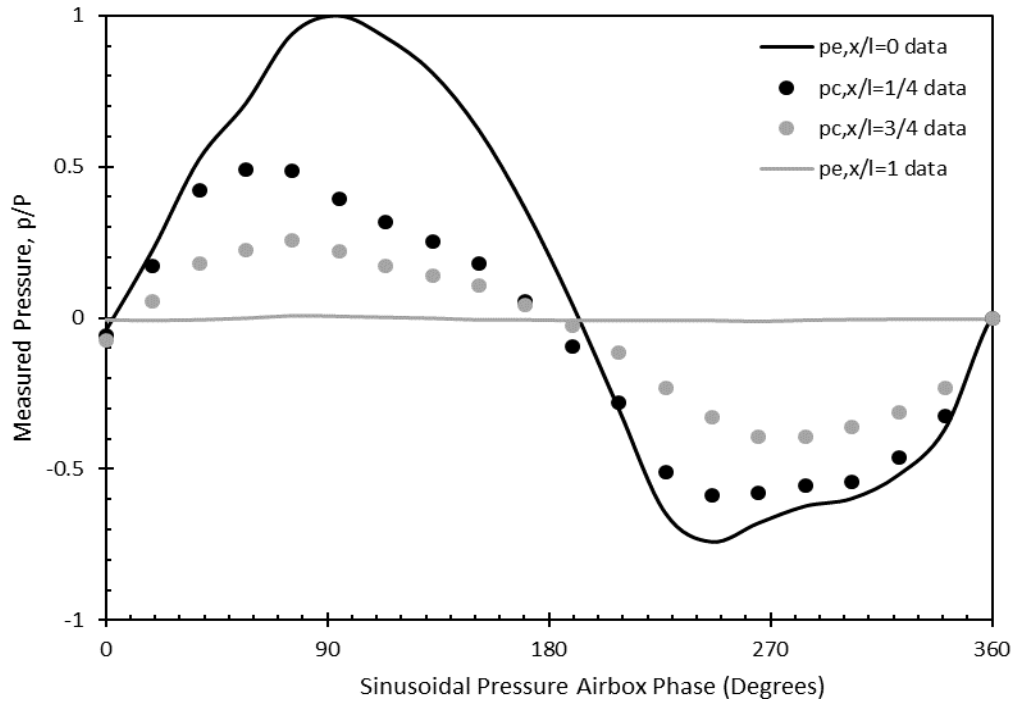
Figure 62: Measured pressures for Airbox#3, unsteady 5Hz pressure trace, l=160mm,

G=2.44mm, and H=2.58mm scenario
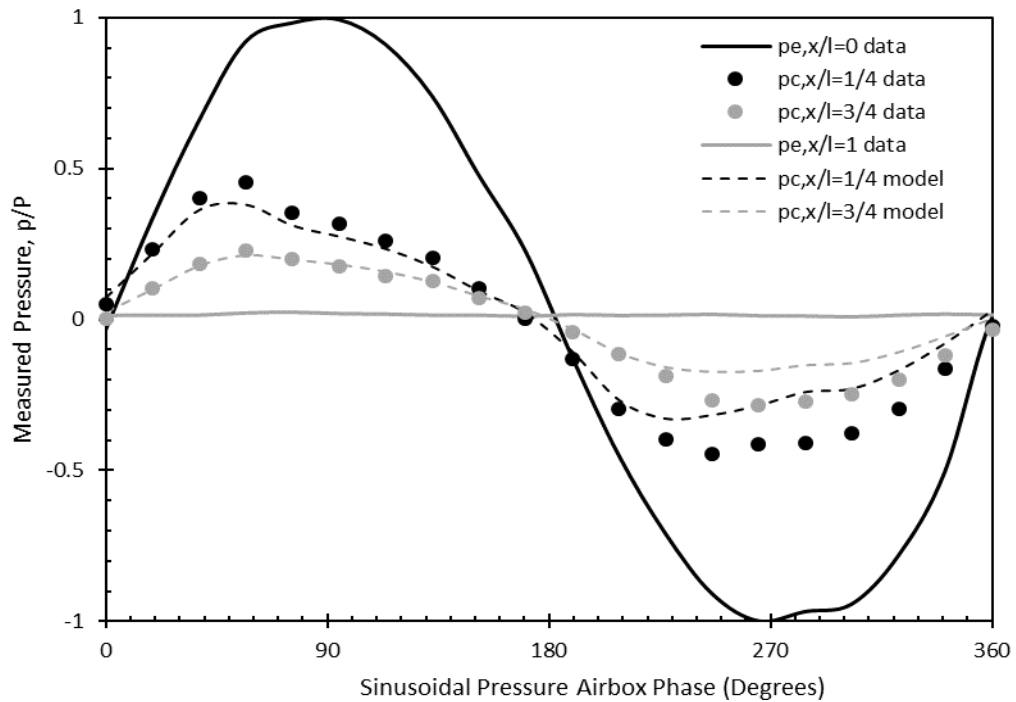
Figure 63: Measured and predicted pressures for Airbox#2, unsteady 5Hz pressure trace,

l=160mm, G=2.44mm, and H=2.58mm scenario
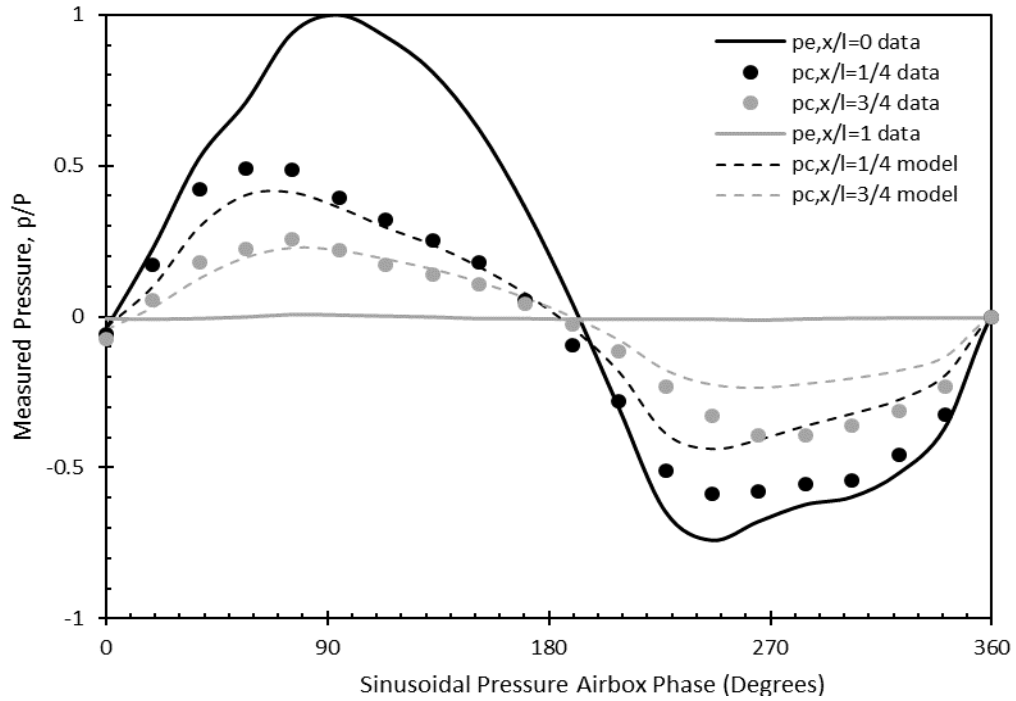
Figure 64: Measured and predicted pressures for Airbox#3, unsteady 5Hz pressure trace, l=160mm, G=2.44mm, and H=2.58mm scenario
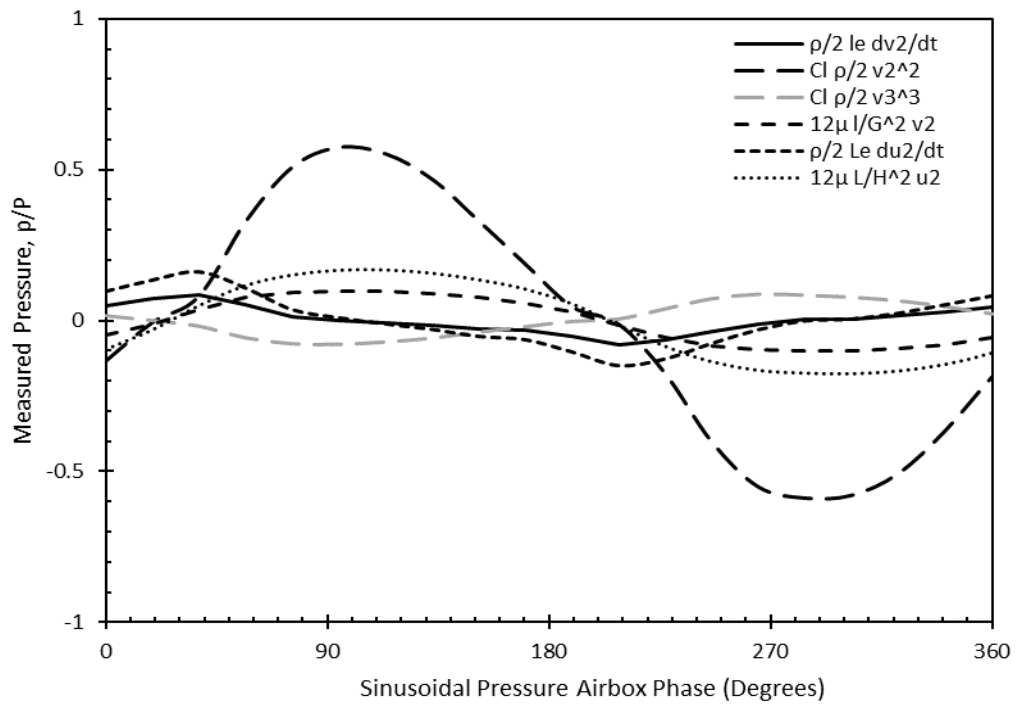
Figure 65: Predicted model loss and inertial terms for Airbox#2, unsteady 5Hz pressure trace, l=160mm, G=2.44mm, and H=2.58mm scenario

3.3.4 Unsteady Flow Through Intermediate Orifice and Deep Cavity

Unsteady phenomenon discussed in section 3.3.3 for the shallow cavity are expected to be higher for the deep cavity because the flow structures are less constrained and the Richardson annulus effects are predicted to be higher as shown in section 2.3.5

Airbox pressures and select cavity pressures are plotted in Figure 66 and Figure 67 in similar non-dimensional terms as section 3.3.1 for Airbox#2 and Airbox#3. The cavity pressures and pressure gradient are much lower than for the shallow 2.58mm cavity configuration. The pressures peak about 30° before the pressurized airbox peak pressure and then slowly decline like the shallow 2.58mm cavity under pressurization and depressurization. The reason why the phase shift occurs in this case for both pressurization and depressurization may be because the discharge loss coefficients are more similar under both conditions than for shallow cavities.

An analytical model was setup identical to that used for the shallow cavity in section 3.3.3 but with H set to 9.46mm. The model results for pressurization of airbox#2 and airbox#3 given in Figure 68 and Figure 69 show that the model accurately predicted cavity pressures within +/- 5% of 1kPa amplitude.

The loss and inertial terms predicted for the Airbox#1 unsteady pressurization are plotted in Figure 70. The pressurized airbox orifice discharge loss term, $C_l \frac{1}{2}\rho v_1^2$ is much greater than the remaining terms as the cavity losses are reduced due to the division of flow. Otherwise the terms are like end of cavity models in that the discharge losses for adjacent airbox orifice and orifice friction loss, $12\frac{\mu L}{H} \cdot \frac{1}{2}\rho u_1^2$ are high and following the airbox sinusoidal pressures. The remaining loss terms are small. The inertial terms are once again the inertial terms are 30° out of phase and the both cavity and orifice terms are small.
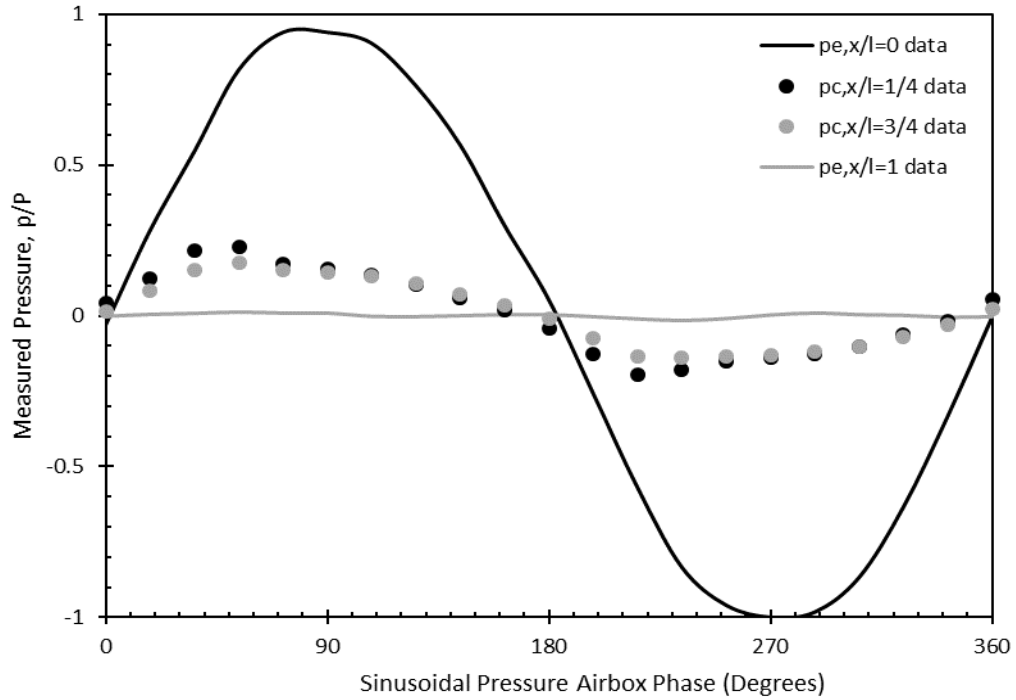
Figure 66: Non-dimensional measurement results for Airbox#2, unsteady 5Hz pressure
trace, l=160mm, G=2.44mm, and H=9.46mm scenario
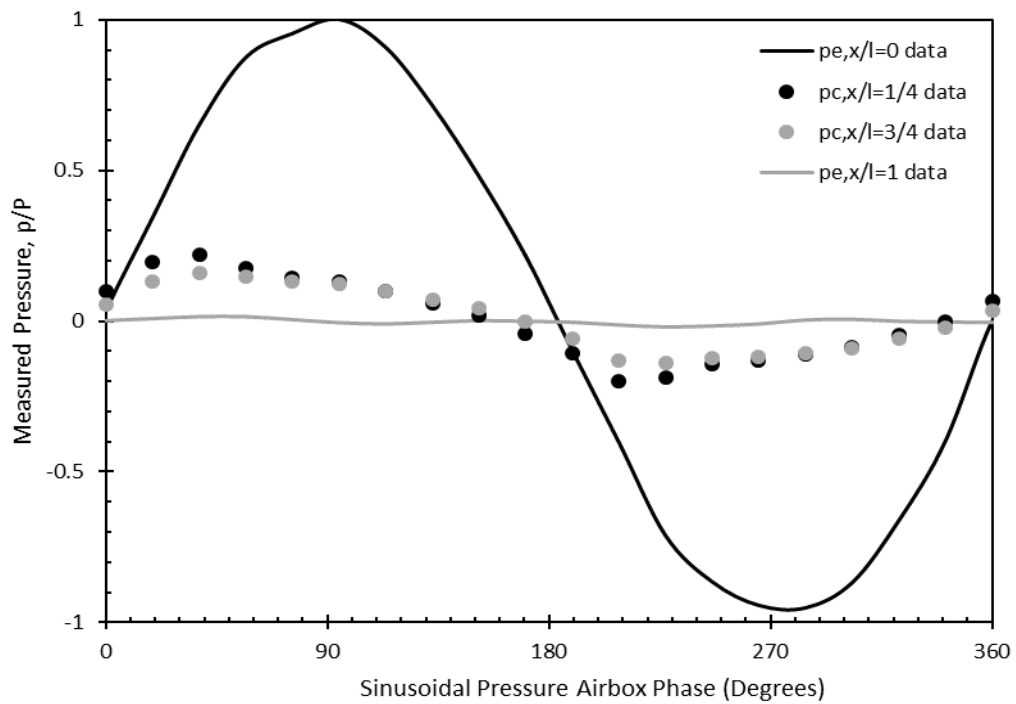
Figure 67: Non-dimensional measurement results for Airbox#3, unsteady 5Hz pressure
trace, l=160mm, G=2.44mm, and H=9.46mm scenario
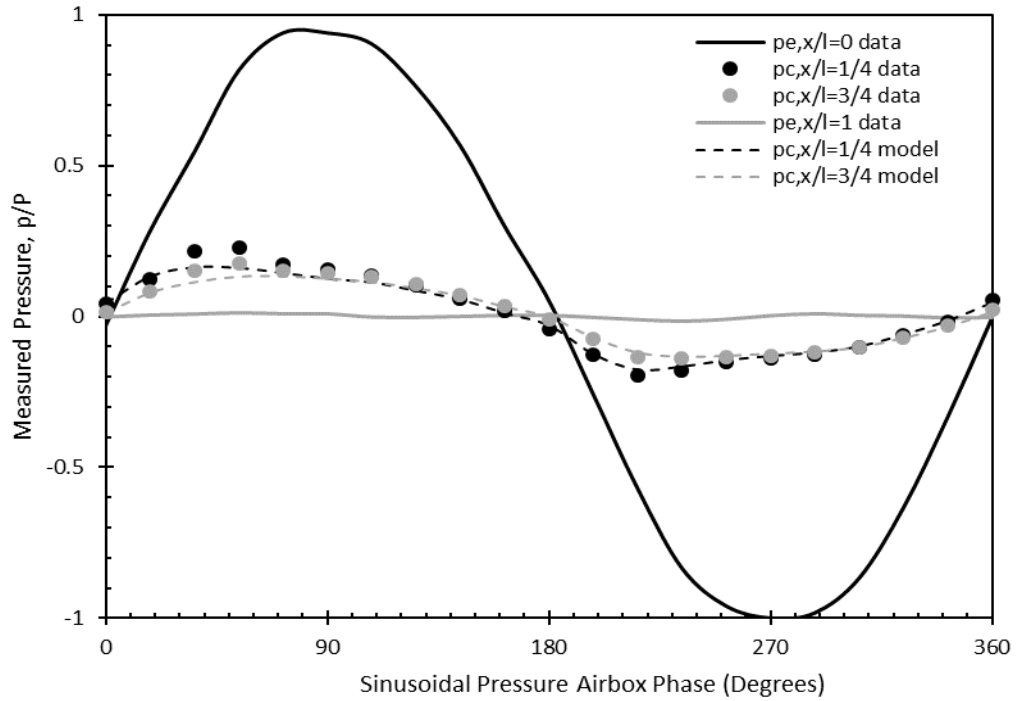
Figure 68: Measured and predicted pressures for Airbox#2, unsteady 5Hz pressure trace,
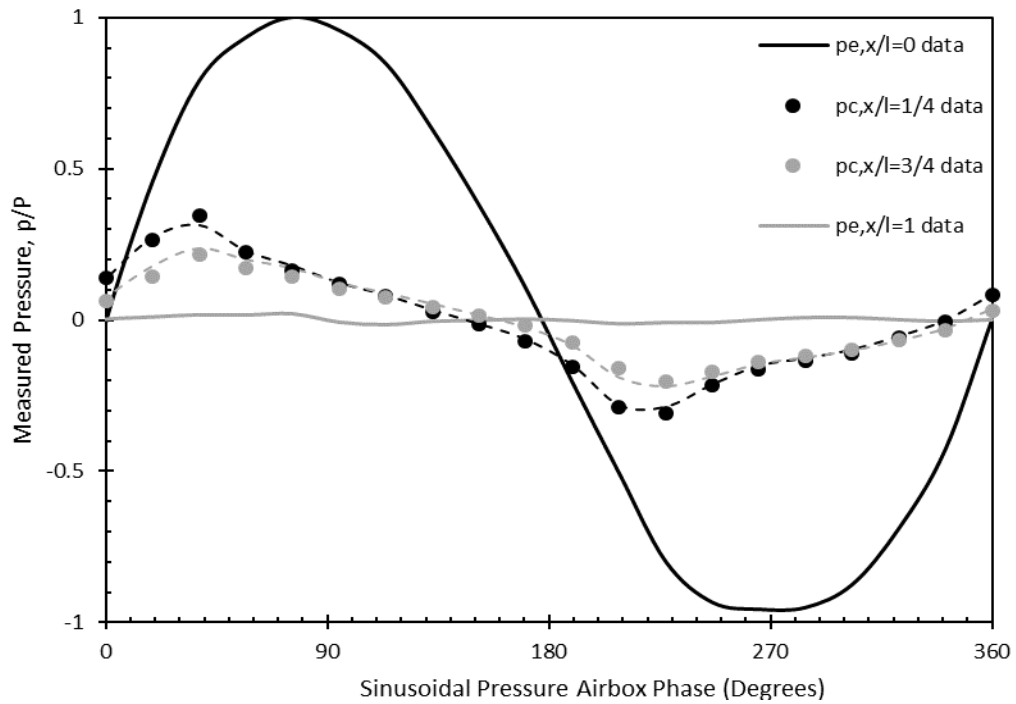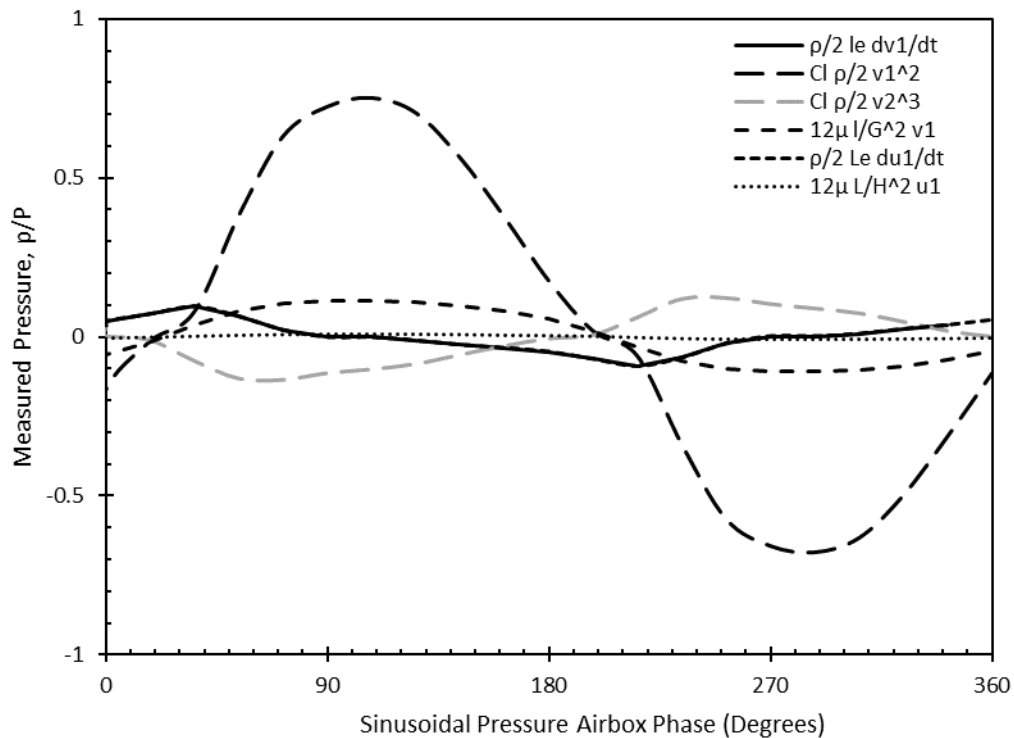l=160mm, G=2.44mm, and H=9.46mm scenario
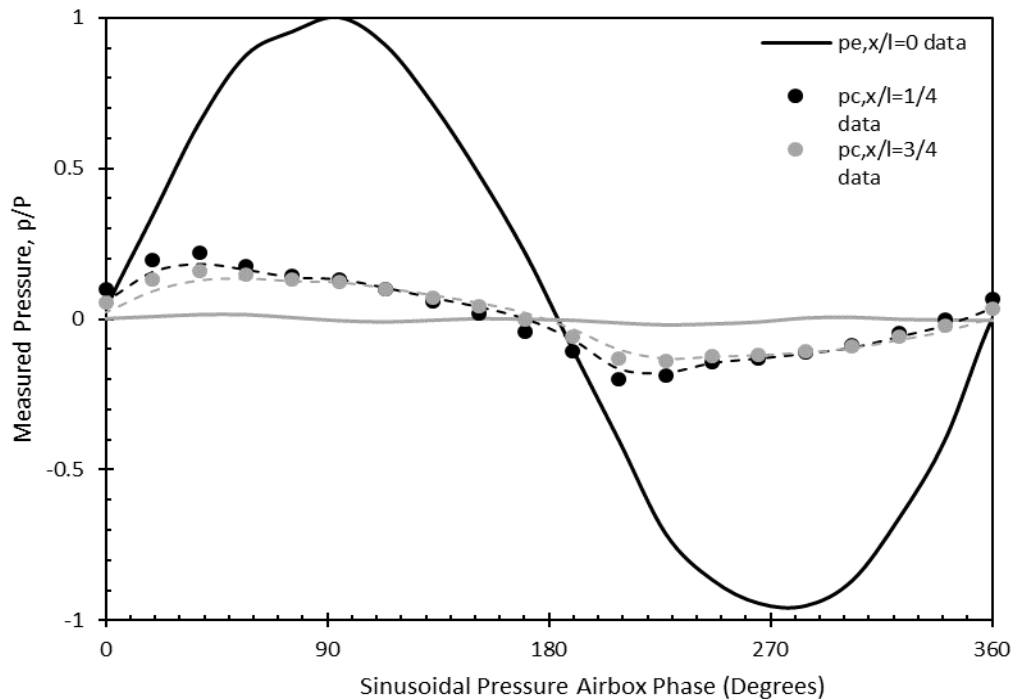
Figure 69: Measured and predicted pressures for Airbox#3, unsteady 5Hz pressure trace,
l=160mm, G=2.44mm, and H=9.46mm scenario
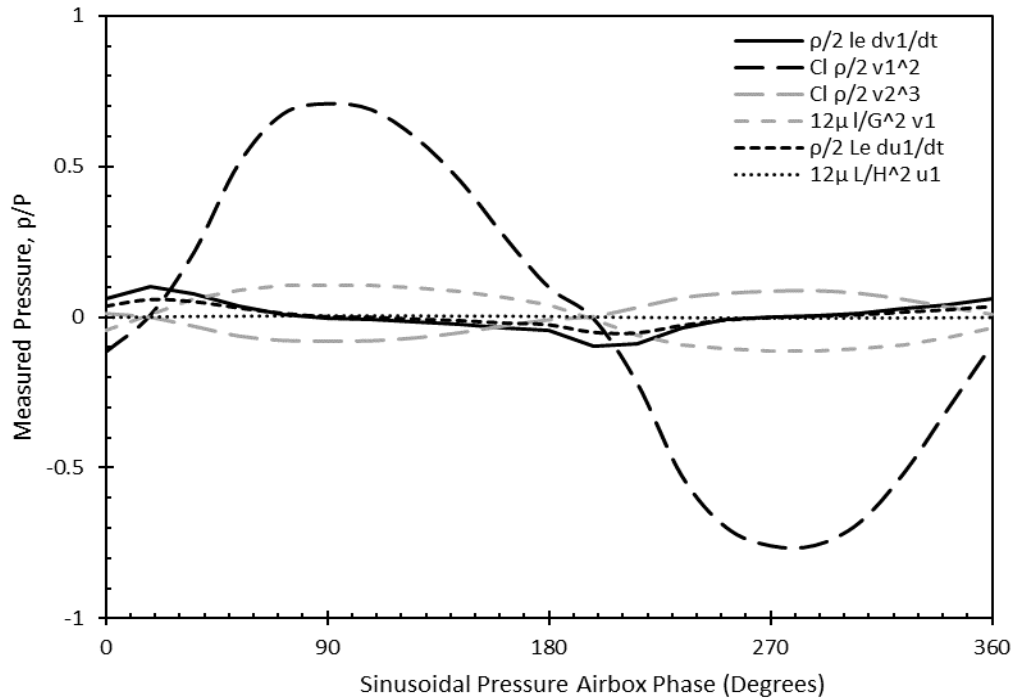
Figure 70: Predicted model loss and inertial terms for Airbox#2, unsteady 5Hz pressure trace, l=160mm, G=2.44mm, and H=9.46mm scenario

3.4 Closure

A simplified cladding system was setup and tested to verify the MDE model for ventilated cladding pressure equalization under high frequency varying pressures. For the setup with a much higher orifice than cavity flow resistance (deep cavity case) the MDE accurately (within +/-5%) predicted the cavity pressures under steady and unsteady flow. For the setup with similar orifice to cavity flow resistance the model does not accurately predict cavity pressures. This appears to be due significant effects of airflow turning into a perpendicular cavity. It was speculated that the flow between the orifice and the deep cavity is less constrained and hence act more as orifices to open spaces than for the shallow cavity. Cavity friction losses were found to generally be between those predicted for laminar and turbulent flow. Friction factors are speculated to follow above that for laminar flow due to flow development.

It was shown in Chapter #2 that vinyl siding has air flow resistance characteristics similar to the deep cavity case tested in this chapter. As the MDE model accurately predicted the

performance of this simplified system it seems that the Richardson annulus doesn't have a significant effect, use of fully developed laminar flow cavity model is adequate, and use of sharp edged orifice model accurately predicted orifice losses for this arrangement. Furthermore, the model may be accurate for vinyl given that other variables (flexibility of layers, sheathing air tightness, etc.) have minimal effects on performance.

Chapter 4

4 Analysis of a Full-Scale Wind Tunnel Dataset

The potential limitation of the MDE model for predicting pressure equalization effects on vinyl siding under high wind conditions were identified in chapter 2. It chapter 3 the model was found to accurately predict cavity pressures, hence pressure equalization, for a setup with a relatively high orifice flow resistance to the resistance within a relatively deep cavity. However, the tested cladding included several simplifications relative to vinyl siding.

In this chapter, measurements from full-scale wind tunnel testing of vinyl siding clad walls are analyzed. Datasets from these measurements were provided by the Institute for Business and Home Safety's (IBHS) facility (Cope et al. 2012). The implications of variations in sheathing air tightness and sheathing flexibility, which were not examined in Chapter 3, are examined through dataset analysis from additional measurements taken as part of this thesis study. The data is further compared to an MDE model adapted for vinyl siding. Finally, physical modifications to vinyl siding necessary for such systems to achieve the pressure equalization allowed in ASTM D3679.

4.1 Full-Scale Wind Tunnel Test Summary

The IBHS study walls were batt-filled, wood-frame construction clad with vinyl siding and sheathed with rigid Foam Board (FB) or Oriented Strand Board (OSB). A sketch of the wall assembly and pressure tap locations through the depth of the assembly are shown in plan and section view in Figure 71 and Figure 72.
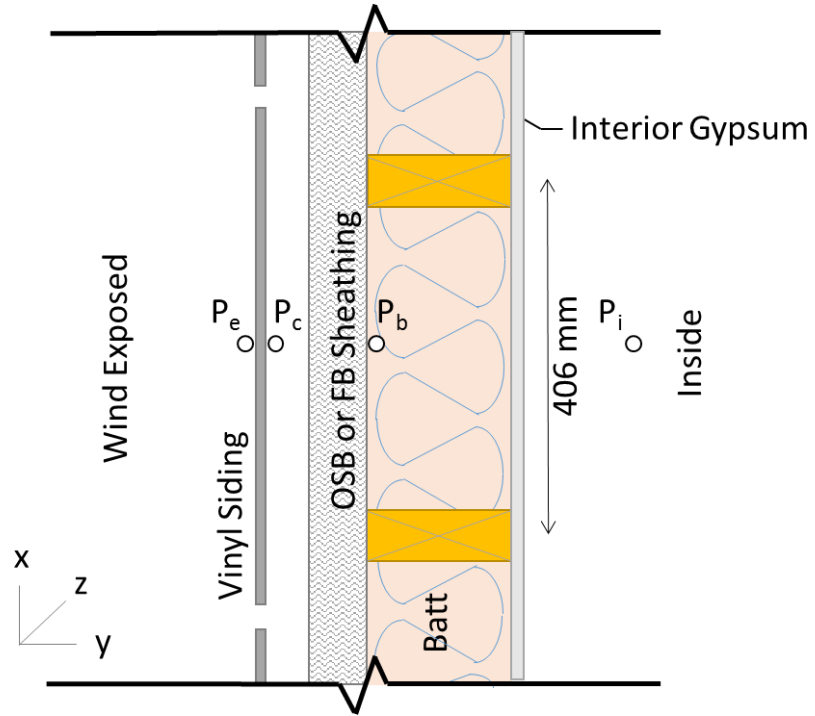
Figure 71: Pressure measurements in exterior wall system (plan view)
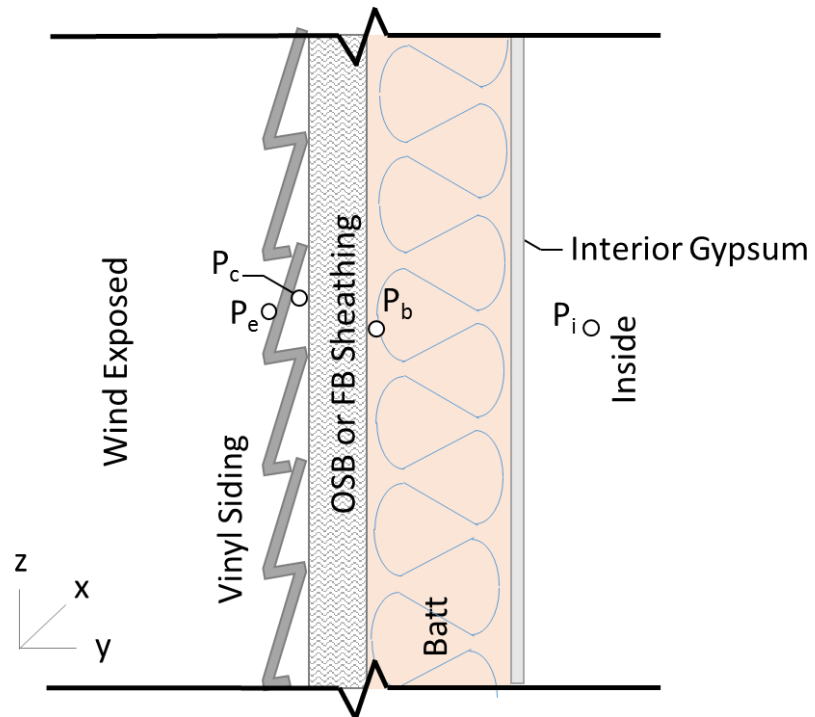
Figure 72: Pressure measurements in exterior wall system (section view)
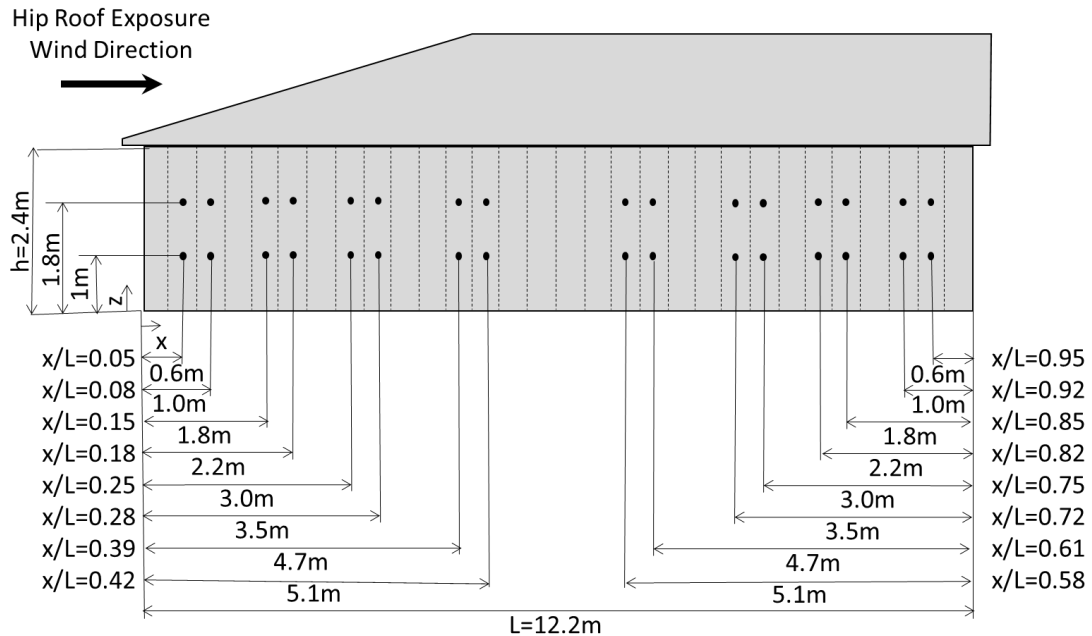
Figure 73: Schematic drawing showing the hip and gable roof configurations and the pressure taps location (labelling shown for wind from hip roof direction)

The test walls were installed on a simple rectangular 9.2m by 12.2m exterior floor plate test building with a hip and gable roof exposure at either end, as shown in Figure 73. The wood framing members (e.g., 2x4 studs) sit at 406mm on centre (16 inches on centre) and are shown as vertical dashed lines on the wall in the figure. The test building was constructed on a rotatable table to allow exposure at various wind angles.

The tests were run at a series wind angles and at several wind speeds for 15 minutes time increments. Pressure transducer voltage measurements were taken at 1000HZ and filtered to 100 Hz for analysis. The pressure taps were located along upper and lower bands running the length of the wall at approximately 1m and 1.8m from the ground as shown in Figure 73. The pressure tap nomenclature is indicated in Figure 73 for the hip roof windward exposure case and labelled for the relative distance across the length of the wall, x/L. For gable roof exposures, the ratios are reversed so that the x/L=0 position is always the windward edge of the wall. The two horizontal bands of measurements will further be referred to by their location relative to the eave height, h, being y/h=0.4 and 0.75.

Wind speed readings were simultaneously recorded by an upstream anemometer. The measured mean and gusting wind speeds are listed in Table 2. Mean wind speed for the 2.44m (8ft) roof height, $\overline{U}_W$, listed in Table 2 were calculated from the lab wind speed measured with an anemometer at 4.9m (16ft), using ESDU85 z_o=0.01m (from Morrison et. al. 2012) assuming open terrain condition (ASCE 7-10, 2010) as follows:

$$\overline{U}_W = \overline{U}(y = 4.9\text{m}) \cdot \left(\frac{2.44\text{m}}{4.9\text{m}}\right)^{0.14} \tag{81}$$

Table 2: Test Scenarios for Datasets Analyzed from Full-Scale Wind Tunnel Test

Gusting Wind Speed (m/s)	20	20	27	27	35	35
Wind Directions Analyzed	0°	180°	0°	180°	0°	180°
Mean Wind Speed	14.7	14.5	20.2	19.6	27.9	26.6
Calculated, $\overline{U}_W$(m/s)	13.2	13.1	18.2	17.6	25.1	23.9

Wind perpendicular to the 12.2m walls from the hip roof and gable roof windward exposures were determined by Cope et al. (2012) to produce the peak negative (design) pressures on the test walls and are the only two exposures used in this study. First, the measurements were further analyzed to assess spatial variations. Spatial variations in performance provide flow behaviour insights and allow examination of experimental issues. The MDE analytical model described in Chapter 3 is then applied to the tested wall system and compared to the measurements. The model is then further used to determined adjustments to the airflow characteristics necessary to improve pressure equalization performance.

4.2 Measured Wind Pressure Coefficients and Pressure Equalization Factors

The mean and root mean square (RMS) pressures coefficients have been calculated at different pressure tap locations on the wall as follows:

$$\overline{C}_{p,e} = (p_b - p_i)_{mean}/(0.5\rho\overline{U}_W^2) \tag{82}$$

$$\tilde{C}_{p,e} = (p_e - p_i)_{RMS}/(0.5\rho\overline{U}_W^2) \tag{83}$$

$$\overline{C}_{p,c} = (p_b - p_i)_{mean}/(0.5\rho\overline{U}_W^2) \tag{84}$$

$$\tilde{C}_{p,c} = (p_c - p_i)_{RMS}/(0.5\rho\bar{U}_W^2) \tag{85}$$

$$\bar{C}_{p,b} = (p_b - p_i)_{mean}/(0.5\rho\bar{U}_W^2) \tag{86}$$

$$\tilde{C}_{p,b} = (p_b - p_i)_{RMS}/(0.5\rho\bar{U}_W^2) \tag{87}$$

where p is pressure and $\bar{C}_p$ and $\tilde{C}_p$ are the mean and RMS pressure coefficients, respectively. The subscripts e, c, b, and i refer to the external surface, cavity space, batt space, and indoor pressure tap locations, respectively, ρ is density, assumed to be 1.15 kg/m^3, and $\bar{U}_W^2$ is the square of the mean wind speed adjusted to roof height, as given in Table 2.

Plots of measured mean and RMS pressure coefficients for the cladding surface, air cavity, and batt space pressure taps for a range of wind speeds for both hip and gable roof assemblies along the lower band (y/h=0.4) of the OSB sheathed wall are given in Figure 74, Figure 75 and Figure 76. The average of these values for the range of wind speeds is also shown as dashed lines for hip and gable roof exposures, to highlight the trends.

The results show high mean exterior pressures toward the wind ward edge of the wall and high RMS pressures along the leading half of the wall. This is consistent with typical wind tunnel observations (e.g., Davenport 1977) where flow separates at the windward wall edge and reattaches along the wall forming a separation bubble which in this case appears to reach as far as half way along the wall. The mean pressure coefficients peaks between x/L = 0.2 and 0.3 and these peak coefficients are slightly higher for lower wind speeds. The pressures are lower for the hip roof than the gable roof exposure. The pressure coefficients all decline from the surface to the cavity to the batt space.
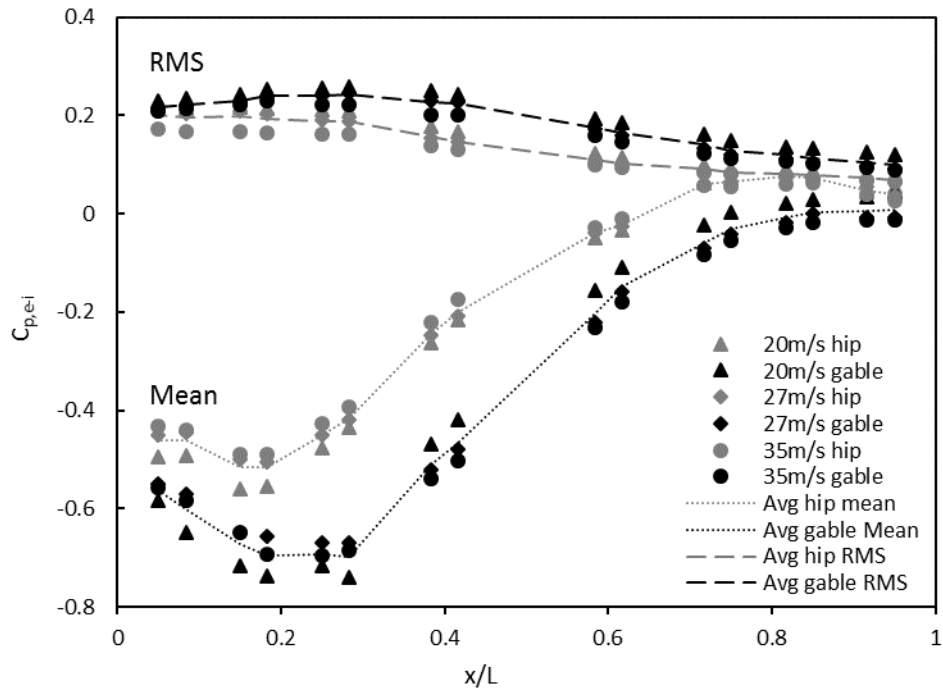
Figure 74: Mean and RMS surface pressures along length of OSB walls at 0.4z/h for wind normal to wall
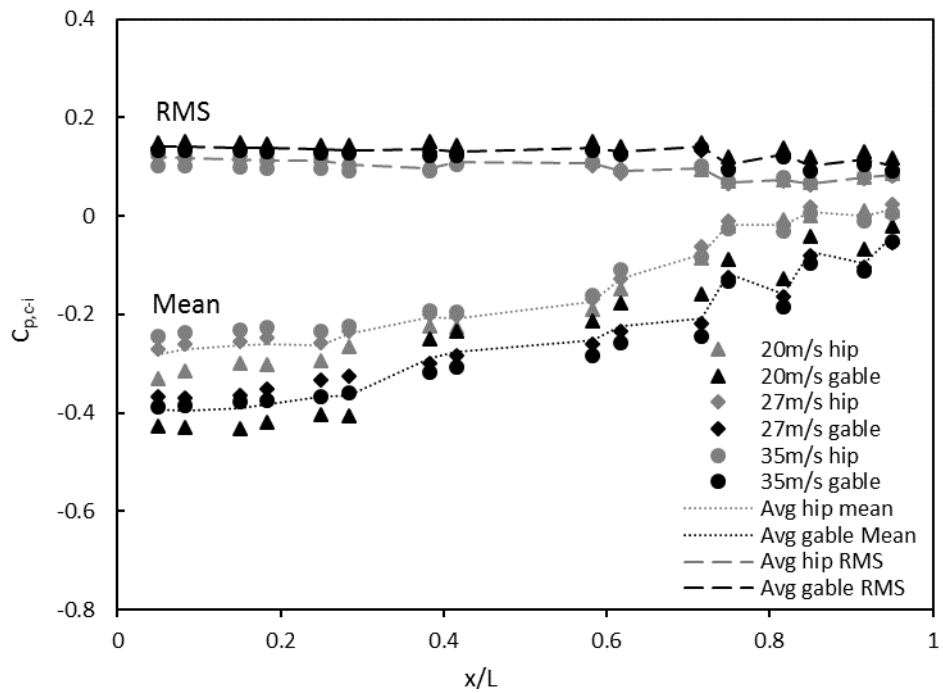
Figure 75: Mean and RMS cavity pressures along length of OSB walls at 0.4z/h for wind normal to wall
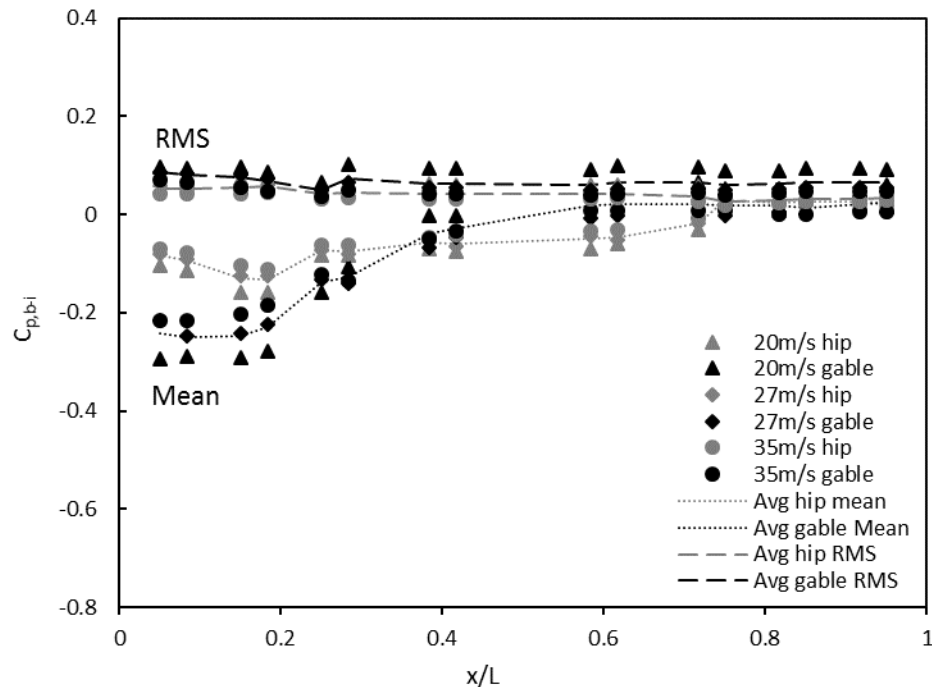
Figure 76: Mean and RMS batt pressures along length of OSB walls at 0.4y/h for wind normal to wall

Plots of mean and RMS pressure coefficients for the cladding surface, air cavity, and batt space pressure taps for both the OSB and FB sheathed walls along the lower (y/W=0.4) and upper (y/W=0.75) bands for hip and gable roof exposures are given in Figure 77, Figure 78, and Figure 79 for the 35m/s gusting wind case.

Measurements pressures along the upper and lower band of pressure taps were similar. Differences would have been expected if measurements were taken closer to the bottom or top of the wall (Straube 1999). The OSB sheathed walls saw 0.1 greater mean pressure coefficients than the FB wall between x/L=0.1 and 0.3 which appears to translate into higher cavity and batt pressures. The sheathing choice should not affect surface pressures suggesting this is a results of measurement uncertainty.
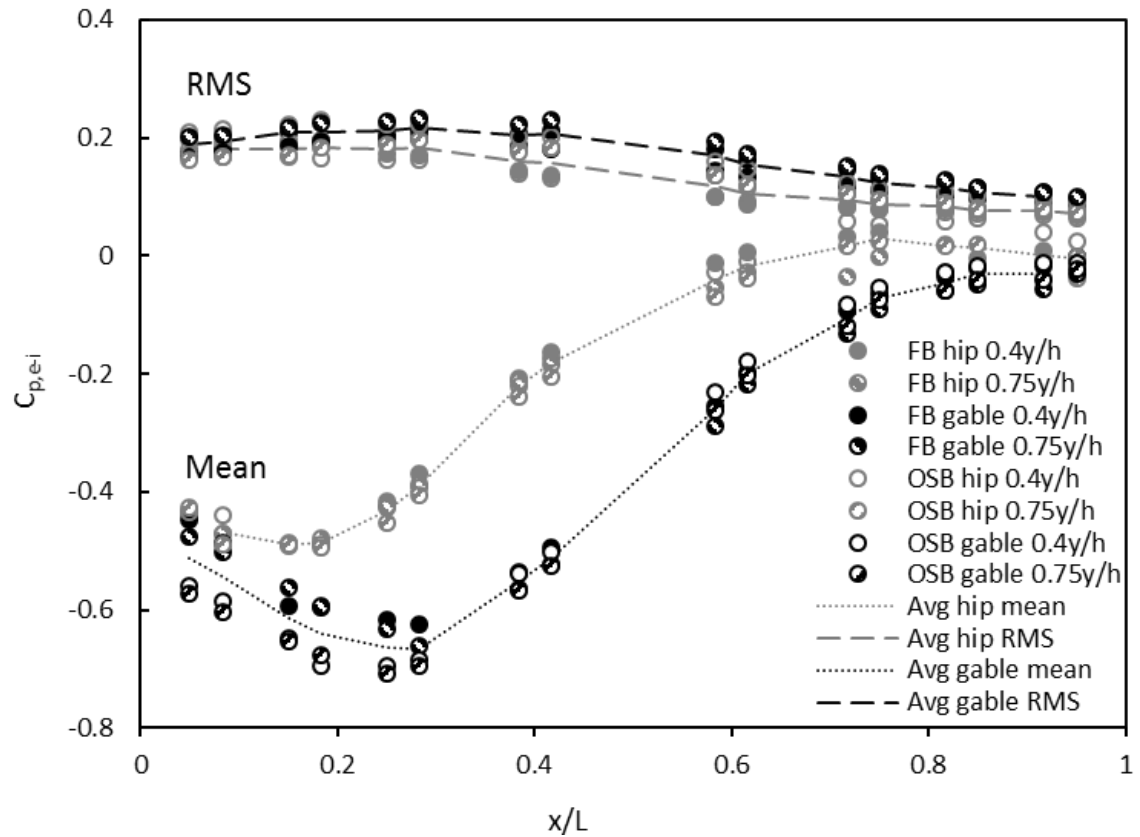
Figure 77: Mean and RMS surface pressures for 35 m/s wind speed normal to wall

The finding suggests limited difference in the pressure equalization of these two systems even though there are potentially differences in the airtightness and flexibility of these products. This finding supports those model assumptions used in Chapter 3.
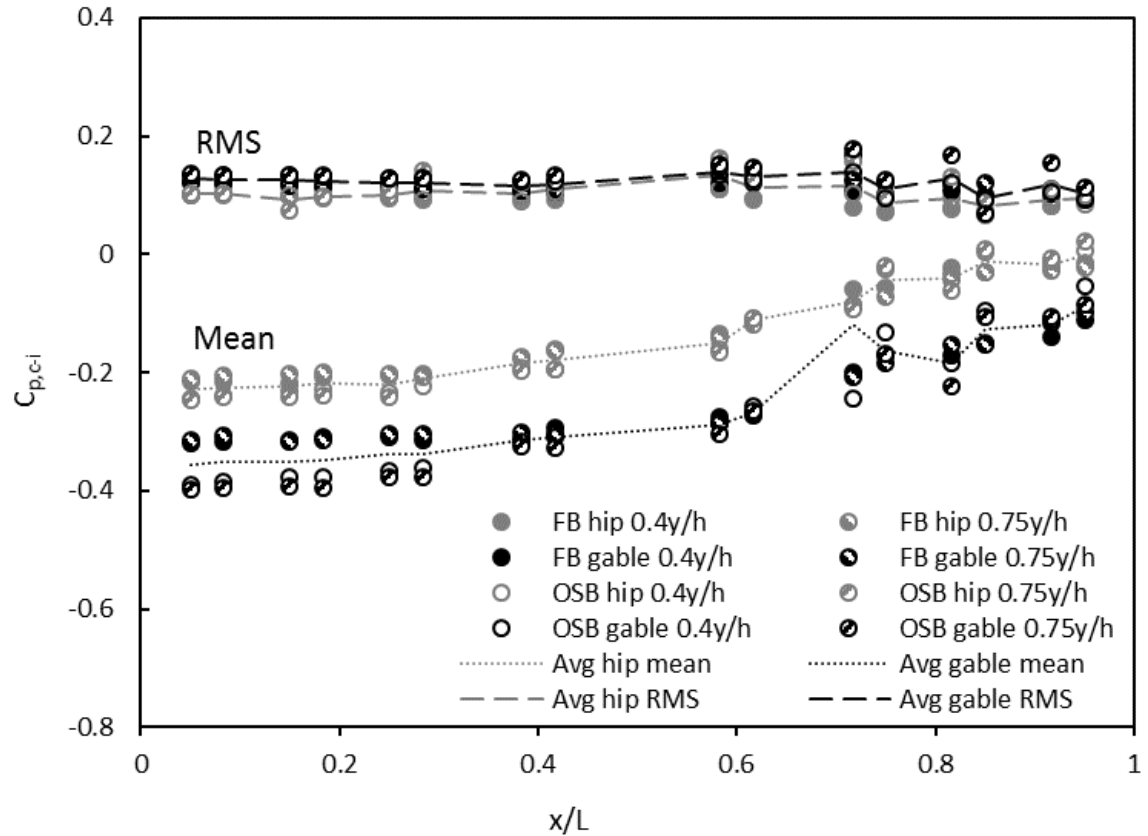
Figure 78: Mean and RMS cavity pressures for 35 m/s wind speed normal to wall

The batt pressure coefficients for the FB wall gable exposures at both upper and lower bands between 0.2 x/W and 0.6 x/W are high and comparable to cavity pressure coefficients in the same location. It is possible that a large isolated sheathing air leakage pathway existed through the sheathing in this area. This would affect upper and lower bands of pressure taps as they sit in the same batt space. The potential for variations in sheathing airtightness in this test is explored later in this chapter.
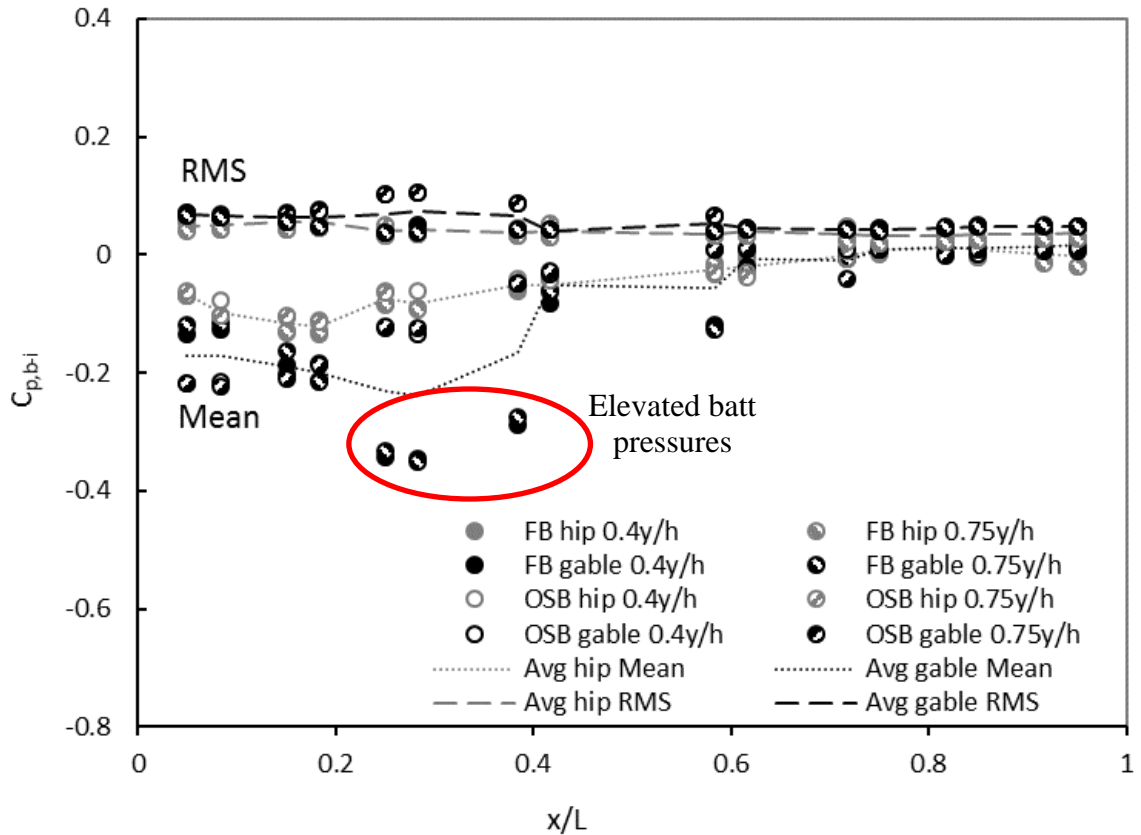
Figure 79: Mean and RMS batt pressures for 35 m/s gusting wind speed normal to wall

To assess peak loading, the measurements were plotted in terms of instantaneous PEF values calculated per equation (4). These values are plotted for the pressure tap locations within the windward half of the wall along the lower band of the FB wall for the hip and gable exposures in Figure 80 and Figure 81. The locations of the pressure taps are also shown in the plots. The 90th percentile of the PEF values are plotted as a dashed line in the plots to estimate possible design values. Following the 90th percentile lines left toward the y-axis, both graphs show PEF converging to approximately 0.8 PEF. The highest wind loads occurred within 0.25 x/L of the windward leading edge of the wall matching the location of the highest mean suction pressures. The highest pressures for the hip roof occurred closer to the wind-ward edge than for the gable roofs which also matches the mean pressure coefficient findings.
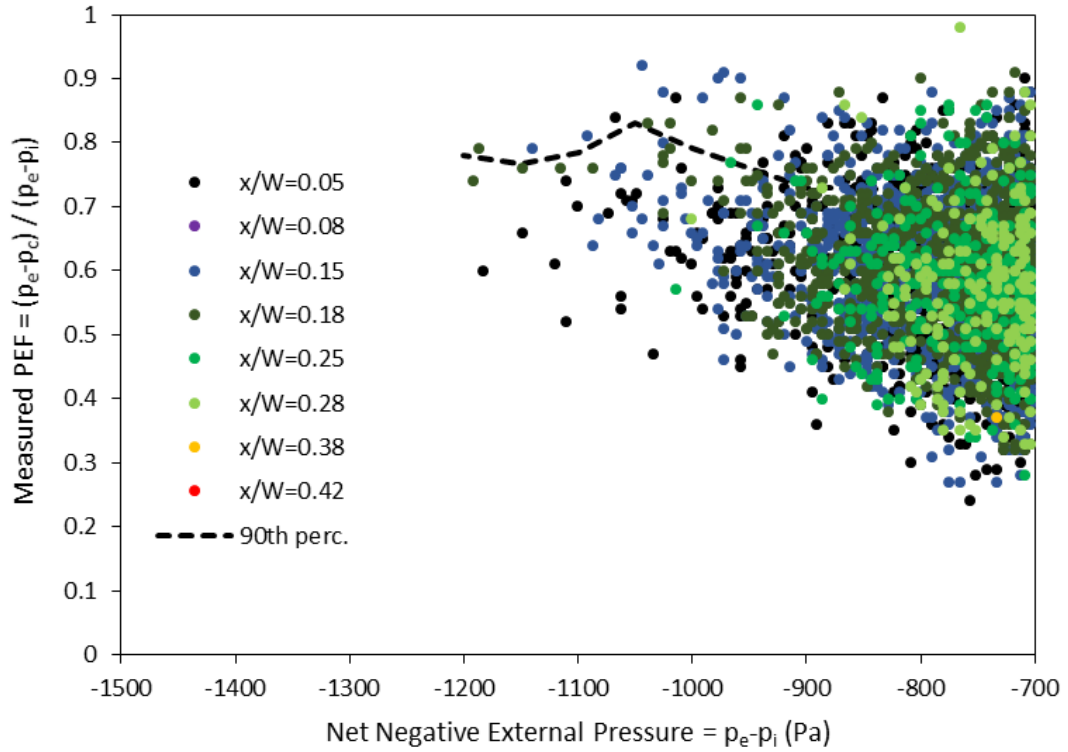
Figure 80: External pressure vs. PEF for hip roof 35 m/s wind speed normal to wall
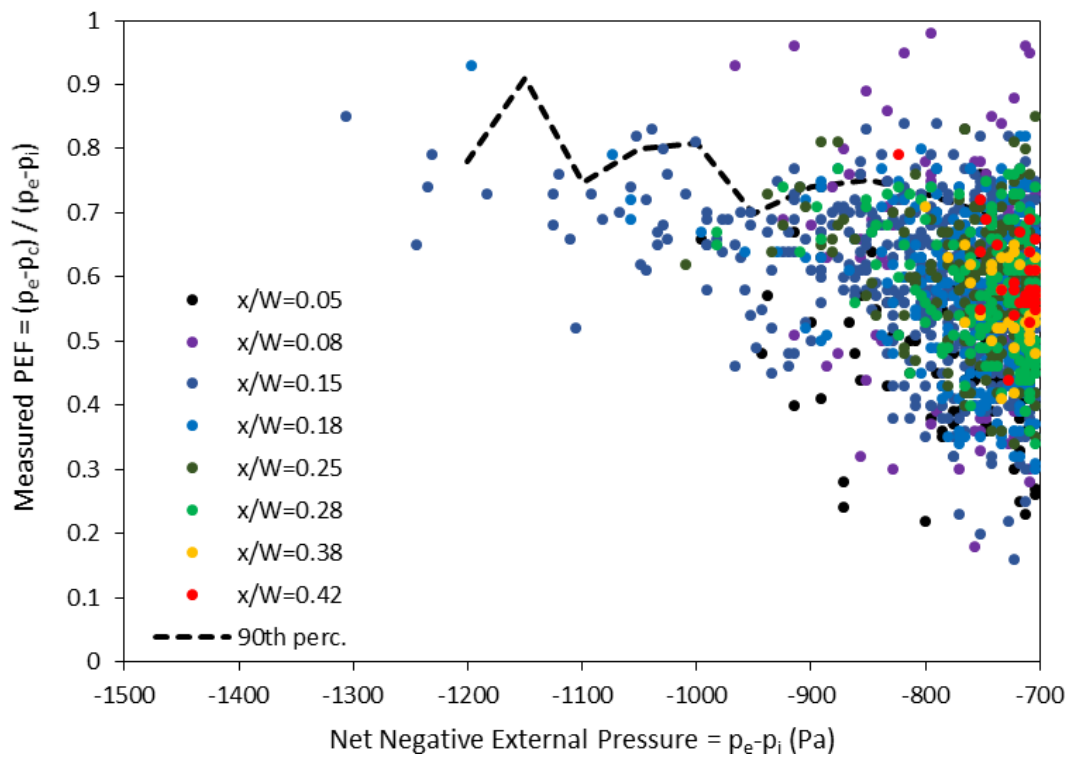
Figure 81: External pressure vs. PEF for gable roof 35 m/s wind speed normal to wall

4.3   Sheathing Air Leakage Investigation

An isolated case of batt space pressures following cavity pressures are described in section 4.2 suggesting variations in sheathing air leakage amongst the test walls. This is important because the MDE equation based model ignores sheathing air leakage. The air tightness of walls installed in the IBHS test house from a subsequent study at IBHS (Morrison and Cope (2015)) were used for the investigation and based on the assumption that construction variance would be similar to the previous Cope et al. (2012) study.

The variation in air tightness was measured by drawing air from an airbox mounted over electrical outlets (with their covers removed) at a range of airbox suction pressures. The air from the airbox was drawn through a rotameter for airflow rate measurement by a vacuum. The pressure difference between the airbox and the test house interior was measured with a manometer. The test was run during still exterior conditions and the test house door was left open to allow the interior and exterior pressure to equalize. A drawing of the wall assembly with the air leakage apparatus installed is given in Figure 82. Photos of this apparatus are given in Figure 83 and Figure 84. The Figure 82 drawing also shows possible air leakage paths (light blue lines) through the wall assembly some through the sheathing and others through other paths. Unfortunately, the walls were installed in such a way that direct measurement of the sheathing airtightness was not possible. In future studies test walls could be installed with air tight perimeters to allow air tightness measurement.

The measured air leakage flowrates are plotted in Figure 85. Power law curve fits, using the method of least squares, for pressure versus flow rate set of measurement are also given on the graph. The measurements show a factor of two variation in air leakage for different measurement locations. Power law exponents for the various outlets ranged from 0.5 to 0.8. It was noted in Chapter 2 that sharp-edged orifices have a power law exponent of 0.5 while long narrow and tortuous orifices have an exponent of 1.0. Hence, this result suggest variation in the types of air leakage paths as well. The measured variations provide evidence that the batt space pressure anomaly could be due to variance in sheathing air tightness.
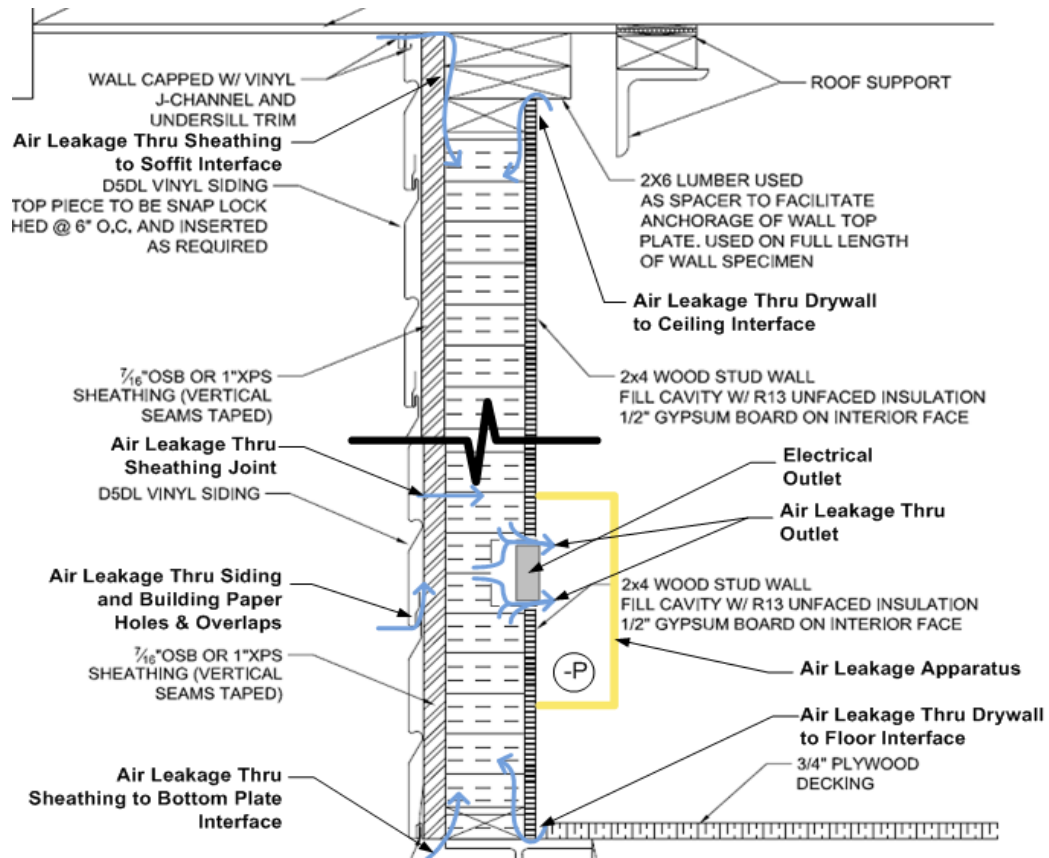
Figure 82: Air Leakage Paths during Testing

Figure 83: Typical electrical outlet with cover removed and ready for airbox mounting

Figure 84: Photo of airbox mounted over electrical outlet and ready for testing.
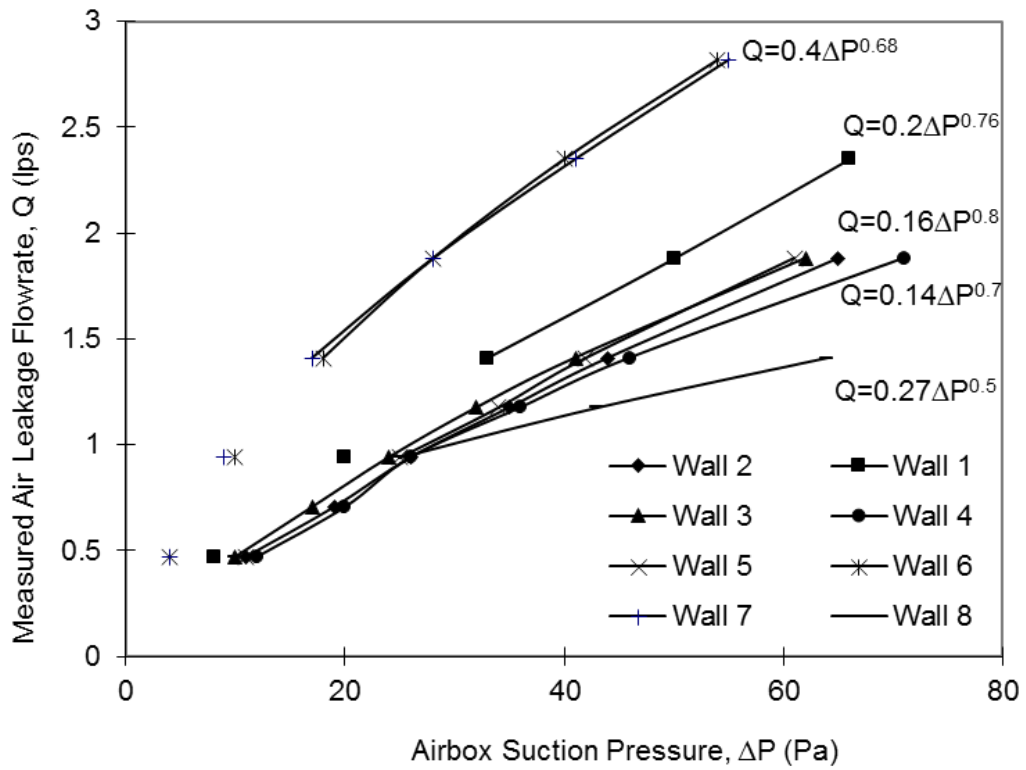
Figure 85: Measured air leakage flowrate through electrical outlets without covers at a range of airbox suction pressures and power law curve fits

4.4 Analytical Modelling

The Oh and Kopp (2014) model is adapted in this chapter to the testing described in section 4.2. The main objective of this analysis is to determine if the model can accurately predict pressure equalization effects given the assumptions and simplification in the model which are similar to those used in Chapter 3. An illustration of hypothetical wind driven airflow through and behind vinyl siding is shown in Figure 86. Spatial variations in surface pressures are expected to drive air through the siding at various vent locations. Air mostly flows horizontally due to the low horizontal flow resistance within the cavities formed by the siding profile. The length of this flow path is not clearly defined as some portion of the cavity air mixes with exterior air at the various opening along the length.   Vertical airflow behind the siding is minimized as the siding rests against the sheathing.
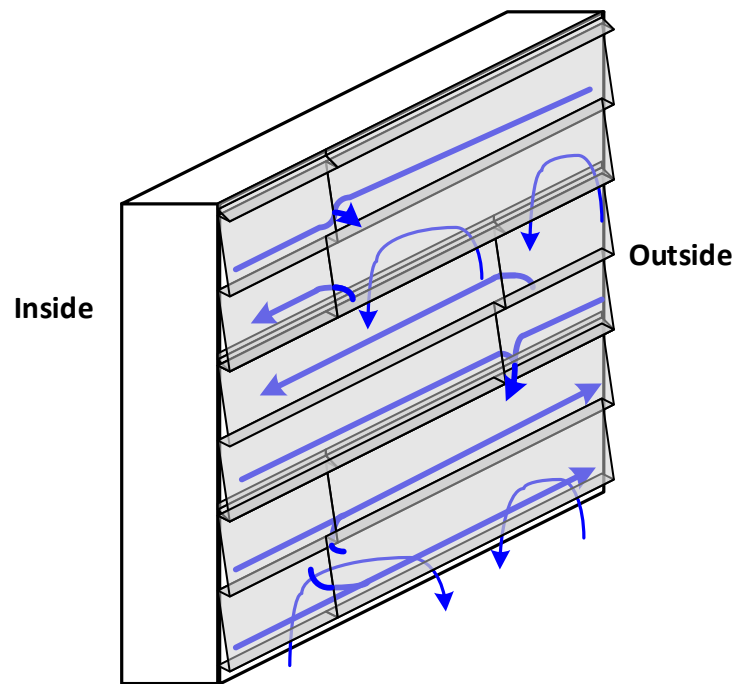
Figure 86: Illustration of realistic air flow through vinyl siding during wind exposure

1. Wide rectangular cavities with constant depth, H.

2. No airflow between adjacent cavities.

3. Vertical orifice openings with constant loss coefficients of 2.5 and no wall friction losses

4. Airtight sheathing

5. Rigid sheathing and cladding

6. Vent locations align with pressure taps from which exterior pressures are drawn

7. Fully developed laminar cavity flow
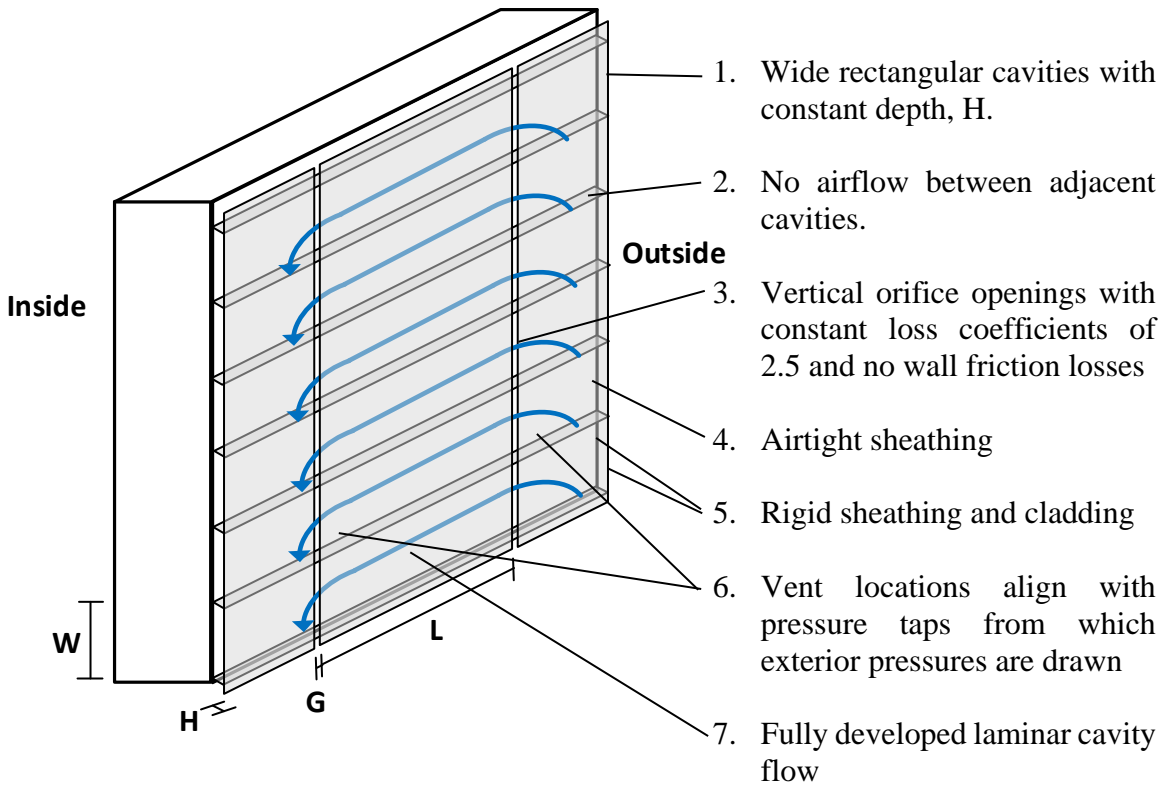
Figure 87: Illustration of simplified airflow and geometry assumed in model

The MDE model was used for the vinyl siding by making several assumptions as illustrated and listed in Figure 87. The flow network has flow resistance components through the siding and in the cavity between the orifice openings as shown in Figure 88.
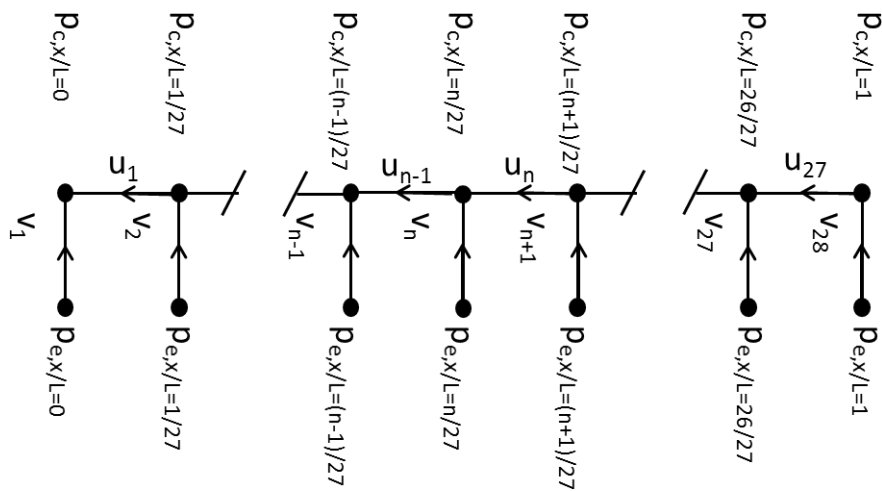
Figure 88: Nodal network for airflow model

Airflow velocity through the orifices, v_n, is driven by the pressure difference between the surface pressures, $p_{e,x/L=n}$, and cavity pressures, $p_{c,x/L=n}$. The air flow velocity through the cavity, u_n, is driven by the pressure difference between the adjacent cavity pressures, $p_{e,x/L=n}$, and cavity pressure $p_{e,x/L=n-1}$. These are calculated with a time step, dt, of 0.01s matching the IBHS dataset.

To capture unsteady affects, the equations are solved iteratively. The methodology and calculations used are as follows.

1. Initially set $u_{i,old}(t) = u_i(t-1)$

2. Calculate $v_i(t)$ based on $u_{i,old}(t)$, values using conservation of mass

$$v_1(t) = u_{1,old}(t) \cdot H/G \tag{88}$$

$$v_2(t) = [u_{2,old}(t) - u_{1,old}(t)] \cdot H/G \tag{89}$$

...

$$v_{28}(t) = u_{27,old}(t) \cdot H/G \tag{90}$$

3. Calculate $p_c(t)$ based on $v(t)$ and $p_e(t)$ using Oh and Kopp (2014)

$$p_{c,x=0}(t) = p_{e,x=0}(t) - \frac{\rho l_e[3v_1(t)-4v_1(t-1)+v_1(t-2)]}{2dt} - \frac{C_L\rho}{2}v_1(t)|v_1(t)| - \frac{12\mu l_o}{G^2}v_1(t) \tag{91}$$

...

$$p_{c,x=L}(t) = p_{e,x=L}(t) - \frac{\rho l_e[3v_{28}(t)-4v_{28}(t-1)+v_{28}(t-2)]}{2dt} - \frac{C_L\rho}{2}v_{28}(t)|v_{28}(t)| - \frac{12\mu l_o}{G^2}v_{28}(t)$$
$$\tag{92}$$

4. Calculate $u_{i,new}(t)$ based on $p_c(t)$ values using Oh and Kopp (2014)

$$\rho L_m \frac{3u_1(t)-4u_1(t-1)+u_1(t-2)}{2dt} + \frac{12\mu L_m}{H^2}u_1(t) = p_{c,x/L=0}(t) - p_{c,x/L=1/27}(t) \tag{93}$$

Solving for $u(t)$

$$u_1(t) = \frac{p_{c,x/L=0}(t) - p_{c,x/L=1/27}(t) + 4\rho L_m/2dt \cdot u_1(t-1) - \rho L_m/2dt \cdot u_1(t-2)}{3\rho L_m/2dt + 12\mu\rho L_m/H^2} \tag{94}$$

…

$$u_{27}(t) = \frac{p_{c,x/L=26/27}(t) - p_{c,x/L=1}(t) + 4\rho L_m/2dt \cdot u_{27}(t-1) - \rho L_m/2dt \cdot u_{27}(t-2)}{3\rho L_m/2dt + 12\mu\rho L_m/H^2} \qquad (95)$$

5. Estimate $u_i(t) = 0.5u_{i,new}(t) + 0.5u_{i,old}(t)$

6. Exit loop and move to next time increment when $u_i(t) = u_{i,old}(t)$ (RMS of all points within 1%)

7. Otherwise set $u_{i,old}(t) = u_i(t)$ and return to step 2.

Geometric inputs were based on measurements from a previous study (Van Straaten 2004) and listed in Table 3. A 10mm cavity depth was used and assumed to capture conditions under high suction pressures. A gap length of 1mm was used as an approximate average length of orifice through the vinyl siding. A model cavity length of 406mm was used, since this is the minimum distance between pressure taps used as inputs for the analysis. The model gap orifice width is calculated based on model cavity length and open area of 0.12%. Equation (24) can be used for effective gap slug length since the cavity depths are deep relative to the gap widths.

Table 3: Model Input for Full-Scale Wind Tunnel Test Vinyl Siding Clad Walls

Open Area, O	Cavity Depth, H	Cavity Length, L_m	Orifice Width, $G = L_m *O$	G/H	Orifice Length, l_o	Effective Gap Slug Length $l_e = l_o + 0.89G$
0.12%	10mm	406mm	0.4mm	0.4/10	1mm	1.4mm

The model was run for both the hip and gable roof exposures for the lower-band FB wall. The model results are compared to measurements for the various wind speeds given in Figure 89 through Figure 94. The uncertainty of pressure measurements were not reported by Cope et. al. (2012). Mean and root mean square (RMS) pressure coefficients are shown on each graph. Except for an anomaly at x/L=0.08 for the hip roof, the model predicts the measured mean cavity pressure coefficients within +/-0.08 (or 20% of the greatest mean pressure coefficients) along the windward half of the wall where design wind loads are expected. RMS pressure coefficients are predicted within +/-0.01.

Figure 89: 20m/s, hip roof, FB sheathing predicted and measured coefficients

Figure 90: 20m/s, gable roof, FB sheathed predicted and measured coefficients

Figure 91: 27m/s, hip roof, FB sheathed predicted and measured coefficients
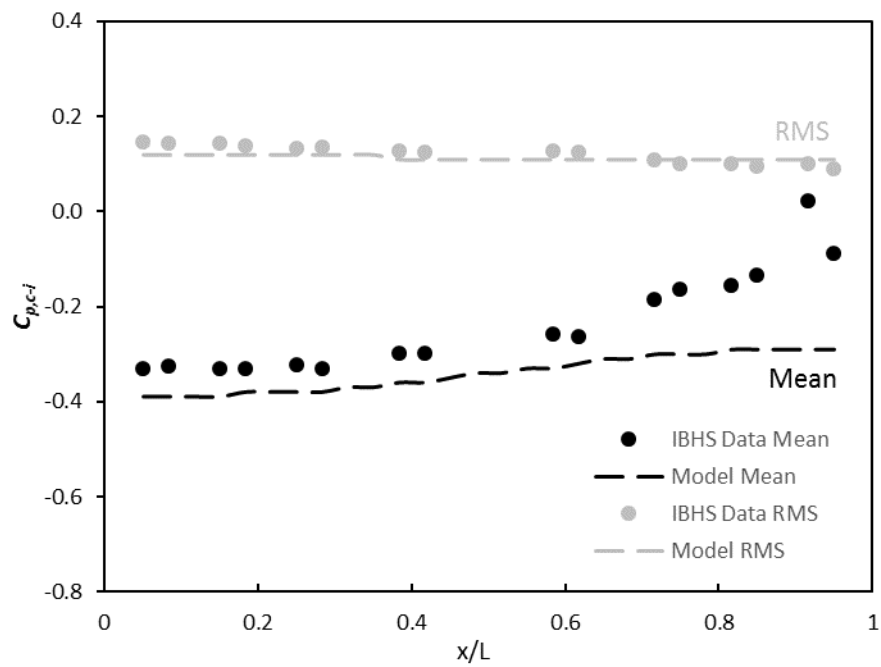
Figure 92: 27m/s, gable roof, FB sheathed predicted and measured coefficients
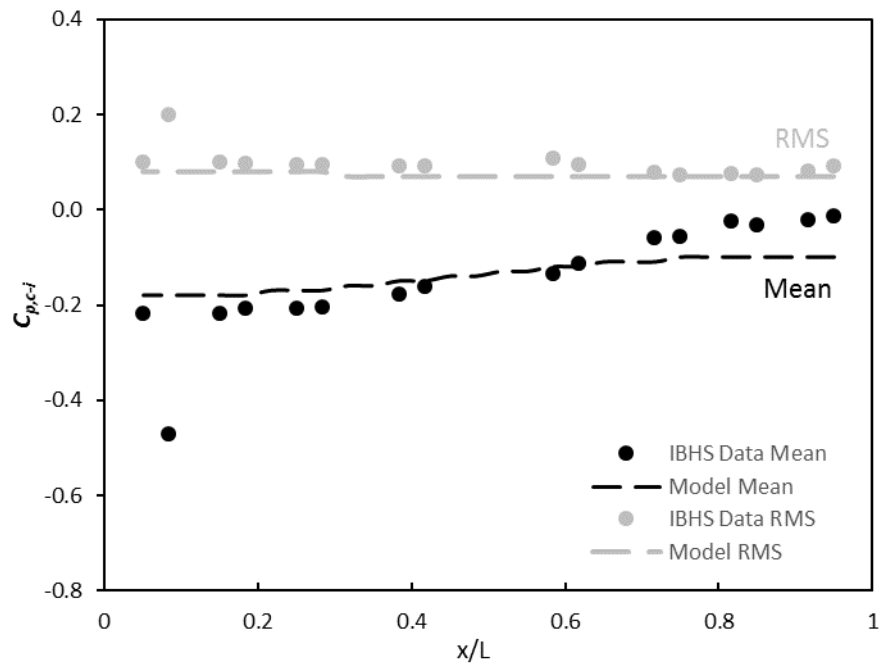
Figure 93: 35m/s, hip roof, FB sheathed predicted and measured coefficients
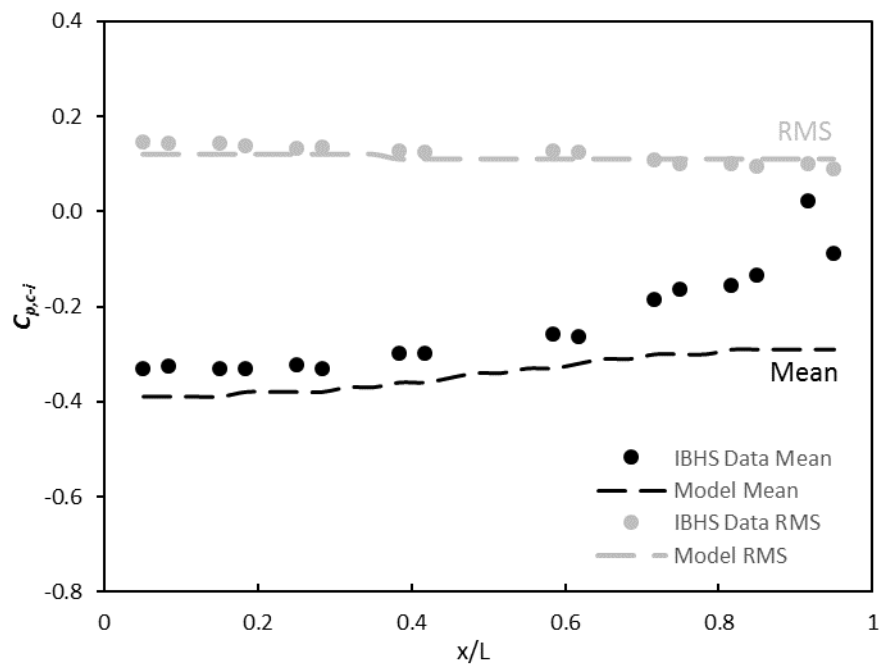
Figure 94: 35m/s, gable roof, FB sheathed predicted and measured coefficients

PEF values were calculated, as described in section 4.2. These are plotted for the high 35 m/s wind speed condition in Figure 95 and Figure 96 for the hip and gable roof exposures. The 90th percentile of all the PEF values is shown as a dashed line in the plots. These values show similar predictions as for the measured PEF values being in the range of 0.7 to 0.8. Hence, the analytical model accurately predicts pressure equalization performance for the tested vinyl siding.
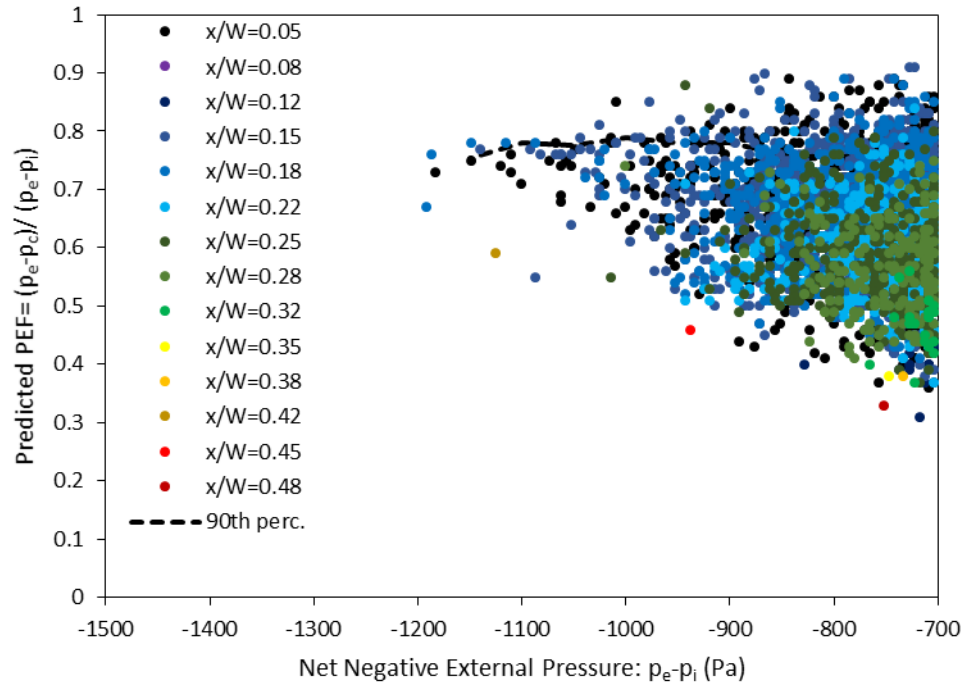
Figure 95: Predicted external pressure vs. PEF for hip roof, 35 m/s
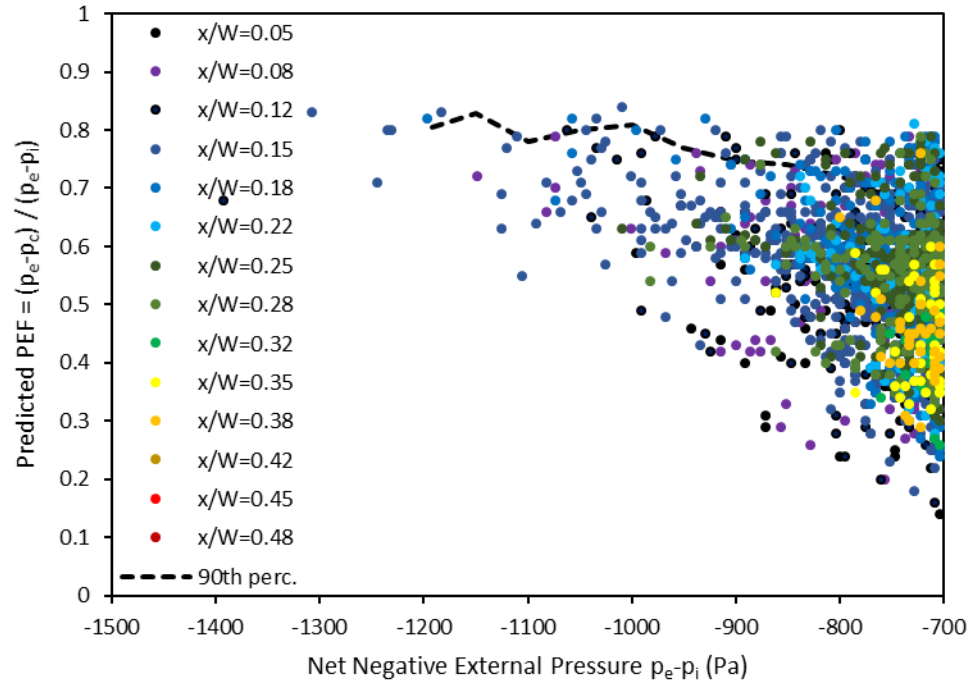
Figure 96: Predicted external pressure vs. PEF for gable roof, 35 m/s

4.5 Vinyl Siding Wall with Improved Pressure Equalization Performance

Given the accuracy of the model in predicting the measured pressure equalization performance for a simplified cladding system in Chapter 3 and actual vinyl siding cladding in the previous section, it was further used to determine how the airflow resistance characteristics would need to be altered to achieve high pressure equalization performance. Several cavity and gap width scenarios have been modelled as listed in Table 4. These include increasing gap width or open area by a factor to 0.5 and 1%, and then reducing the cavity depth to 4mm.

Table 4: Modelled Scenarios for Vinyl Siding Optimization

Open Area, O	Cavity Depth, H	Cavity Length, L_m	Orifice Width, $G = L_m * O$	G/H	Orifice Length, l_o	Effective Gap Slug Length $l_e = l_o + 0.89G$
0.5%	10mm	406mm	2mm	2/10	1mm	2.8mm
1%	10mm		4mm	4/10		4.5mm
1%	4mm		4mm	4/4		4.5mm

The results for these simulations for the various wind speeds are included in Figure 97 through Figure 102. Mean and root mean square (RMS) pressure prediction are shown on each graph as well as the original measurements and simulation of the IBHS test wall. Each step toward higher G/H ratios has an impact on mean and RMS cavity pressure coefficients. As these coefficients rise in magnitude, the cavity pressures more closely match the surface pressure and, hence, pressure equalization is improving. The G/H=2/10 model further matches the leeward half measurements closely for most cases while the G/H=0.4/10 model for section 4.4 most closely matches the windward half. It may be that the difference is capturing the difference in the vinyl siding as it is drawn outward.
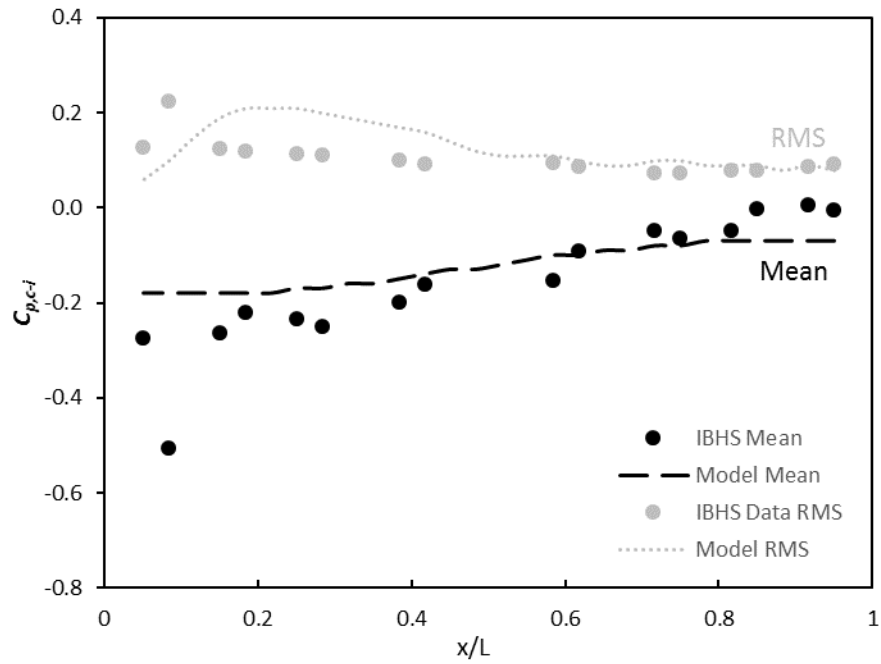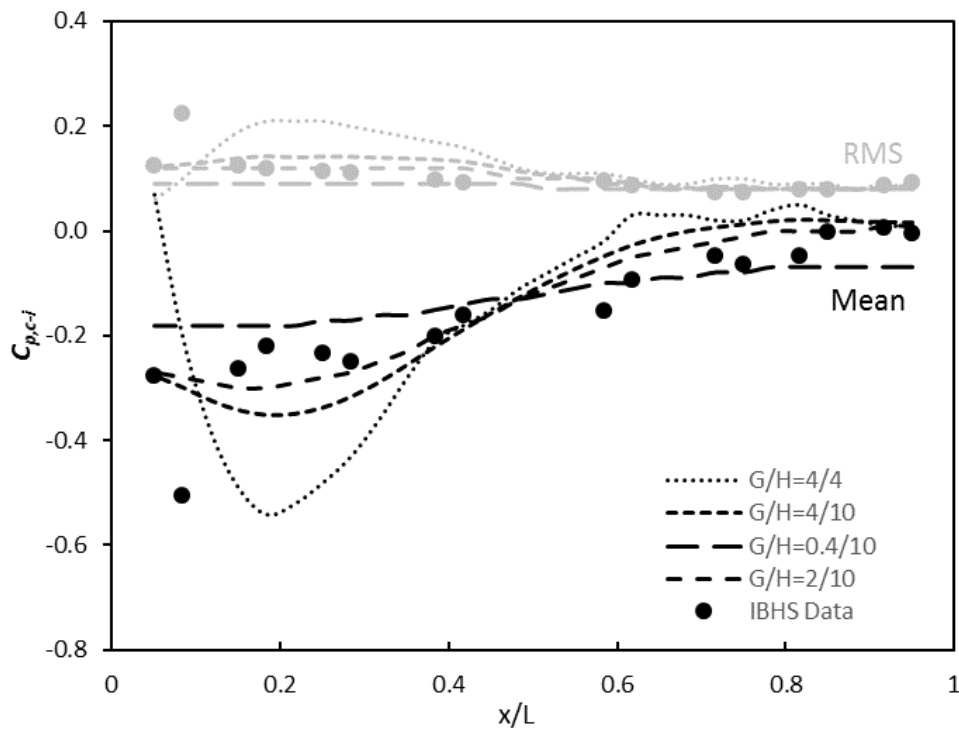

Figure 97: 20m/s, hip roof, FB sheathed predicted and measured coefficients
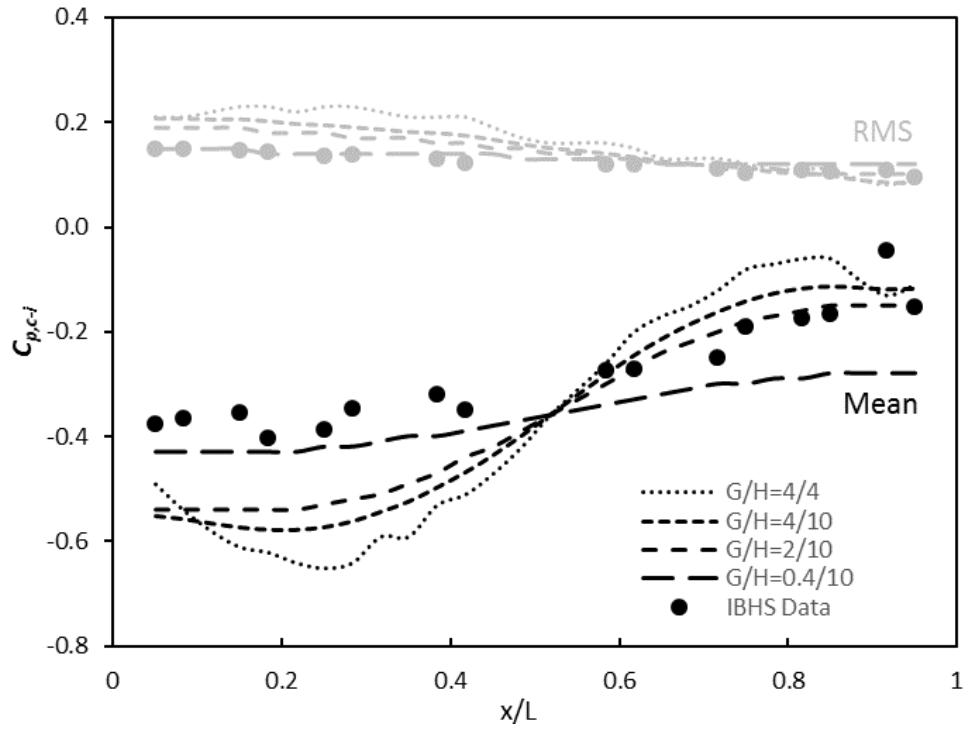
Figure 98: 20m/s, gable roof, FB sheathed predicted and measured coefficients
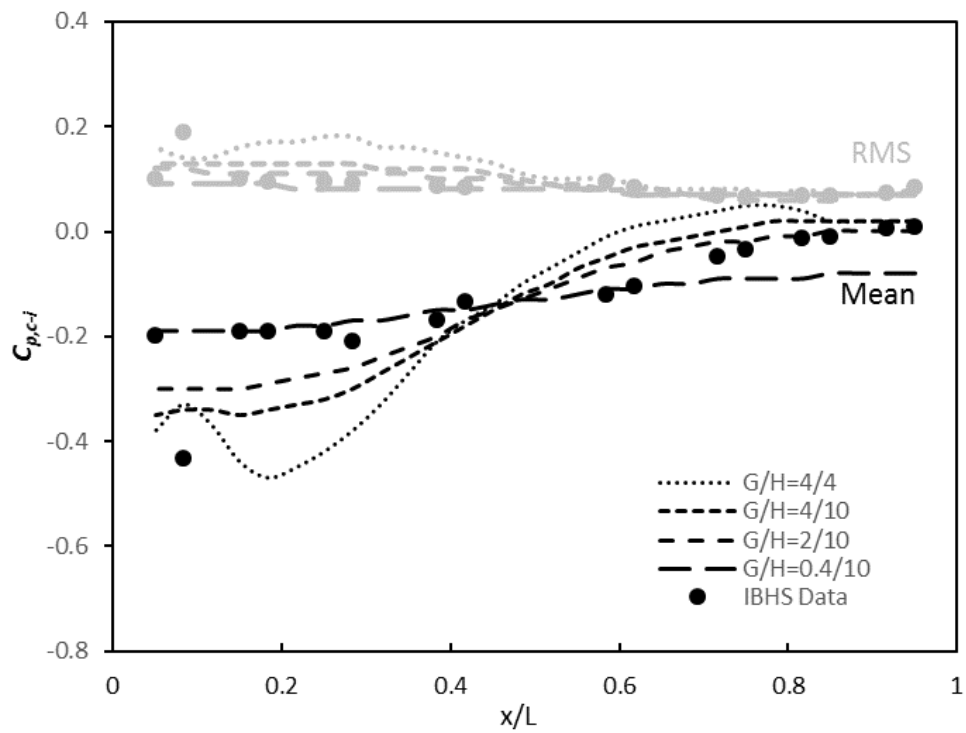
Figure 99: 27m/s, hip roof, FB sheathed predicted and measured coefficients
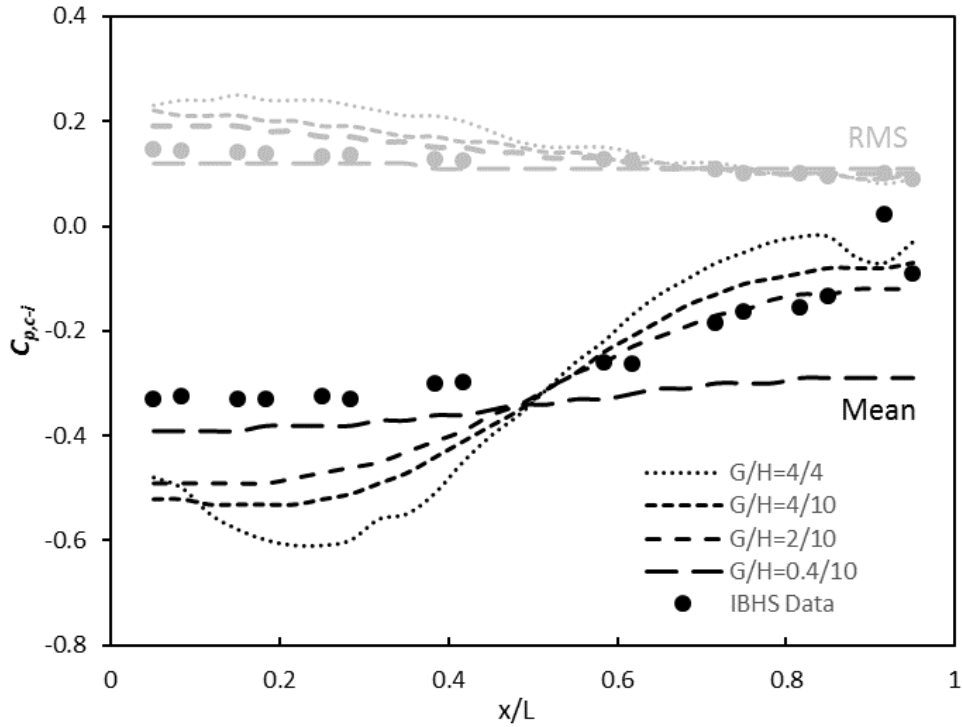
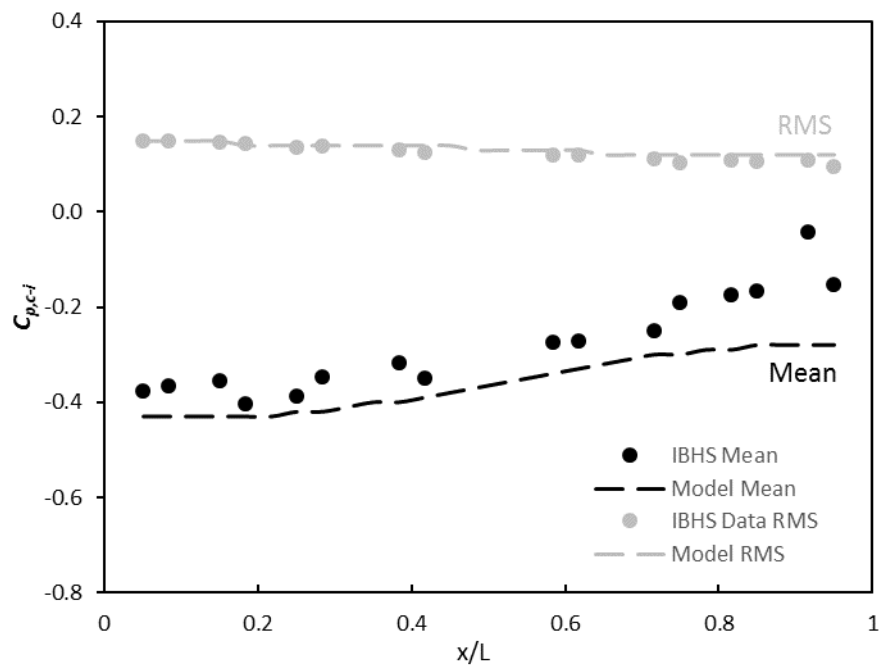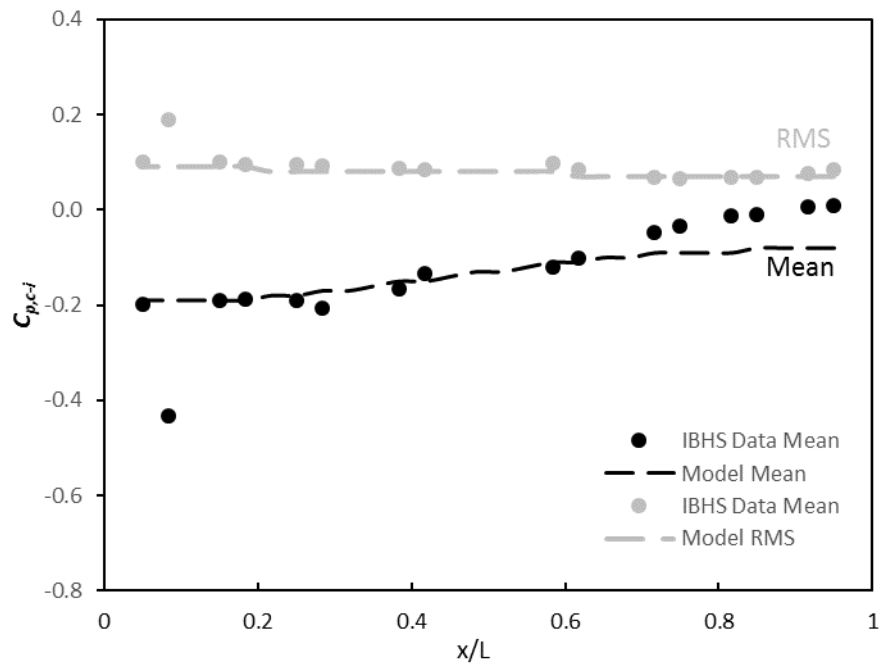Figure 100: 27m/s, gable roof, FB sheathed predicted and measured coefficients
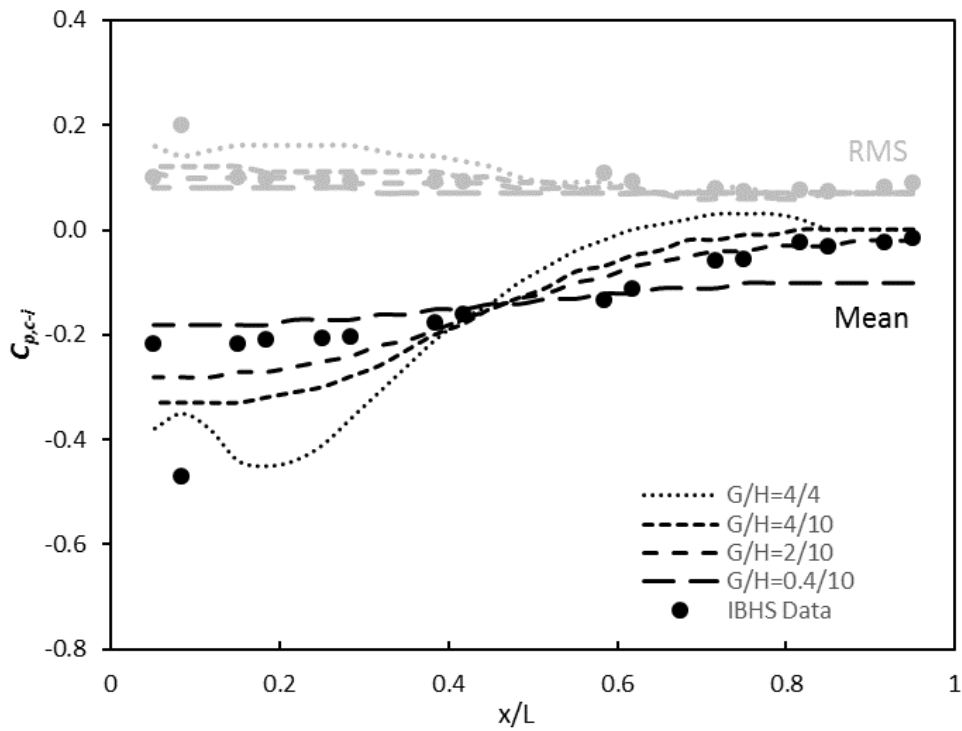
Figure 101: 35m/s, hip roof, FB sheathed predicted and measured coefficients
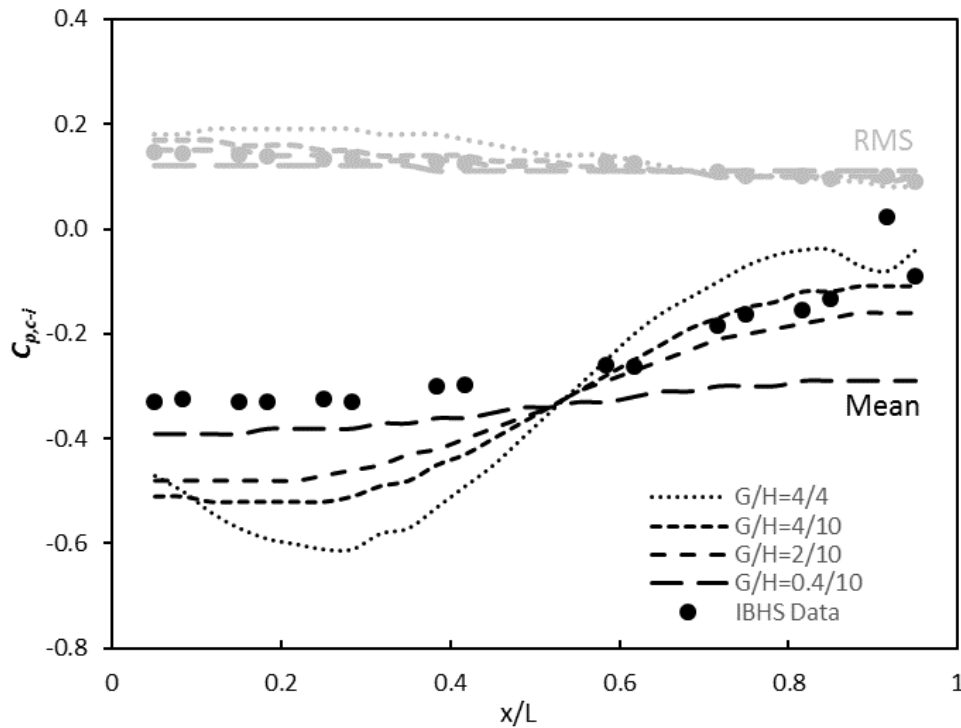
Figure 102: 35m/s, gable roof, FB sheathed predicted and measured coefficients

PEF values were calculated and plotted for the high 35 m/s wind speed condition in Figure 103 through Figure 106 for G/H=4/10 and 4/4 model scenarios and hip and gable roof exposures. The 90th percentile of the PEF values are shown as a dashed line in the plots. The results show that increasing the open area lowers the PEF to 0.5 to 0.6 for the G/H=4/10 model. Further decreasing the cavity depth lowers the PEF to 0.2 to 0.3 for the G/H=4/4 model meeting the performance of the ASTM D3679 load reduction factor. These effects are similar for both the hip and gable roof exposures.
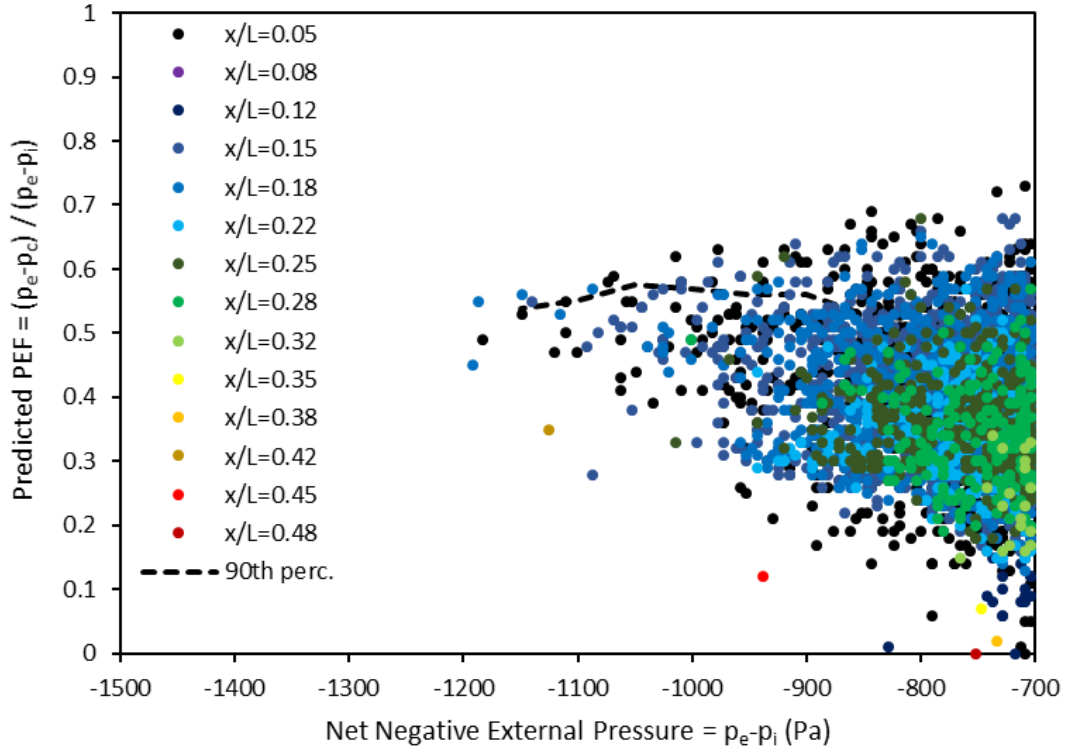
Figure 103: Predicted external pressure vs. PEF for hip roof, 35 m/s, G/H = 4/10
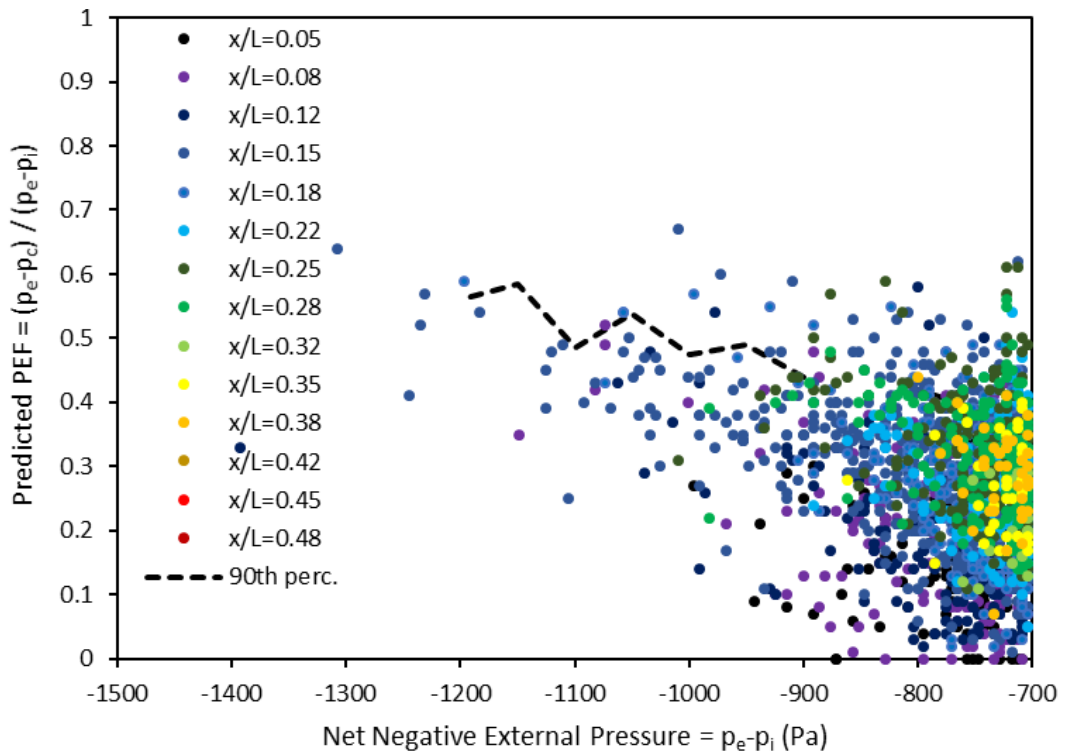
Figure 104: Predicted external pressure vs. PEF for gable roof, 35 m/s, G/H = 4/10
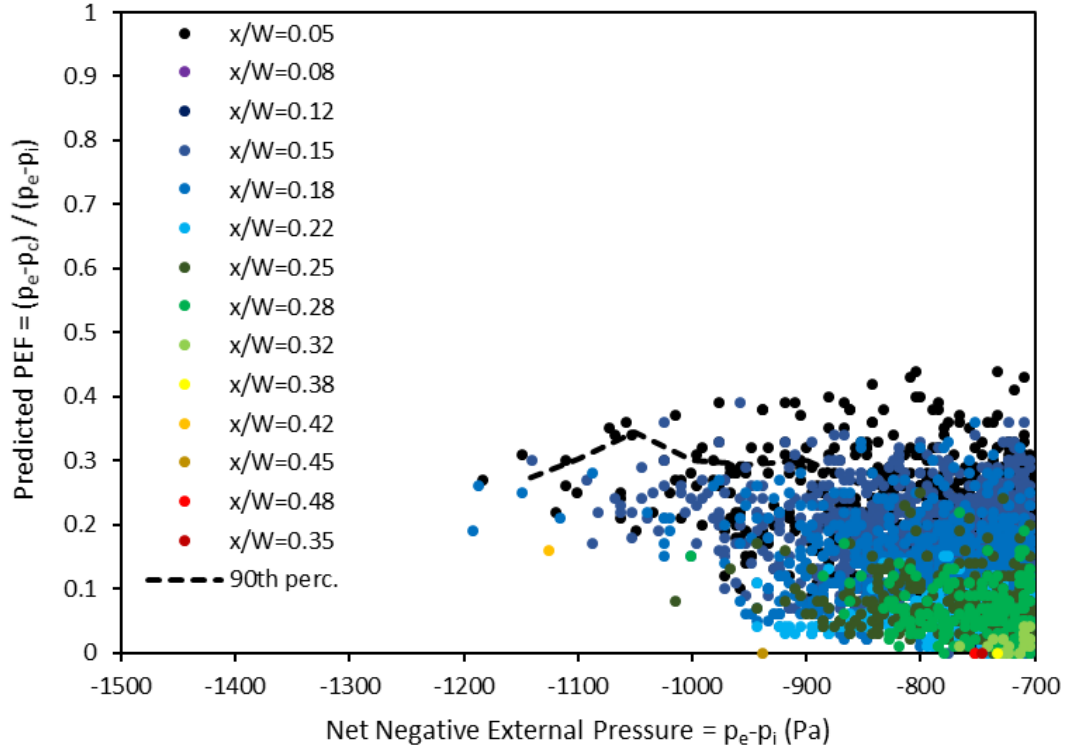
Figure 105: Predicted external pressure vs. PEF for hip roof, 35 m/s, G/H = 4/4
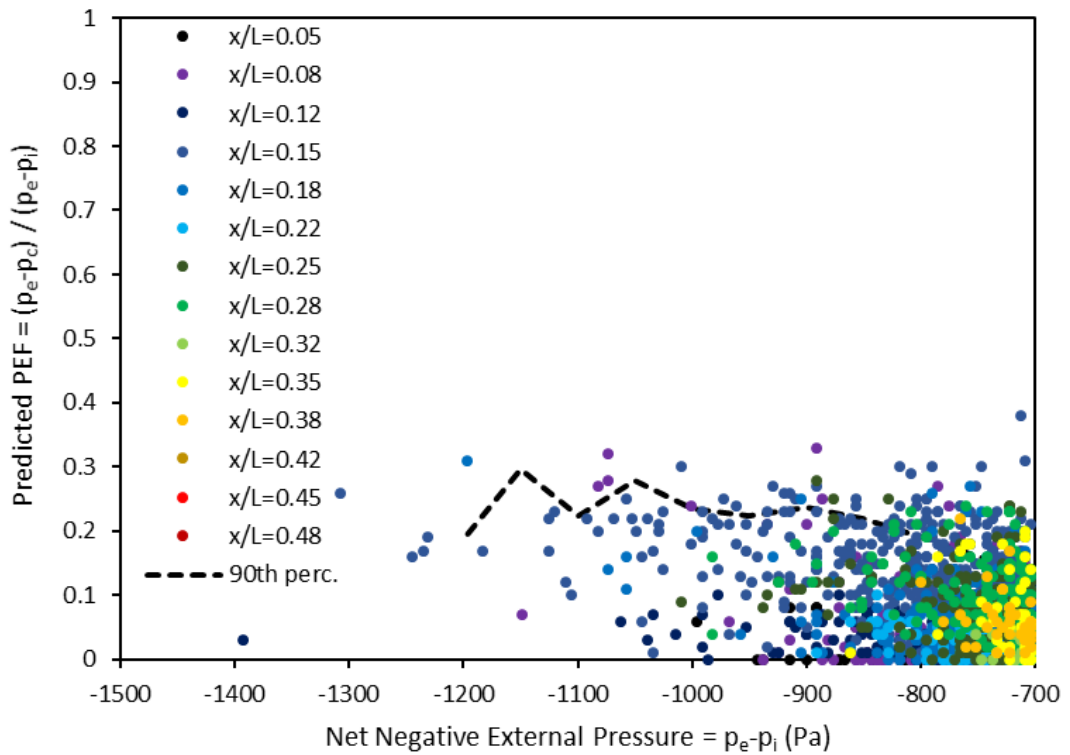
Figure 106: Predicted external pressure vs. PEF for gable roof, 35 m/s, G/H = 4/4

4.6 Closure

The cavity pressures for the tests did not appear to be affected by sheathing choice which would be have differences in flexibility. The sheathing would also have differences in air tightness. Air tightness measured of wall installed at the facility found a large variation. Furthermore, batt pressure measurements suggest significant differences in sheathing air tightness. However, the wall areas with high sheathing air leakage did show an effect on the cavity pressure.

The MDE model was found to accurately predict PEF values at peak loads for the vinyl siding tested at IBHS. This results further suggests that flexibility of wall layers and sheathing air leakage have little effect on pressure equalization for such vinyl siding clad systems.

Increasing the open area through the siding to 1.2% open leakage area and reducing the cavity depth to have a flow resistance equivalent to a 4mm cavity were needed to achieve the pressure equalization of vinyl siding in ASTM D3679. Practically such design modifications may not be achievable while maintaining other performance attributes (ventilation drying capacity, stiffness, pest control, aesthetics, UV solar control, etc.). Furthermore, in Chapter 3 it was found inaccuracies in the MDE model for the test setup with restriction cavity flow. Hence, the impacts of such modifications to vinyl siding should be verified by further testing.

Chapter 5

5 Conclusions and Recommendation

The objective of the study was to verify the accuracy of the MDE model for ventilated cladding pressure equalization application. Vinyl siding performance was of interest because, as explained in chapter 2, of the extent of failures in the field and high-pressure equalization allowance for such products in ASTM D3679.

Testing results and modelling presented in chapter 3 showed that the MDE model accurately predicted cavity pressures for a simplified cladding system which similar air flow resistance characteristics as vinyl siding. Furthermore, in chapter 4 an adapted MDE model for vinyl siding accurately predicted cavity pressure for vinyl siding clad walls tested in a full-scale wind tunnel. The findings provide verification of the model accuracy for vinyl siding applications.

Furthermore, simulations were conducted with physical modification to the vinyl siding. However, it remains uncertain if such modifications will encourage as much pressure equalization as predicted. The testing of variations to simplified cladding presented in chapter 3 suggest modifications of the MDE model may be necessary.

The following recommendations are for further full-scale testing of simplified cladding for model development.

- Investigation of cladding systems with shallow cavities will need more precise airflow rate measurements and control of experimental variables to accurately measure loss coefficients as parts of pressure equalization models.

- Air leakage inward through the sheathing could be evaluated by the additions of holes in the sheathing layer.

- The influence of layer flexibility and more realistic airflow paths (such as those through vinyl siding) could be incorporated by installing actual construction materials and allowing lateral movement between the airbox through the air cavities which exist behind such systems.

- The use of loose laid flexible membranes could be investigated by adding such products to these studies.

- Narrower airboxes could be used to investigative sensitivity to spatial variation in greater detail.

- Different and more complex orifice openings from the airbox through the cladding to the cavity could be evaluated.

Furthermore, additional features could be incorporated within the test rig to further understand the flow behavior providing greater confidence in the model and insights into the observed anomalies. Further flow visualization techniques are recommended in future studied to determine how these transitions occur and what structures develop under high frequency unsteady pressures.

- Smoke tests could be used to see the actual flow structure

- Cavity velocities could be measured using hot wire anemometry in such device could be designed in such a way as not to interrupt the cavity flow and not allow air leakage.

- Particle Image Velocimetry could be used to provide velocity mapping

In full-scale wind tunnel measurements of actual cladding systems and wall assemblies the following additions are recommended

- Install and provide full scale testing of vinyl siding with modified flow resistance characteristics to confirm the analytical model findings in this study

- Confirm that air leakage through sheathing does not affect cladding pressure equalization through a controlled experiment involving controlled air leakage through the sheathing

- Conduct measurements of cladding systems other than vinyl siding and wall systems (e.g. with variations of loose laid membranes)

References

American Society of Heating, Refrigerating and Air-Conditioning Engineers, Inc. (ASHRAE) **(2001)** *2001 ASHRAE handbook: Fundamentals, SI edition*, Atlanta, 2.11.

American Society of Civil Engineers, **(2010)** *ASCE 7-10*, "*Minimum Design Loads for Buildings and Other Structures*," Reston, VA, 2010.

Aly, A., and Bitsuamlak, G., **(2013)** "Wind-induced pressures on solar panels mounted on residential homes" *Journal of Architectural Engineering*, 20(1), 04013003.

Architectural Testing, Inc. (ATI), **(2002)** *"Wind Pressure Equalization Research Project Report." No. 01-40776.01 for the Vinyl Siding Institute*, Washington, DC.

AS/NZL 1170.2 **(2011)** *Australian/New Zealand standard: structural design actions, Part 2: wind actions*, Standards Australia/Standards New Zealand, Sydney, Australia.

ASTM **(2009)** *ASTM Standard D3679-09 Standard Specification for Rigid Poly (Vinyl Chloride) (PVC) Siding.* ASTM International, West Conshohocken, PA.

ASTM **(2006)** *ASTM Standard D5206-06a Wind Testing of Vinyl Siding.* ASTM International, West Conshohocken, PA.

Baskaran, A., **(2002)** "Dynamic wind uplift performance of thermoplastic roofing system with new seaming technology" *Journal of Architectural Engineering*, 8(4), pp. 1-11.

Bassett, M., and S. McNeil. **(2009)** *"Ventilation Measured in the Wall Cavities of High Moisture Risk Buildings" Journal of Building Physics*, 34(4), pp. 291-303.

Beavers, G., Sparrow, E., and Lloyd, J., **(1971)** "Low Reynolds number turbulent flow in large aspect ratio rectangular ducts" ASCE Journal of Basic Engineering, 93, pp. 296–299.

Bienkiewicz, B., and Sun, Y., **(1992)** "Wind-tunnel study of wind loading on loose-laid roofing systems" *Journal of Wind Engineering and Industrial Aerodynamics,* 41-44, pp. 1817-1828.

Bienkiewicz, B., and Sun, Y., **(1997)** *"Wind loading and resistance of loose-laid pavers systems" Journal of Wind Engineering and Industrial Aerodynamics,* 72, pp. 401-410.

Bofah, K. K., Gerhardt, H. J., and Kramer, C. **(1996)** "Calculations of pressure equilibration underneath loose-laid, flow permeable roof insulation boards" *Journal of Wind Engineering and Industrial Aerodynamics*, 59(1), pp. 23-37.

Cheung, W., **(1986)** "Wind loading on porous cladding" *Proceedings of the 9th Australasian Fluid Mechanics Conference*, Auckland.

Choi ECC and Wang Z. **(1998)** "Study on pressure-equalization of curtain wall systems", *Journal of Wind Engineering and Industrial Aerodynamics*, 73 pp. 251-266

Cope, A. D., Crandell, J. H., Johnston, D., Kochkin, V., Liu, Z., Stevig, L., and Reinhold, T., **(2012)** "Wind loads on components of multi-layer wall systems with air-permeable exterior cladding," *Proceedings of the ATC-SEI Advances in Hurricane Engineering Conference*, Miami, FL.

Cope, A.D., Crandell, J.K., Liu, Z., and Stevig, L.J., **(2014)** "Wind loads on fasteners used to attach flexible porous siding on multi-layer wall systems", *Journal of Wind Engineering and Industrial Aerodynamics,* 133, pp.150-159.

Currie, I. G. **(1974)** *Fundamental mechanics of fluids*, CRC Press.

Davidovic, D., Pinon, J., Burnett, E.F.P., and Srebric, J., **(2012)** "Analytical procedures for estimating airflow rates in ventilated, screened wall systems (VSWS)", *Building and Environment*, 47, pp. 126-137.

Earles, S. W. E., and Zarek, J. M. **(1963)** "Use of sharp-edged orifices for metering pulsating flow", *Proceedings of the Institution of Mechanical Engineers*, 177(1), pp. 997-1024.

Etheridge, D. W. **(2000)** "Unsteady flow effects due to fluctuating wind pressures in natural ventilation design—mean flow rates", *Building and Environment*, 35(2), pp. 111-133.

Federal Emergency Management Agency (FEMA) **(2010)** *P-499 Homebuyers Guide to Coastal Construction Technical Fact Sheet No. 5.3 Siding Installation in High Wind Regions*.

Garden, G.K., **(1963)** "Rain Penetration and its Control", *Canadian Building Digest – 40*, NRC-IRC Publications, Ottawa.

Gavanski, E., and Kopp, G. A., **(2012)** "Effects of pressure equalization on the performance of residential wall systems under extreme wind loads", *Journal of Structural Engineering* 138, pp. 526–538.

Gerhardt, H.J., and Janser, F., **(1994)** "Wind loads on wind permeable facades", *Journal of Wind Engineering and Industrial Aerodynamics* 53, pp. 37-48.

Gudum, C. **(2003)** "Moisture transport and convection in building envelopes – ventilation in light weight outer walls", *PhD Thesis,* University of Denmark.

Holmes, J.D., **(1994)** "Wind pressures on tropical housing", *Journal of Wind Engineering and Industrial Aerodynamics*, 53, pp 105-123.

Holmes, J.D., **(2001)** *Wind loading of structures 2nd Ed.,* Taylor & Francis, New York.

Idelchik, I.E., and Fried, E., **(1986)** *Handbook of Hydraulic Resistance 2nd Ed.,* Hemisphere Pub. Corp, Washington.

Ilić, D., Butorac, J., and Ferković, L. **(2008)** *"*Temperature measurements by means of NTC resistors and a two-parameter approximation curve"*, Measurement*, 41(3), 294-299.

IBC **(2012)** *International Building Code*, International Code Council, Inc., www.iccsafe.org

IRC **(2012)** *International Residential Code*, International Code Council, Inc. www.iccsafe.org

Kim, P.Y., and Ginger, J.D., **(2012)** "Discharge coefficient for a dominant opening in a building", *15th Australasian Wind Engineering Society Workshop*, Sydney, Australia.

Kopp, G., Morrison, M., Gavanski, E., Henderson, D., and Hong, H., **(2010)** ""Three Little Pigs" Project: Hurricane Risk Mitigation by Integrated Wind tunnel and Full-Scale Laboratory Tests", *ASCE Natural Hazard Review*, November, pp. 151-161.

Kumar K.S., **(2000)** "Pressure equalization of rainscreen walls: a critical review", *Building and Environment* 35, pp. 161-179.

Miller, C., Kopp, G., Morrison, M., Kemp, G., and Drought, N., **(2017)** "Multichamber, Pressure-Based Test Method to Determine Wind loads on air-Permeable, Multilayer cladding systems" *Frontiers in Built Environment*, 3:7, pp. 1-12.

Minkowycz, W., Abraham, J., and Sparrow, E., **(2009)** "Numerical simulation of laminar breakdown and subsequent intermittent and turbulent flow in parallel-plate channels: Effects of inlet velocity profile and turbulence intensity" *International Journal of Heat and Mass Transfer*, 52, pp. 4040-4046.

Mooneghi, M., Irwin, P., and Chowdhury, A., **(2014)** "Large-scale testing on wind uplift of roof pavers" *Journal of Wind Engineering and Industrial Aerodynamics*, 128, pp 22-36.

Moravej, M., Ioannis Zisis, I., Chowdhury, A., Irwin, P., and Hajra, B., (**2016**) "Experimental assessment of Wind loads on Vinyl Wall siding" *Frontiers in Built Environment*, 2:35, pp. 1-9.

Morrison, M., Brown, T., and Liu, Z., **(2012)** "Comparison of field and full-scale laboratory pressures at the IBHS research center" *Proceedings of the ATC-SEI Advances in Hurricane Engineering Conference*, Miami, FL.

Morrison, M., and Cope, A. **(2015)** "Wind performance and evaluation methods of multi-layered wall assemblies" *Structures Congress 2015*, pp. 2735-2748.

Munson, B., Young, D., and Okiishi, T., **(1998)** *Fundamentals of Fluid Mechanics 3rd Ed.* John Wiley & Sons, Toronto.

National Association of Home Builders Research Center (NAHBRC) **(2012)** *Evaluation of the Wind Pressure Performance of Walls with Exterior Rigid Foam Sheathing*, Upper Marlboro, MD: NAHB Research Center, Inc.

National Institute for Standard and Technology (NIST), **(2006)** *Technical Note 1476: Performance of Physical Structures in Hurricane Katrina and Hurricane Rita: A Reconnaissance Report,* Gaithersburg, MD, pp 168-171.

Oh, J.H., **(2014)** "Wind-induced pressures in air permeable, double-layer roof systems in regions of separated flow", *Ph.D. Thesis,* University of Western Ontario.

Oh, J. H., and Kopp, G. A., **(2014)** "Modelling of spatially and temporally-varying cavity pressures in air permeable, double-layer roof systems", *Building and Environment* 82, pp. 135–150.

Oh, J. H., and Kopp, G. A., **(2015)** "An experimental study of pressure distributions within an air-permeable, double-layer roof system in regions of separated flow", *Journal of Wind Engineering and Industrial Aerodynamics* 138, pp. 1-12.

Oh, J.H., Kopp, G.A., and Inculet, D.R., **(2007)** *"*The UWO contribution to the NIST aerodynamic database for wind loads on low buildings: Part 3. Internal Pressures*", Journal of Wind Engineering and Industrial Aerodynamics* 95, pp. 755-779.

Ormieres, D., and Provansal, M., **(1999)** "Transition to turbulence in the wake of a sphere", *Physics Review Letters* 83 (1): 80–83.

Richardson, E. G., and Tyler, E. **(1929)** "The transverse velocity gradient near the mouths of pipes in which an alternating or continuous flow of air is established", *Proceedings of the Physical Society*, 42(1), 1.

Straube, J. **(1998)** "Moisture control and enclosure wall systems" *Ph.D. Thesis*, University of Waterloo.

Straube, J.F., and Burnett, E.F.P., **(1995)** *Vents, Ventilation, and Pressure Moderation.* University of Waterloo Building Engineering Group Report for Canada Mortgage and Housing Corp, Ottawa.

Straube, J.F., and Burnett, E.F.P., **(1999)** "Rain Control and Design Strategies", *Journal of Building Physics* 23(1), pp. 41-56.

Sun, Y., and Bienkiewicz, B., **(1993)** "Numerical Simulation of Pressure distributions Underneath Roofing Paver Systems", *Journal of Wind Engineering and Industrial Aerodynamics* 46-47, pp. 517-626.

Surry, D., **(1991)** *"Pressure Measurements on the Texas Tech building –II: Wind tunnel measurements and comparisons with full scales", Journal of Wind Engineering and Industrial Aerodynamics* 38, pp. 235-247.

Swami, M. and Chandra, S., **(1987)** "Procedures for calculating natural ventilation airflow rates in buildings" *Final Report FSEC-CR-163-86*. Florida Solar Energy Center, Cape Canaveral.

Uvsløkk, S., **(1996)** "The importance of wind barriers for insulated timber frame constructions", *Journal of Building Physics* 20(1): 40-62.

Van Bentum, C., and Geurts, C., **(2015)** "Full scale measurements of pressure equalization on air permeable façade elements", *14th International Conference on Wind Engineering*, Porto Alegre, Brazil.

Van Bentum, C., Kalkman, I., and Geurts, C. **(2012)** "Towards a better understanding of pressure equalization", *The Seventh International Colloquium on Bluff Body Aerodynamics and Applications*, Shanghai, China.

Van Straaten, R., **(2004)** "Ventilation of Cladding Systems." *M.A.Sc. Thesis*, University of Waterloo.

Vickery, B., **(1986)** "Guest factors for internal pressures in low-rise buildings", *Journal of Wind Engineering and Industrial Aerodynamics* 23(1), pp. 259-271.

Yakhot, A., Arad, M., and Ben-Dor, G., **(1999)** "Numerical investigation of a laminar pulsating flow in a rectangular duct", *International Journal for Numerical Methods in Fluids* 19, pp. 935-950.

Warsido, W., Bitsuamlak, G., Barata, J., and Chowdhury, A. **(2014)** "Influence of spacing parameters on the wind loading of solar array", *Journal of Fluids and Structures* 48, pp. 295–315.

White, F., **(2011)** *Fluid Mechanics 7th Edition*, McGraw-Hill, New York.

Wiggert, M. C., and Potter, D. C. **(2002)** *Mechanics of Fluids*, Brooks Cole /Thompson Learning.

Appendix

Appendix A: Uncertainty Analysis

Kline and McClintock Uncertainty Calculation Method
taken from Holman, J.P., (2012) *Experimental Methods of Engineers 8th Ed.* McGraw Hill New York

uncertainty $f(x_1,x_2)=\omega f(x_1,x_2)$

$\omega f(x_1,x_2)=[(df(x_1,x_2)/dx_1\cdot\omega x_1)^2+(df(x_1,x_2)/dx_2\cdot\omega x_2)^2]^{1/2}$

where

x_1 and x_2 are independent variables

repeated measurements of x_1 and x_2 display Gaussian distribution (error is random)

uncertainties of x_1 and x_2 are expressed with same odds

note: the odds associated with the uncertainties of the independent variables are not known in this case and hence, the method is being used as an uncertainty approximation within this study.

	A	B	C	D	Unit
slot length, l	6.45	6.45	6.45	6.45	mm
uncertainty (range of measurements at 15 locations)	0.05	0.05	0.05	0.05	mm
slot width, G	2.44	2.44	2.44	2.44	mm
uncertainty (range of mean per slot measurements)	0.03	0.03	0.03	0.03	mm
slot and cavity height, W	150	150	150	150	mm
uncertainty (1/16" measurement tape check)	1.6	1.6	1.6	1.6	mm
cavity depth, H	2.58	2.58	9.42	9.42	mm
spacer sheet thickness (measured in 16 places)	0.02	0.02	0.08	0.08	mm
deflection (measured under 2 kPa airbox pressure)	0.06	0.06	0.06	0.06	mm
uncertainty	0.06	0.06	0.10	0.10	mm
cavity length, L	604	604	604	604	mm
uncertainty (1/16" measurement tape check)	1.6	1.6	1.6	1.6	mm
temperature, T	20	20	20	20	C
uncertainty (10kOhm Fenwall linearity error - Ilic 2008)	0.2	0.2	0.2	0.2	C
atmospheric pressure, P_{atm}	101.3	101.3	101.3	101.3	kPa
uncertainty (nearby weather station - estimated)	0.5	0.5	0.5	0.5	kPa
density, ρ					
Ideal Gas Law with gas constant for air from ASHRAE 2001					
$\rho = P_{atm}/(287\cdot(T+273.15))$	1.20	1.20	1.20	1.20	kg/m^3
uncertainty (based on T and P_{atm} uncertainty)	0.003	0.003	0.003	0.003	kg/m^3
dynamic viscosity, μ					
Sutherland formula from Munson et. al. 2001					
$\mu = 1.827\text{E}-5\cdot[411.15/(T+393.15)]\cdot[(T+273.15)/291.15]^{1.5}$	1.8E-05	1.8E-05	1.8E-05	1.8E-05	Pa s
uncertainty (based on T uncertainty)	9.9E-09	9.9E-09	9.9E-09	9.9E-09	Pa s

	A	B	C	D	Unit
airbox pressure (from test), p	300	2000	300	2000	Pa
cavity pressure (from test), $p_{x/L=0}$	250	1000	100	200	Pa
cavity pressure (from test), $p_{x/L=1/4}$	170	900	99	190	Pa
cavity pressure (from test), $p_{x/L=3/4}$	130	250	97	170	Pa
cavity pressure (from test), $p_{x/L=1/4}$	110	200	90	160	Pa
cavity pressure (from test), $p_{x/L=3/4}$	100	40	89.5	155	Pa
uncertainty (calibration with u-tube manometer)	16	16	16	16	Pa
flowrate, Q	2	10	5	13	lps
accuracy of LFE based on reading	0.76%	0.76%	0.76%	0.76%	
inclined manometer uncertainty (0.005" W.C. precision)	0.9	0.9	0.9	0.9	lps
air leakage uncertainty (measured with Dwyer rotameter)	0.1	0.1	0.1	0.1	lps
total flowrate uncertainty	0.9	0.9	0.9	0.9	lps
Reynold Number, Re					
$Re = 2\rho Q/(\mu W)$	1748	8739	4370	11361	-
uncertainty (based on ρ, Q, μ, and W uncertainty)	774	782	776	788	-
cavity friction factor					
$f = \left(P_{c,x/L=1/4} - P_{c,x/L=3/4}\right)/[0.5\rho(Q/WH)^2] \cdot 2H/0.5L$	0.043	0.028	0.017	0.024	-
uncertainty (based on P, P, ρ, Q, W, H, and L uncertainty)	0.044	0.005	0.182	0.027	-
orifice loss coefficient, Cl					
$C_l = (P_e - P_c)/[0.5\rho(Q/WG)^2]$	2.78	2.23	1.78	2.37	-
uncertainty (based on P, P, ρ, Q, W, and G uncertainty)	2.75	0.40	0.66	0.33	-
Flowrate Ratio at Intermediate Slots					
$Q_t/Q = \left(P_{c,x/L=1\,1/4} - P_{c,x/L=1\,3/4}\right)/\left(P_{c,x/L=1/4} - P_{c,x/L=3/4}\right)$	0.25	0.25	0.25	0.25	-
$Q_b/Q = 1 - Q_t/Q$	0.75	0.75	0.75	0.75	-
uncertainty (based on pressures)	0.40	0.02	8.03	0.80	-
Flowrate thru Intermediate Slots					
$Q_t = Q \cdot \left(P_{c,x/L=1\,1/4} - P_{c,x/L=1\,3/4}\right)/\left(P_{c,x/L=1/4} - P_{c,x/L=3/4}\right)$	0.50	2.46	1.25	3.25	lps
uncertainty (based on flowrate and pressures)	0.92	2.20	40.15	10.83	lps
Flowrate Branching at Intermediate Slots					
$Q_b = Q - Q_t$	1.50	7.54	3.75	9.75	lps
uncertainty (based on flowrate and pressures)	1.27	2.37	40.16	10.86	lps

Curriculum Vitae

Name: Randy Van Straaten

**Post-secondary   Waterloo University
Education and   Waterloo, Ontario, Canada
Degrees:**   1995-2000 B.A.Sc. (Mechanical)

                     Waterloo University
                     Waterloo, Ontario, Canada
                     2001-2004 M.A.Sc. (Civil)

                     The University of Western Ontario
                     London, Ontario, Canada
                     2010-2016 Ph.D.

**Honours and   NSERC Industrial Partnership Scholarship
Awards:**   2010-2013

**Related Work   Teaching Assistant
Experience**   Waterloo University
                     2001-2003

                     Senior Research Engineer
                     RDH Building Science Inc.
                     2008-2017